PIEZOELECTRIC ENERGY HARVESTING FOR MUNITIONS APPLICATIONS

A THESIS SUBMITTED TO
THE GRADUATE SCHOOL OF NATURAL AND APPLIED SCIENCES
OF
MIDDLE EAST TECHNICAL UNIVERSITY

BY

KURTULUŞ ERSOY

IN PARTIAL FULFILLMENT OF THE REQUIREMENTS
FOR
THE DEGREE OF MASTER OF SCIENCE
IN
MECHANICAL ENGINEERING

SEPTEMBER 2011

Approval of the thesis:

PIEZOELECTRIC ENERGY HARVESTING FOR MUNITIONS APPLICATIONS

submitted by **KURTULUŞ ERSOY** in partial fulfillment of requirements for the degree of **Master of Science in Mechanical Engineering Department**, **Middle East Technical University** by,

Prof. Dr. Canan ÖZGEN   _____
Dean, Graduate School of **Natural and Applied Sciences**

Prof. Dr. Suha ORAL   _____
Head of Department, **Mechanical Engineering**

Prof. Dr. Mehmet ÇALIŞKAN   _____
Supervisor, **Mechanical Engineering Dept., METU**

Examining Committee Members

Prof. Dr. Tuna BALKAN   _____
Mechanical Engineering Dept., METU

Prof. Dr. Mehmet ÇALIŞKAN   _____
Mechanical Engineering Dept., METU

Assist. Prof. Dr. Yiğit YAZICIOĞLU   _____
Mechanical Engineering Dept., METU

Assist. Prof. Dr. Ender CİĞEROĞLU   _____
Mechanical Engineering Dept., METU

Taner KARAGÖZ, M.Sc.   _____
Defence Systems Technologies Division, ASELSAN

Date: 12/09/2011

I hereby declare that all information in this document has been obtained and presented in accordance with academic rules and ethical conduct. I also declare that, as required by these rules and conduct, I have fully cited and referenced all material and results that are not original to this work.

Name, Last name: Kurtuluş ERSOY

Signature   :

ABSTRACT

PIEZOELECTRIC ENERGY HARVESTING FOR MUNITIONS APPLICATIONS

ERSOY, Kurtuluş

M.Sc., Department of Mechanical Engineering

Supervisor: Prof. Dr. Mehmet ÇALIŞKAN

September 2011, 163 pages

In recent years, vibration-based energy harvesting technologies have gained great importance because of reduced power requirement of small electronic components. External power source and maintenance requirement can be minimized by employment of mechanical vibration energy harvesters. Power sources that harvest energy from the environment have the main advantages of high safety, long shell life and low cost compared to chemical batteries. Electromagnetic, electrostatic and piezoelectric transduction mechanisms are the three main energy harvesting methods.

In this thesis, it is aimed to apply the piezoelectric elements technology to develop means for energy storage in munitions launch. The practical problems encountered in the design of piezoelectric energy harvesters are investigated. The applicability of energy harvesting to high power needs are studied. The experience compiled in the

study is to be exploited in designing piezoelectric energy harvesters for munitions applications.

Piezoelectric energy harvesters for harmonic and mechanical shock loading conditions with different types of piezoelectric materials are designed and tested. The test results are compared with both responses from analytical models generated in MATLAB® and ORCAD PSPICE®, and finite element method models generated in ATILA®. Optimum energy storage methods are considered.

Keywords: Piezoelectric Materials, Energy Harvesting, Finite Element Modelling of Piezoelectric Materials, Continuous Modelling of Piezoelectric Materials

ÖZ

MÜHİMMAT UYGULAMALARI İÇİN PİEZOELEKTRİK ENERJİ HASADI

ERSOY, Kurtuluş

Yüksek Lisans, Makina Mühendisliği Bölümü

Tez Yöneticisi: Prof. Dr. Mehmet Çalışkan

Eylül 2011, 163 Sayfa

Son yıllarda, küçük elektronik parçaların düşen güç gereksinimleri nedeniyle titreşim kaynaklı enerji hasadı büyük önem kazanmıştır. Harici güç kaynağı ve bakım gereklilikleri mekanik titreşim güç üreteçleri kullanımı sayesinde en düşük seviyeye indirilebilmektedir. Çevresel koşullardan güç üretimi kimyasal bataryalara göre yüksek güvenilirlik, uzun raf ömrü ve düşük fiyat avantaja sahip olma temel avantajlarına sahiptir. Elektromanyetik, elektrostatik ve piezoelektrik enerji çevirim mekanizmaları üç temel enerji hasadı yöntemidir.

Bu çalışmada, piezoelektrik eleman teknolojilerinin mühimmat patlaması sonucu enerji depolama yöntemi olarak uygulanması amaçlanmıştır. Piezoelektrik enerji üreteçlerinin tasarımlarında karşılaşılan sorunlar araştırılmıştır. Enerji hasadının yüksek güç ihtiyaçlarına göre uygulanabilirliği üzerine çalışılmıştır. Çalışmada elde

edilen deneyim mühimmat uygulamaları için piezoelektrik güç üreteci tasarımında kullanılacaktır.

Harmonik ve mekanik şok yükleme durumları için farklı tipten piezoelektrik malzemeler içeren piezoelektrik güç üreteçleri tasarlanmış ve test edilmiştir. Test sonuçları MATLAB® ve ORCAD PSPICE® programlarında hazırlanan analitik modeller ve ATILA® programında hazırlanan sonlu elemanlar modelleri ile karşılaştırılmıştır. Kazanılan enerjinin optimum olarak saklanması konusu da incelenmiştir.

Anahtar Kelimeler: Piezoelektrik Malzemeler, Piezoelektrik Malzemelerin Sonlu Elemanlar Yöntemi ile Modellenmesi, Piezoelektrik Malzemelerin Devamlı Olarak Modellenmesi

Dedicated with Love to My Family, Bilge FİLİZ and my lovebird Kemal

ACKNOWLEDGMENTS

TABLE OF CONTENTS

APPENDICES

NOMENCLATURE

A	Cross-sectional area of the piezoelectric material
$a(t)$	Acceleration of the environment
C	Capacitance of Piezoelectric Material
c	Elastic constant
c_r	Damping of the resonator
c_f	Fluid sound speed
$\left[c^E\right]$	Matrix of elastic coefficients at constant electrical field
D	Constant electrical displacement where the open circuit conditions exist
d	Piezoelectric constant
$\{D\}$	Electrical displacement vector
E	Constant electrical field where the short circuit conditions applied
E_{elec}	Electrical energy
E_{mech}	Mechanical energy
$\{E\}$	Electrical field vector
e	Piezoelectric stress constant
$[e]$	Piezoelectric stress matrix
$\underline{F}$	Vector of the nodal values of the applied forces
$F(t)$	Forcing function of the resonator
$F_{pz}(t)$	Piezoelectric compression forcing function
$\underline{f}$	Vector of the nodal values of the reduced magnetic field flux across the magnetic domain boundary

f_a	Anti-resonance frequency
$\underline{f_b}$	Vector of the nodal values of the the reduced magnetic field flux seen by the coils
f_r	Resonance frequency
g	Piezoelectric voltage constant
$[H]$	Fluid (pseudo-) stiffness matrix
$H_{pz}(w)$	Frequency response function of piezoelectric material
h_{pz}	Height of the Piezoelectric Material
$\underline{I}$	Vector of the prescribed values of the excitation currents
$[K_{uu}]$	Stiffness matrix
$[K_{u\Phi}]$	Piezoelectric matrix
$[K_{u\phi}]$	Piezomagnetic coupling matrix
$[K_{uI}]$	Source-structure coupling matrix
$[K_{\Phi\Phi}]$	Dielectric Matrix
$[K_{\phi I}]$	Source-magnetization coupling matrix
$[K_{\phi\phi}]$	Magnetic (pseudo-) stiffness matrix
$[K_{II}]$	Inductance matrix in vacuum
k	Electromechanical coupling coefficient
k_r	Stiffness of the resonator
L	Inductance
$[L]$	Coupling matrix at the fluid structure interface
$[M]$	Consistent Mass matrix
$[M_1]$	Consistent (pseudo-) fluid mass matrix

m	Compression mass
$m(x)$	Mass per length of the piezoelectric material
P	Power
$\underline{P}$	Vector of the nodal values of the pressure field
Q	Charge created by piezoelectric material
Q_m	Mechanical quality factor
$\underline{q}$	Vector of nodal values of the electrical charges
R	Resistance
S	Constant strain where the material is mechanically constrained
$\{S\}$	Strain vector
s	Elastic compliance
T	Constant stress condition where the material is unconstrained mechanically
T_c	Curie temperature
$\{T\}$	Stress vector
t_{pz}	Thickness of the piezoelectric material
$\tan\delta$	Loss tangent
$\underline{U}$	Vector of nodal values of the components of the displacement field
$u(x,t)$	Displacement response of piezoelectric material in continuous modelling
$V_{\max}$	Maximum voltage production capability of piezoelectric material
V_{pf}	Poling field voltage
$x(t)$	Displacement response of the resonator

Y	Young's modulus
$[\alpha^s]$	Dielectric matrix at constant mechanical strain
ε	Permittivity of a material
ζ	Damping ratio of the resonator
δ	Dirac Delta Function
ρ_s	Surface mass density
ρ_f	Fluid density
$\underline{\Phi}$	Vector of the nodal values of the electric potential
$\underline{\phi}$	Vector of the nodal values of reduced magnetic potential
$\underline{\Psi}$	Vector of the nodal values of the integrated normal derivative of the pressure on the surface boundary
v	Viscosity
w	Frequency
w_d	Damped natural frequency of the resonator
w_n	Natural frequency of the resonator

Subscripts

i	Direction of electric field
j	Direction of the mechanical strain or the stress
stk	Piezoelectric Stack
pz	Piezoelectric
m	Mechanical

Abbreviations

FEM   Finite Element Modelling

FFT   Fast Fourier Transformation

PZT $Pb(Zr,Ti)O_3$

PT $PbTiO_3$

PLZT $(Pb,La)(Zr,Ti)O3$

PPG   Pressure Pulse Generator

rms   Root mean square

LIST OF TABLES

TABLES

LIST OF FIGURES

CHAPTER 1

INTRODUCTION

Electromagnetic, electrostatic and piezoelectric transduction mechanisms are three main energy harvesting methods. Basically, electromagnetic generators utilize electromagnetic induction arising from the relative motion between a magnetic flux gradient and a conductor. Electrostatic generators utilize relative movement between electrically isolated charged capacitor plates to generate energy. Piezoelectric materials employ active materials that generate a charge when mechanically stressed [1]. Energy harvesting by piezoelectric materials has received greatest attention in recent years because of their large power densities and ease of application [2].

In this chapter, detailed information about piezoelectricity history, piezoelectric material types, physical phenomenon of piezoelectric materials, typical applications of piezoelectric materials are mentioned. Motivation for the study is discussed at the end of the chapter.

1.1 Piezoelectricity History

In Greek, "piezin" means "to press" and the term piezoelectric is thought to be defined the direct piezoelectric effect of this kind of materials [3].

It was first noticed in rocks which repel other rocks when they were heated [4]. In the mid-18th century, the pyroelectric effect (from the Greek pyr, fire, and electricity),

which is the ability of generating electric potential when a temperature change occurs, was studied by Carolus Linnaeus and Franz Aepinus. Further examination of these materials by forming a relationship between mechanical stress and charge is resulted in the invention of piezoelectricity [5]. In 1880, the first demonstration of the direct piezoelectric effect which relates mechanical strain to electric potential was done by the Pierre Curie and Jacques Curie [6]. However, Curie Brothers did not predict the converse piezoelectric effect which relates applied electrical voltage to mechanical strain. In 1881, this effect was deduced by Gabriel Lippmann [5].

The first serious application of piezoelectric materials is in the World War I. Langevin and co-workers developed a transducer to measure submarine depth [3]. Between 1920 and 1940, by single crystals, quartz resonators, non-destructive testing methods of fluids and solids and transient measure of pressure were achieved. In the World War II, the studies were focused on increasing the sensitivity and output power of piezoceramics by U.S., Japan and Soviet Union. Powerful sonar systems, small microphones, ignition systems etc. are developed by exploiting piezoelectric materials. Most of the materials used in piezoelectric phenomena applications have been created artificially by 1970 [7].

In recent years, the most popular application area of piezoelectric materials is in sensors where their linear response is very useful in mechanical measurements like acceleration and pressure. The usage of piezoelectric materials as actuators by converse piezoelectric effect is a growing field [4]. In the last decade, their usage in energy harvesting applications is becoming more popular because of reduced power requirement of small electronic components [2].

1.2   Piezoelectric Material Types

Two main types of piezoelectric materials namely crystalline materials and ceramic materials exist. Crystalline materials which are naturally occurring crystals are found naturally especially in the areas of South Pacific. The main types of these materials

are quartz, tourmaline, sodium potassium tartarate, Rochelle salt etc. They are very sensitive to their cut and orientation due to their atomic structure. Ceramic materials which are not found in nature and artificially created by sintering finely ground powdered mixture made by ferroelectrics of the oxygen-octahedral type. They are named according to their material content like PZT : $Pb(Zr,Ti)O_3$, PT: $PbTiO_3$, PLZT : $(Pb,La)(Zr,Ti)O_3$. Ceramic materials are widely used in different application areas because of their advantages to crystalline materials. They are manufactured by several companies and they cost less than crystalline materials. On the other hand, they are much more sensitive than crystalline materials. This implies they have better piezoelectric material properties. However, ceramic materials exhibit very high temperature sensitivity. Piezoelectric properties can degrade by great extent when the temperature increases up to the "Curie Temperature" of the material. They have lack of stability because they can lose their polarization, tentative to mention aging and fatigue problems. In addition, they are brittle materials [3].

1.3   Physical Phenomena

Two main types of operation of piezoelectric devices are known to date.

Direct piezoelectric effect is the production of an electrical field when the material is mechanically stressed and converse piezoelectric effect is the deformation of piezoelectric materials when an electric field is applied to the electrodes of a piezoelectric material as in Figure 1.1.
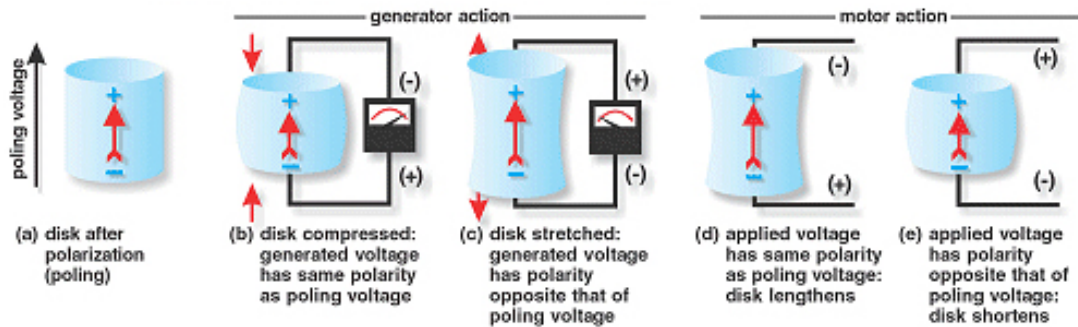
Figure 1.1 Schematic Drawings of Direct and Converse Piezoelectric Effect [8]

1.4   Typical Applications of Piezoelectric Materials

Piezoelectric materials are used widely in different application areas. Piezoceramic devices fit into four general categories, namely, generators, actuators, sensors and transducers [8].

Piezoelectric generators can generate voltages sufficient to spark across an electrode gap, and thus can be used as igniters in fuel lighters, gas stoves, welding equipment, and other such apparatus. Alternatively, the electrical energy generated by a piezoelectric element can be stored. Techniques produced have been developed to construct multilayer piezoelectric generators. Such generators are excellent solid state batteries for electronic circuits.

Piezoelectric actuators convert an electrical signal into a precisely controlled physical displacement, to finely adjust precision machining tools, lenses, mirrors etc. In piezoelectric sensors applications, the physical variable such as acceleration or pressure acts directly on the piezoelectric element and this excitation is converted into electrical signal.

4

Piezoelectric transducers convert electrical energy into mechanical energy, often sound or ultrasound, to perform tasks like generating ultrasonic vibrations for cleaning, atomizing liquids, drilling or milling ceramics etc. Piezoelectric materials technologies and their general applications are summarized in Table 1.1 [9].

Table 1.1 Piezoelectric Material Technology and Application Areas [9]

Technology	Applications
Piezoelectric generators	Energy source for munitions Energy source for wireless sensors, e.g. in tyres Energy source for lightning switches Gas igniters
Piezoelectric actuators	Micro & Nano positioning Vibration & noise control Valves & pumps Optics and photonics Ultrasonic motors Instrumentation
Piezoelectric sensors	Vibration and shock measurement Pressure and force measurement Flow and distance measurement Sound and noise measurement
Piezoelectric transducers	Communication devices Sonars Ultrasonic welding Ultrasonic cleaning

In time very interesting applications of piezoelectric materials have emerged. For example, POWERleap Company develops flooring systems that generates electricity from pedestrian and vehicular traffic. These flooring systems are applied in crowded places like dance clubs, train stations etc. [10]. Another example is the use of

piezoelectric materials to control the vibration in snowboards and skis. In these equipments, vibrations cause reduction of control in the board because of reduced edge contact with snow. The piezoelectric dampers reduce vibration of the board and allow a more precise control of the snowboard in any kind of snow condition [11].

1.5   Motivation for the Study

Recently developed smart or guided munitions require electrical power for their operation. The amount of electrical energy required for components such as fby, onboard RF receivers, low power sensors etc. is relatively low as a result of the developments of low power electronics. The power requirement is more if communication with a ground or a mobile station and becomes significant when the smart materials are equipped with actuators or similar devices for guidance and control purposes. Classical chemical batteries are not preferred because of their short shell life, low safety etc. as well as environmental regulations. They have the safety regulations by various corporations in their transportations [12] - [15]. Instead energy harvesters, electromagnetic or piezoelectric, with long shell life (up to 20 years or more) storage safety (e.g. zero power during storage and loading) and mechanical strength for operating in high g environments up to 120.000 g are preferred [16]. For small-calibre fuses, for instance, electrical energy requirement is about 3 mJ [17]. In this thesis, it is aimed to apply the piezoelectric elements technology to develop means for energy storage in munitions launch. The practical problems encountered in the design of piezoelectric energy harvesters are investigated. The applicability of energy harvesting to high power needs are studied. The experience compiled in the study is to be exploited in designing piezoelectric energy harvesters for munitions applications.

CHAPTER 2

PIEZOLECTRIC ELEMENTS TECHNOLOGY BACKGROUND

In this chapter, information about piezoelectric material properties, polarization of piezoelectric materials, modelling of piezoelectric behaviour, common shapes and loading conditions of piezoelectric materials. Literature survey is presented at the end of the chapter.

2.1   Piezoelectric Material Properties

Piezoelectric materials exhibit anisotropic properties. Anisotropic means properties are dependent on the direction within the material. Because of this reason, it is necessary to use a fixed axis scheme as in Figure 2.1.
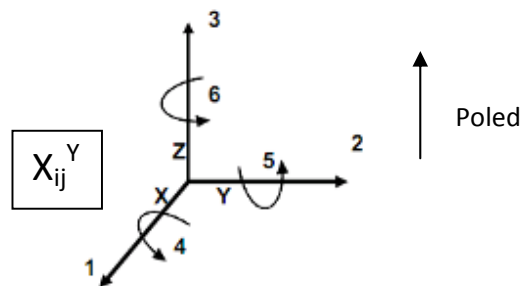
Figure 2.1 Piezoelectric Materials Axis Numbering Scheme

In Figure 2.1, X is the piezoelectric coefficient, i is the direction of electric field (1,2,3 or X,Y,Z), j is the direction of the mechanical strain or the stress (1,2,3,4,5,6 or X,Y,Z, YZ,ZX, XY) and Y is the specification of electrical or mechanical boundary conditions. As the superscript, T means constant stress condition where the material is unconstrained mechanically, S means constant strain where the material is mechanically constrained, E means constant electrical field where the short circuit conditions applied and D means constant electrical displacement where the open circuit conditions exist.

For the direct piezoelectric effect, piezoelectric constant d is the amount of the charge collected at the electrodes per unit of applied mechanical stress. The unit is Coulombs per Newton $[C / N]$. For the converse piezoelectric effect, this constant is the mechanical strain produced by per unit of applied electric field. For this condition, the unit is meters per volt $[m / V]$.

Piezoelectric voltage constant g is equal to the open circuit electric field per unit of applied mechanical stress for the direct piezoelectric effect. The unit is volts meters per Newton $[Vm / N]$. For the converse piezoelectric effect, it is the strain developed per unit of applied charge density or electrical displacement.

Electromechanical coupling coefficient k is square root of converted electrical energy per input mechanical energy for the direct piezoelectric effect and square root of converted mechanical energy per input electrical energy for the converse piezoelectric effect. The actual relationship is in terms of k^2 as in

$$k^2 = \frac{Converted\ Electrical\ Energy}{Input\ Mechanical\ Energy} \tag{2.1}$$

$$k^2 = \frac{Converted\ Electrical\ Energy}{Input\ Mechanical\ Energy} \qquad (2.2)$$

Typical values of k are 0.1 for quartz, 0.4 for barium titanate ceramic and 0.5-0.7 for PZTs.

Relative dielectric constant ε_r is the ratio of permittivity of a material, ε which is the dielectric displacement per electric field, to permittivity of free space which is vacuumed ε_0. Permittivity is the measure of how much resistance is encountered when forming an electric field in a medium. Thus, permittivity relates to ability of a material to transmit or "permit" an electric field. It is used in the calculation of the capacitance of the piezoelectric material. The unit of the permittivity is Farads per meter $[F/m]$.

Loss tangent $\tan \delta$ is the frequency dependent ratio of imaginary and real parts of the impedance of a capacitor. It is used in the calculation of loss resistance of piezoelectric material. High values of loss resistance mean a lot of dielectric absorption.

Young's modulus Y is the ratio of mechanical stress per unit of applied mechanical strain. The unit is Pascal $[Pa]$.

Elastic compliance, s, is the inverse of Young's modulus. The unit is meters square per Newton $[m^2/N]$.

Curie temperature, T_c is the limiting temperature at which the polarization of the material is lost. Typical Curie temperatures for PZT materials are in the order of 200 ^{0}C.

Frequency constant, N is the product of the resonance frequency and the linear dimension in the applied force direction. The unit is meters per second $[m/s]$ [8].

Mechanical quality factor, Q_m is a constant related with damping characteristics of the material. It is formulated as follows in terms of the damping ratio, ζ.

$$Q_m = \frac{1}{2\zeta} \qquad (2.3)$$

Thus, higher Q_m indicates a lower rate of energy loss relative to the stored energy of a resonator.

Efficiency of energy conversion, η for a clamped and cyclically compressed piezoelectric element at its resonant frequency is dependent on electromechanical coupling coefficient, k and mechanical quality factor, Q_m. The relationship is as in

$$\eta = \frac{\dfrac{k^2}{2(1-k^2)}}{\dfrac{1}{Q_m} + \dfrac{k^2}{2(1-k^2)}} \qquad (2.4)$$

It implies that higher efficiency of a piezoelectric energy harvester is provided by higher k and Q$_m$, which is a useful guideline when choosing piezoelectric materials for designing energy harvesters.

The piezoelectric properties can be lowered by ageing, high stress and temperature. The change in the properties of the piezoelectric materials is known as the ageing rate and dependent on the material type and physical conditions. The changes in the material are logarithmic with the time. For this reason, manufacturers of piezoelectric materials usually specify the piezoelectric constants after a specified period of a time. The ageing process is accelerated by the amount of the stress applied to ceramic material. This poses a very important problem in the cyclically loaded energy

10

harvesting applications [1]. In Figure 2.2, voltage decrease of a soft piezoelectric material due to different levels of applied mechanical stress is shown [18].
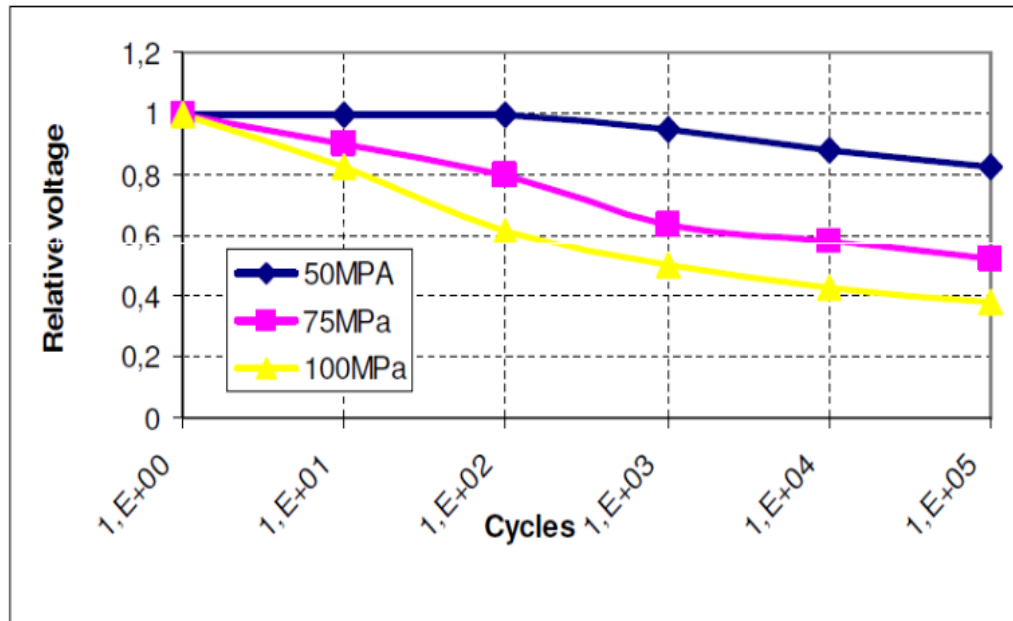
Figure 2.2 Voltage Decrease of a Soft Piezoceramic due to Different Mechanical Stress Levels [18]

2.2   Polarization of Piezoelectric Material Properties

Piezoelectric crystals are composed of very small piezo crystallites. Initially, dipoles which consist of a set of the same and opposite charges separated by a small distance are randomly oriented. Because of that, at macro level, piezoelectric behaviour cannot be achieved. Poling process is applied to align the dipoles properly [8]. Schematic drawing of poling process is as in Figure 2.3.

Random Dipole Polarization Surviving Polarity

Electrodes
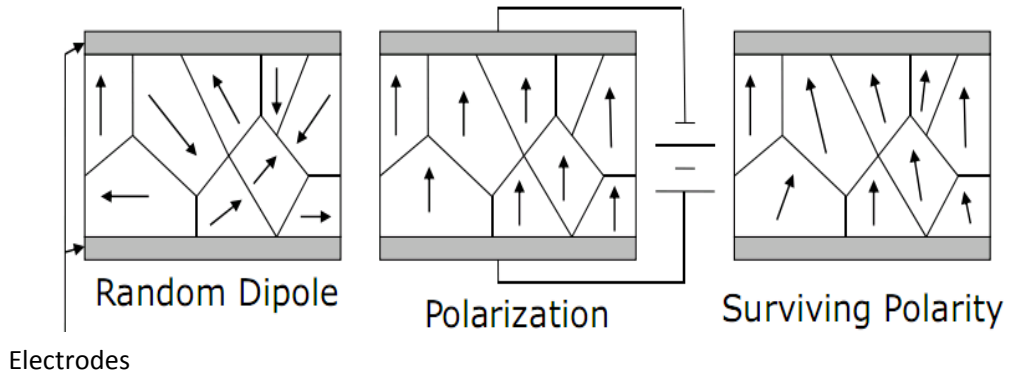
Figure 2.3 Schematic Drawing of Poling Process [8]

Applied poling field determines the maximum voltage production capability of piezoelectric material, V_{max} equals to poling field voltage, V_{pf} times thickness of the piezoelectric material, t_{pz} according to the below formula [21].

$$V_{max} = V_{pf} t_{pz} \tag{2.5}$$

2.3 Modelling of Piezoelectric Behaviour

Modelling of piezoelectric behaviour is based on having linear piezoelectric constitutive equations by interrelating linear elasticity constitutive equations with electrostatic charge equations through piezoelectric constants as in Figure 2.4.
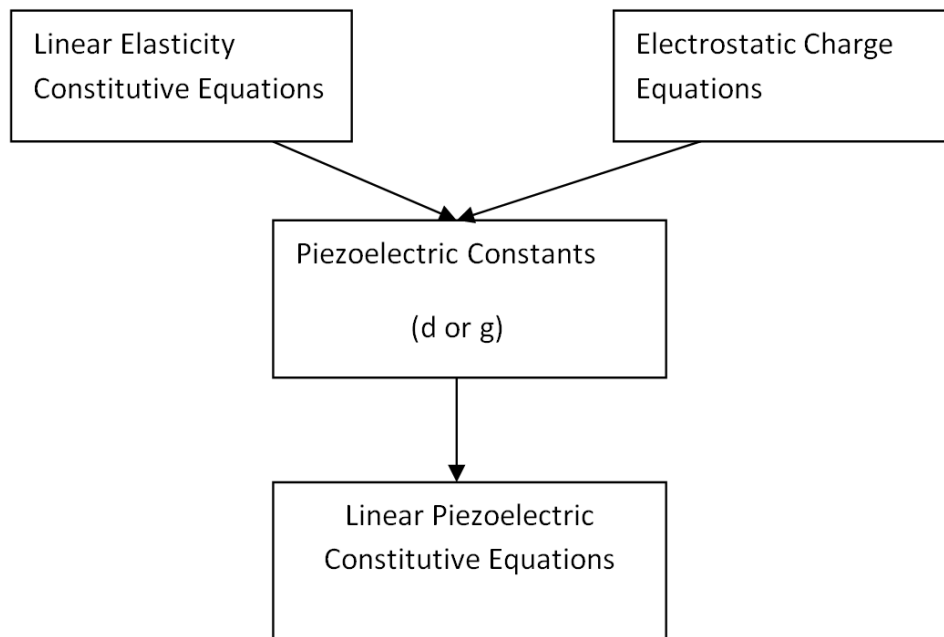
Figure 2.4 Modelling of Piezoelectric Behaviour Diagram

The electromechanical behaviour of piezoelectric materials can be modelled by two matrix equations for direct and converse piezoelectric effects.

For direct piezoelectric effect

$$\{D\} = [e]^T \{S\} + [\alpha^s]\{E\} \tag{2.6}$$

For converse piezoelectric effect

$$\{T\} = [c^E]\{S\} - [e]\{E\} \tag{2.7}$$

13

where $\{D\}$ is the electrical displacement vector, $[e]$ is piezoelectric stress matrix, $\{S\}$ is the strain vector, $[\alpha^s]$ is the dielectric matrix at constant mechanical strain, $\{E\}$ is the electrical field vector, $\{T\}$ is the stress vector and $[c^E]$ is the matrix of elastic coefficients at constant electrical field [19].

2.4   Common Shapes and Loading Conditions of Piezoelectric Materials

Piezoelectric materials are categorized as "soft" and "hard" ceramics according to their ease of depolarization.

Soft piezoelectric materials are produced by addition of donor dopant(s) to create metal (cation) vacancies in the crystal structure of the material [9]. An example of "soft" PZT material is shown in Figure 2.5 [4].

Hard piezoelectric materials are produced by addition of acceptor dopant(s) to create oxygen (anion) vacancies in crystal structure of piezoelectric ceramic [9]. "Hard" does not address mechanical hardness. It refers to meaning of "hard to depolarize" by application of forces etc. An example of "hard" PZT material is shown in Figure 2.6 [4]. The material properties of soft and hard ceramics are compared in Table 2.1[8].
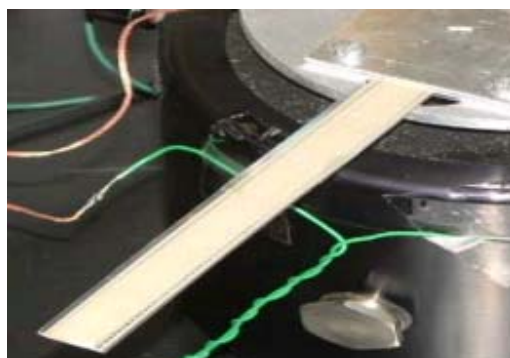
Figure 2.5 Soft PZT-5A Material [4]
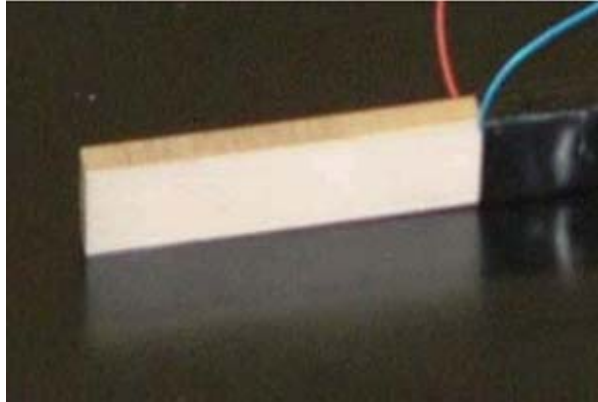
Figure 2.6 Hard PZT Material [4]

Table 2.1 Comparison of Characteristics for Soft and Hard Ceramic Materials [8]

Characteristic	*Soft Ceramic*	*Hard Ceramic*
Piezoelectric Constants	Larger	Smaller
Permittivity	Higher	Lower
Dielectric Constants	Larger	Smaller
Dielectric Losses	Higher	Lower
Electromechanical Coupling Factors	Larger	Smaller
Electrical Resistance	Very High	Lower
Mechanical Quality Factors	Low	High
Coercive Field	Low	Higher
Linearity	Poor	Better
Polarization / Depolarization	Easier	More Difficult

Soft piezoelectric elements are more sensitive to mechanical stress than hard piezoelectric elements. It is shown that hard-doped material is much more resistant than soft-doped material against degradation as in Figure 2.7 [18].

Piezoelectric materials can have different shapes, loading and boundary conditions according to their application area. In Figure 2.8, in column "a", the plate shaped piezoelectric elements are loaded longitudinally. In column "b", the plate shaped elements are loaded in shear mode. In column "c", rod-shaped elements are loaded axially. In column "d" hollow cylinder and truncated cone shaped materials which can only be produced of piezoelectric ceramics are shown. In column "e", bimorph piezoelectric elements which consist of two "soft" piezoceramics and one middle substructure like aluminium in bending mode are shown. In column "f", torsion sensitive piezoelectric elements are shown [4].

Test condition: 10Hz, 50MPa
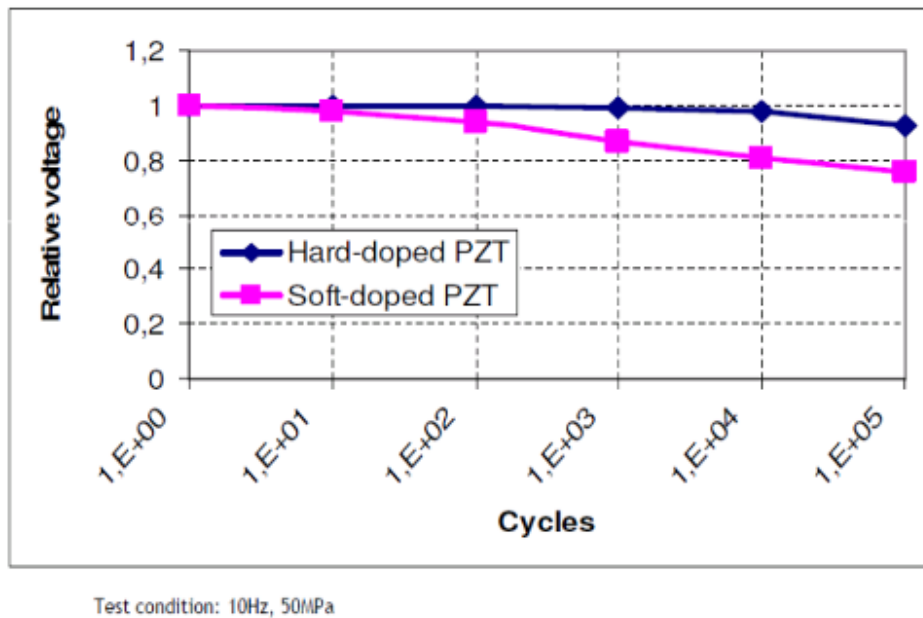
Figure 2.7 Comparison of Voltage Decrease for Soft and Hard Piezoelectric Elements [18]
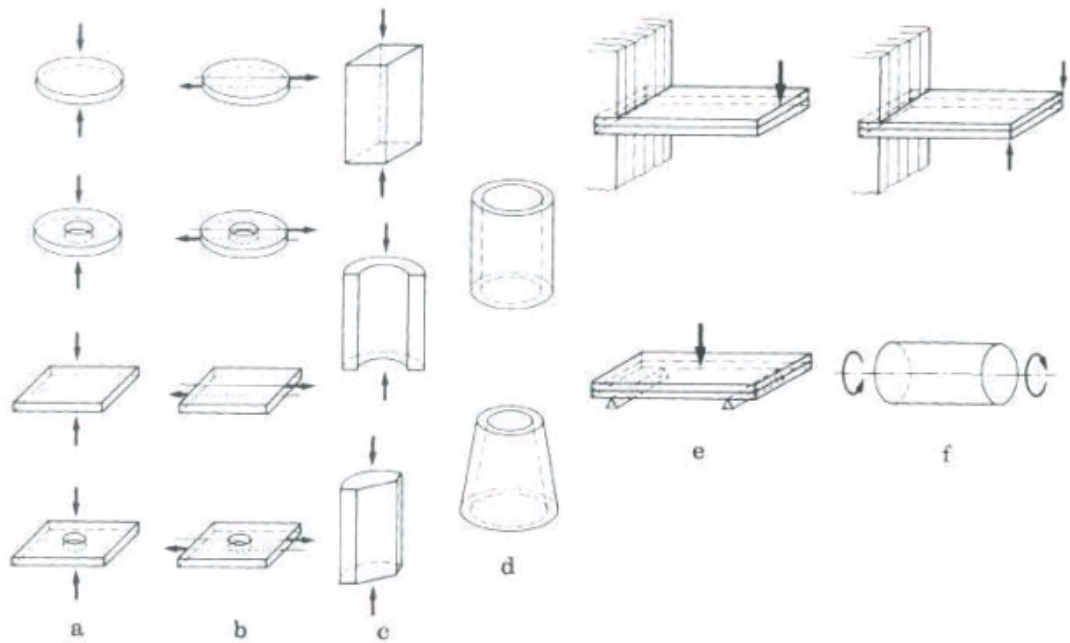
Figure 2.8 Different Piezoelectric Element Shapes, Loading and Boundary
Conditions [4]

2.5   Literature Survey

2.5.1   High Power Applications of Piezoelectric Generators

Pearson [4] aimed to examine the properties of piezoelectric materials and to develop
a system that will allow a designer to employ these devices in energy harvesters. He
was interested in supplying electrical energy to the on-board electronics of a sample
munitions by piezoelectric energy harvesters instead of chemical batteries since these
batteries are bulky and their operation is not reliable under high acceleration
environments. He modelled a mass-spring resonator system which applies the force
to the piezoelectric element under high acceleration environments. He used

MATLAB® with the Simulink package to simulate the mechanical side of the piezoelectric material, along with a resonator and to simulate the internal voltage generation of the piezoelectric material. To complete the electrical simulation of the materials, an equivalent circuit model was used along with ORCAD PSPICE® which is a circuit simulator program. The simulation results were compared with the experimental results which are conducted by the piezoelectric resonator systems of a company and drop test setup which can produce accelerations up to 15000 g's. The results were not consistent. The reason was most probably the modelling errors of the resonators.

In another project, Pearson [20] made the steady state test, drop tests and impedance tests with hard piezoceramics, soft piezoceramics, bimorph materials and piezoelectric resonator systems. He also studied on the linearity check of soft piezoceramics.

Pinkston [21] investigated a high energy piezoelectric pulse generator (PPG) constructed from commercially available piezoelectric materials. The large internal capacitance in the high energy PPG was created by stacking numerous single-element piezoelectric devices and electrically connecting them in parallel. The total internal capacitance of the PPG was around 0.15 μF. The high energy PPG is piezoelectrically charged to greater than 1 kV, thereby storing 50 mJ. An electromechanical model of the PPG was developed in ORCAD PSPICE® as lumped-element system and used to predict the performance of the high PPG under a variety of conditions. The ORCAD PSPICE® simulations were compared to experimental test results with mechanical force rise-times ranging from sub-millisecond to several milliseconds. Experimentally, the force needed to compress is derived from a steel mass dropped from variable heights and neoprene material to control the force. In variety of force values, the simulation results were compared with experimental results. Peak forces around 18 kN were produced to compress the piezoelectric material. It was shown that, even after further increasing the force value after some value, the produced voltage could not be increased because of the

maximum voltage producing capability of piezoelectric stack. Theoretical and experimental results were not in very good agreement.

Keawboonchuay et al. made several studies [22] - [26] in piezoelectric energy harvesting area in high power applications. In "Electrical Power Generation Characteristics of Piezoelectric Generator Under Quasi-Static and Dynamic Stress Conditions" [22], the characteristics of a piezoelectric power generator was investigated under quasi-static (duration > 100 ms) and dynamic (stress duration < 10 ms) stress applications. The lumped parameter electromechanical model of piezoelectric generator were presented and used to explain the effects of the two stress conditions. The simulations predicted that a quasi-static stress would produce a bidirectional generator output voltage, and a dynamic stress would produce a unidirectional output voltage. The simulation also showed that, when equal stresses are applied to the generator, the dynamic stress would generate ten times higher output voltage than the quasi-static stress because of the generator's resistive capacitive time constant. The simulation results were experimentally verified.

In "Design, Modelling, and Implementation of a 30-kW Piezoelectric Pulse Generator" [23], the design and modelling of a high power piezoelectric pulse generator was discussed. This study presented theoretical description of the pulse generator as well as methods to implement it in the simulation by a lumped parameter electromechanical model. Techniques to model the diagnostic system that measures the generator output were presented. Two kinds of experiments, piezoelectric projectile and bench test, were performed on the piezoelectric pulse generator to compare the results with the simulations. Barium titanate was used as the piezoelectric material. In the piezoelectric projectile test, the experimental results and the simulation results were not in good agreement due to the problem with the diagnostic system. Experimentally, the peak current, peak power, and power density were 58.2 A, 28.4 kW, and 517 kW/cm^3, respectively while in simulations these values were 60.9 A, 37.8 kW, and 2256.6 kW/cm^3, respectively. In the bench test,

the results were very well agreed with the simulations. Experimentally, the peak current, peak power and power density were 36 A, 15.6 kW, and 96.7 kW/cm^3, respectively while in simulations these values were 40.2 A, 19.4 kW, and 120.3 kW/cm^3, respectively.

In "Energy Conversion and High Power Pulse Production By Miniature Piezoelectric Compressors" [24], the design, construction, and testing of high-power piezoelectric compression generators were discussed. The piezoelectric compression generators were located inside high speed, 30-mm projectiles that were launched with a high pressure helium gun to velocities of approximately 300 m/s. The large deceleration force created when the projectile impacts the ground is used to power the piezoelectric compression generator. The peak output power is approximately 25 kW into a 10 ohms load with the output pulse duration in the order of 1 s.

In "Maximum Power Generation in a Piezoelectric Pulse Generator" [25], maximization of the power techniques for a high-power piezoelectric pulse generator was discussed. The theoretical results implied that the peak stack voltage would increase with an increasing thickness to area ratio of the piezoelectric material and with increasing applied force. However, in contrast to the peak output voltage, the peak output current would increase with the decreasing of thickness to area ratio of the material. The output power of the piezoelectric generator, which is the product of output voltage and current, linearly increases with the thickness to area ratio. Experimental results were also presented to verify the theoretical results and to represent the performance of several types of piezoelectric materials with different thickness to area ratios.

In "Scaling Relationships and Maximum Peak Power Generation in a Piezoelectric Pulse Generator" [26], the factors affecting the maximum peak power of a piezoelectric pulse generator were presented also considering the mechanical strength limitations. These factors were defined as the piezoelectric material's thickness to area ratio, the mechanical compression force, the material's stress

limitation, and external circuit conditions. It was implied that maximum peak power increased with increasing piezoelectric material volume; however, mechanical stress limitations should also be considered. The highest peak power measured in this study was 320 kW by a cylindrically-shaped piezoelectric material with 0.89-cm diameter and 1.27-cm height, which translates into a power density of 405.06 kW/cm^3.

Rastegar et al. [27] presented piezoelectric-based energy-harvesting power sources for gun-fired munitions and other similar applications that require very high acceleration survivability. The power sources were designed to harvest energy from the firing acceleration as well as vibratory motion of munitions during the flight and convert it to electrical energy to power onboard electronics. The developed piezoelectric-based energy harvesting power sources harvested enough electrical energy for applications such as fusing. The power sources were designed to withstand firing accelerations in excess of 100,000 g. The design of a number of prototypes, including their packaging for high g hardening, and the results of laboratory and air-gun testing were presented. Methods to increase the efficiency of high acceleration energy-harvesting power sources and minimize friction and damping losses were discussed.

2.5.2   Other Applications of Piezoelectric Generators

Ertürk [2] presented distributed-parameter electromechanical models that can accurately predict the coupled dynamics of piezoelectric energy harvesters to as opposed to lumped-parameter electromechanical models. He mostly worked on cantilevered bimorph piezoelectric energy harvesters. The lumped-parameter electromechanical formulation was corrected by introducing a dimensionless correction factor derived from the electromechanically uncoupled distributed-parameter solution for the transverse vibrations and longitudinal vibrations of structures according to the tip mass. Then, the electromechanically coupled closed-form analytical solution was obtained based on the thin-beam theory as piezoelectric energy harvesters concentrated in this work was typically thin cantilevered bimorph

piezoelectric generators. The multi-mode electromechanical frequency response expressions obtained from the analytical solution were reduced to single-mode expressions for modal vibrations. The analytical solutions for the electromechanically coupled voltage response and vibration response were validated experimentally for various cases. The single-mode analytical equations were used for deriving closed-form relations for parameter identification and optimization. A simple experimental technique was presented to identify the optimum load resistance by only a single resistor and an open-circuit voltage measurement. A case study was studied to compare the power generation performances of commonly used monolithic piezoceramics and novel single crystals with a focus on the effects of plane-stress material constants and mechanical damping. The effects of strain nodes and electrode configuration on piezoelectric energy harvesting were discussed theoretically and demonstrated experimentally. An approximate electromechanical solution by the assumed-modes method was presented for modelling of asymmetric and moderately thick energy harvester configurations. In addition, a piezo-magneto-elastic energy harvester was introduced as a non-conventional broadband energy harvester.

Lesieutre et al. [28] studied damping characteristics as a result of energy harvesting by piezoelectric materials due to the fact that the removal of mechanical energy from a vibrating structure necessarily results in damping. They had the discussions about the damping associated with a piezoelectric energy harvesting system that consisted of a full-bridge rectifier, a filter capacitor, a switching DC–DC step-down converter, and a battery. For this system, under conditions of harmonic forcing, the effective modal loss factor was dependent on the electromechanical coupling coefficient of the piezoelectric system and the ratio of the rectifier output voltage during operation to its maximum open circuit value. Related formulas were presented.

Challa et al. [29] studied on designing a resonant frequency tuneable energy harvesting device by a mechanism including permanent magnets. They designed and tested a resonance frequency tuneable energy harvesting device applying magnetic

forces. Attractive and repulsive magnetic forces were employed to tune the device to resonance frequencies that are either greater or less than the untuned resonance frequency of the device. It was found that these magnetic forces could change the resonance frequency of a cantilevered beam up to ±20 % of the untuned resonance frequency. It was shown that by this tuning technique, a wide frequency working range vibration energy harvesting is feasible without sacrificing the output power.

CHAPTER 3

THEORY

In this chapter, analytical and numerical approaches to model the electro-mechanical behaviour of piezoelectric materials are proposed. In the first part of the analytical calculations, the mechanical relations are discussed. Two main techniques exist to produce the strain in piezoelectric materials in high power applications. The first technique is replacement of a mechanical resonator having some stiffness, damping and mass on the top of the piezoelectric material to apply a force related with deformation of the resonator due to acceleration of the environment. The second and easier way of applying force is replacement of a mass by means of a bolt or glue to compress the piezoelectric material. Another important issue is mechanical modelling of piezoelectric materials. Firstly, they can be modelled as a rigid body and the electrical charge can directly be calculated by the compression force and some electrical parameters. Alternatively, the piezoelectric material is modelled as a single degree of freedom lumped parameter model and the strain is calculated. The electrical parameters can be predicted from the calculated strain. As a third way, the piezoelectric material is modelled as a continuous material and the strain is calculated by distributed parameter modelling approach. In the second part, the electrical relations are discussed. The quasi-static and dynamic loading cases and corresponding relations are outlined. Bulk and multilayer characteristics of piezoelectric materials and the reasons of applying multilayer ceramics in the high power applications are investigated. The corresponding electrical circuit models of piezoelectric materials are discussed. In the numerical approach, finite element

software ATILA$^{®}$ is used. The theory used in this program for the piezoelectric energy harvester analysis is discussed.

3.1 Analytical Modelling of High Power Piezoelectric Systems

3.1.1 Mechanical Modelling of High Power Piezoelectric Systems

As mentioned before, mechanical resonators are used to apply the force to compress the piezoelectric materials. The schematic drawing of a piezoelectric energy harvester resonator system which is a product of Omnitek Company is as in Figure 3.1 [30]. These kinds of resonator systems can be designed with optimum natural frequency of the vibration mass-spring unit according to specific application conditions [16].
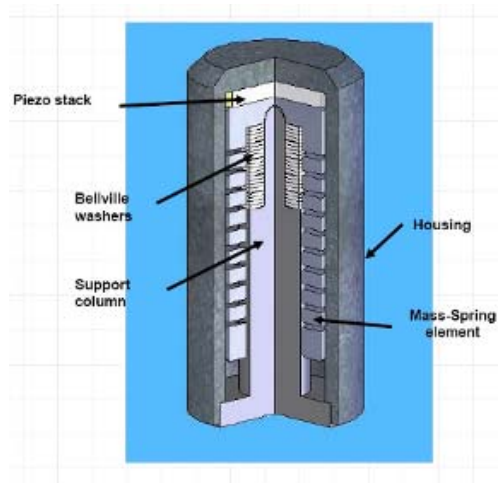
Figure 3.1 Piezoelectric Energy Harvester Resonator System [30]

The second way of applying the compression force to the piezoelectric material is replacing mass on the top surface of the piezoelectric material by means of a bolt or glue. This way of usage is schematized in Figure 3.2.
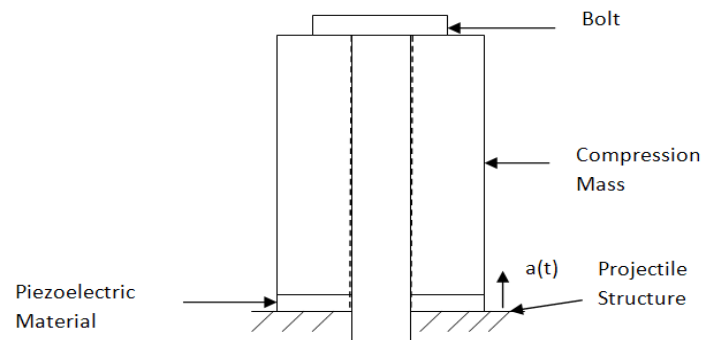
Figure 3.2 Piezoelectric Energy Harvester Compression Mass System

This mass can compress the piezoelectric material with forcing function, $F_{pz}(t)$ because of the acceleration of the environment, $a(t)$ related with

$$F_{pz}(t) = ma(t),$$
(3. 1)

where m is the compression mass.

3.1.1.1   Analytical Modelling of Mechanical Resonators

The usage of mechanical resonators in gunfire applications is modelled as in Figure 3.3.
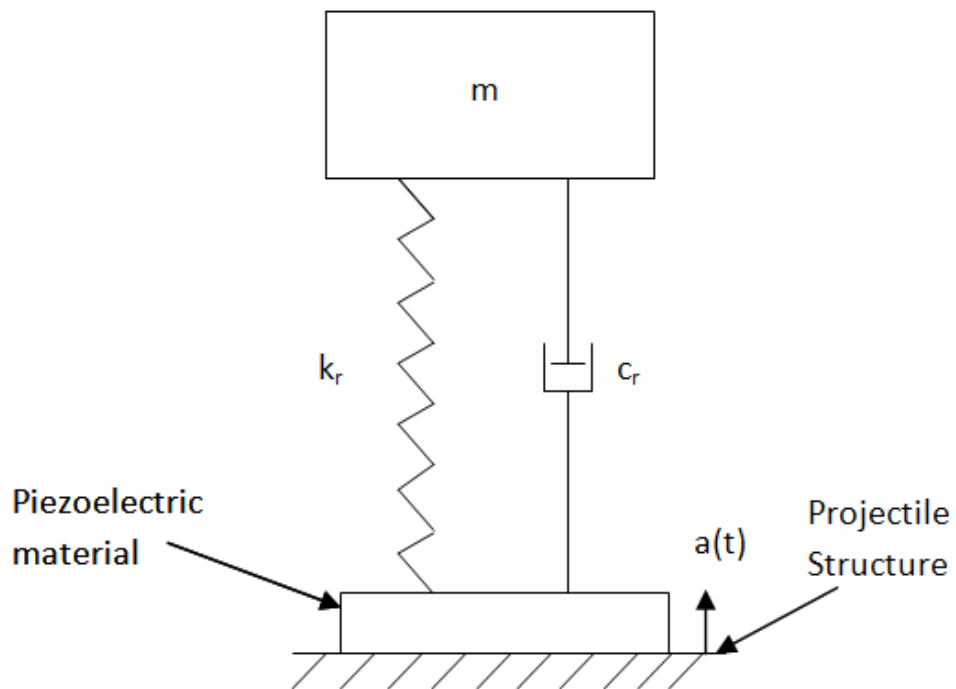
Figure 3.3 Resonator Model

In gunfire applications, the excitation is caused by the acceleration of the projectile. A sample acceleration profile for a 155 mm calibration gun is displayed in Figure 3.4 [4].

m/s²
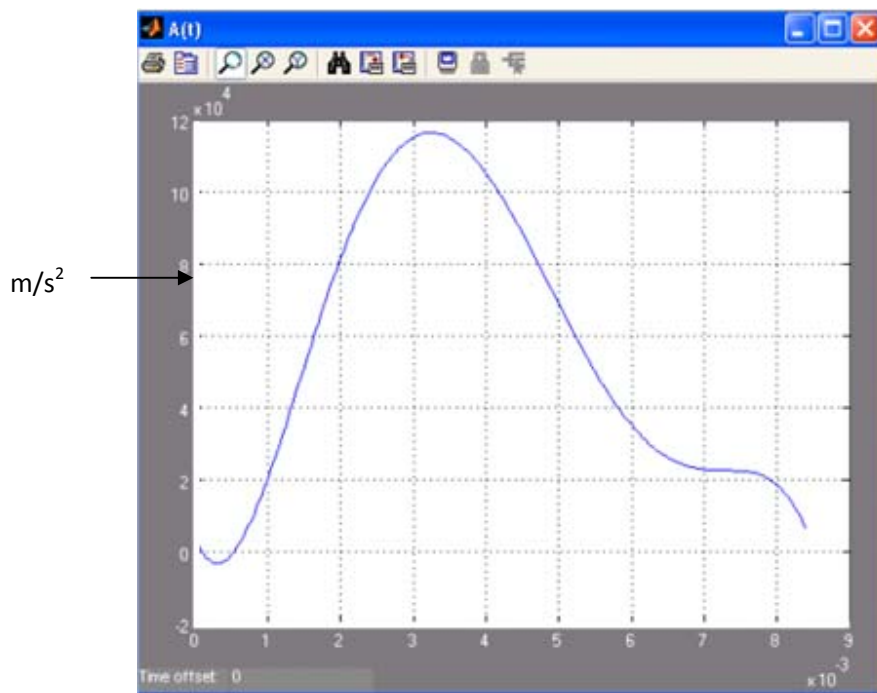
Figure 3.4 Sample Acceleration Data [4].

This excitation is a neither harmonic nor periodic excitation. Because of that feature, the displacement response of this single degree of freedom system is calculated by Laplace Transform Method [31].

Firstly, the equation of motion of a damped single degree of freedom system is as in

$$m\,\ddot{x}(t) + c_r\,\dot{x}(t) + k_r x(t) = F(t)\,,\tag{3.2}$$

where c_r is the damping and k_r is the stiffness of the resonator, $F(t)$ is the forcing function created on the resonator, $x(t)$ is the displacement response, $\dot{x}(t)$ and $\ddot{x}(t)$ are

first and second derivatives of the displacement response of the resonator, respectively.

For the system in Figure 3.3, forcing function in the resonator, $F(t)$ is calculated as

$$F(t) = ma(t).$$ (3. 3)

By Laplace Transform Method, both sides of Eq. (3. 2) is transformed and the equation is obtained as

$$(ms^2 + c_r s + k_r)X(s) = F(s) + m\dot{x}(0) + (ms + c_r)x(0).$$ (3. 4)

In this equation, $\dot{x}(0) = v_0$ and $x(0) = x_0$ are initial velocity and displacement of mass, m.

By Eq.(3.4), the transformed response is in the form of

$$X(s) = \frac{F(s)}{m(s^2 + 2\zeta w_n s + w_n^2)} + \frac{s + 2\zeta w_n}{s^2 + 2\zeta w_n s + w_n^2} x_0 + \frac{1}{s^2 + 2\zeta w_n s + w_n^2} v_0$$ (3. 5)

In this equation, w_n is the natural frequency and ζ is the damping ratio of the system which are calculated by

$$w_n = \sqrt{\frac{k_r}{m}},$$ (3. 6)

$$\zeta = \frac{c_r}{2mw_n}.$$ (3. 7)

The right-hand side of Eq. (3. 5) is considered separately to carry out the inverse transformation of $X(s)$. To let this the functions are defined as

$$F_1(s) = F(s), \qquad F_2(s) = \frac{1}{m(s^2 + 2\zeta w_n s + w_n^2)}. \qquad (3.8)$$

By the table of Laplace transforms pairs, $f_1(t)$ and $f_2(t)$ are calculated as

$$f_1(t) = F(t), \qquad (3.9)$$

$$f_2(t) = \frac{1}{mw_d} e^{-\zeta w_n t} \sin w_d t, \qquad (3.10)$$

where w_d is the damped natural frequency of the resonator which is calculated by

$$w_d = w_n \sqrt{1-\zeta^2}. \qquad (3.11)$$

By the convolution theorem, the inverse transformation of the first term of right-hand side of Eq. (3.5) is

$$L^{-1}\{F_1(s)F_2(s)\} = \int_0^t f_1(\tau)f_2(t-\tau)d\tau = \frac{1}{mw_d} \int_0^t F(\tau)e^{-\zeta w_n(t-\tau)} \sin w_d(t-\tau)d\tau . (3.12)$$

The inverse transform of the second term of right-hand side of Eq. (3.5) is obtained by the table of Laplace transforms pairs as in

$$L^{-1}\left\{\frac{s + 2\zeta w_n}{s^2 + 2\zeta w_n s + w_n^2}\right\} = \frac{w_n}{w_d} e^{-\zeta w_n t} \cos(w_d t - \psi), \qquad (3.13)$$

where

30

$$\psi = \tan^{-1} \frac{\zeta w_n}{w_d}. \tag{3. 14}$$

The inverse transform of the last term of right-hand side of Eq. (3.5) can be obtained by multiplying $f_2(t)$ which is obtained by Eq. (3.10) by mass, m.

The general response of the system in Figure 3.3 is then calculated as

$$x(t) = \frac{1}{mw_d} \int_0^t F(\tau) e^{-\zeta w_n (t-\tau)} \sin w_d (t-\tau) d\tau + x_0 \frac{w_n}{w_d} e^{-\zeta w_n t} \cos(w_d t - \psi)$$

$$+ \frac{v_0}{w_d} e^{-\zeta w_n t} \sin w_d t. \tag{3. 15}$$

Finding the response of the resonator the force exerted on the piezoelectric material can be found by

$$F_{pz}(t) = k_r x(t) + c_r \dot{x}(t). \tag{3. 16}$$

3.1.1.2   Analytical Modelling of Piezoelectric Materials

Mainly, since the piezoelectric materials have anisotropic material properties, their characteristics are being found through the matrix equations as

$$\begin{bmatrix} S_1 \\ S_2 \\ S_3 \\ S_4 \\ S_5 \\ S_6 \end{bmatrix} = \begin{bmatrix} s_{11}^E & s_{12}^E & s_{13}^E & 0 & 0 & 0 \\ s_{21}^E & s_{22}^E & s_{23}^E & 0 & 0 & 0 \\ s_{31}^E & s_{32}^E & s_{33}^E & 0 & 0 & 0 \\ 0 & 0 & 0 & s_{44}^E & 0 & 0 \\ 0 & 0 & 0 & 0 & s_{55}^E & 0 \\ 0 & 0 & 0 & 0 & 0 & s_{66}^E \end{bmatrix} \begin{bmatrix} T_1 \\ T_2 \\ T_3 \\ T_4 \\ T_5 \\ T_6 \end{bmatrix} + \begin{bmatrix} 0 & 0 & d_{31} \\ 0 & 0 & d_{32} \\ 0 & 0 & d_{33} \\ 0 & d_{24} & 0 \\ d_{15} & 0 & 0 \\ 0 & 0 & 0 \end{bmatrix} \begin{bmatrix} E_1 \\ E_2 \\ E_3 \end{bmatrix}, \tag{3. 17}$$

$$\begin{bmatrix} D_1 \\ D_2 \\ D_3 \end{bmatrix} = \begin{bmatrix} 0 & 0 & 0 & 0 & d_{15} & 0 \\ 0 & 0 & 0 & d_{24} & 0 & 0 \\ d_{31} & d_{32} & d_{33} & 0 & 0 & 0 \end{bmatrix} \begin{bmatrix} T_1 \\ T_2 \\ T_3 \\ T_4 \\ T_5 \\ T_6 \end{bmatrix} + \begin{bmatrix} \varepsilon_{11} & 0 & 0 \\ 0 & \varepsilon_{22} & 0 \\ 0 & 0 & \varepsilon_{33} \end{bmatrix} \begin{bmatrix} E_1 \\ E_2 \\ E_3 \end{bmatrix}. \qquad (3.\ 18)$$

In high power applications for munitions, because of the mechanical strength limitations, the piezoelectric materials are used in compression mode. In this mechanical mode, the electrodes are used perpendicular to the poling direction, 3rd direction in Figure 2.1. Since both the mechanical and the electrical direction is the 3rd direction, it is called "33" mode usage of piezoelectric materials. This usage mode is schematized in Figure 3.5.
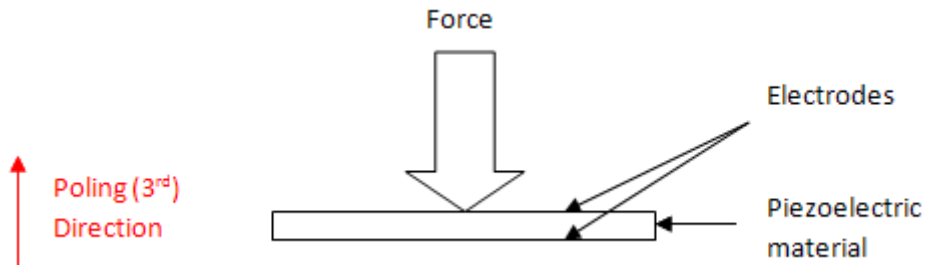
Figure 3.5 Piezoelectric Material 33 mode Usage Scheme

Accordingly, Eq. (3.17) and (3.18) are simplified as in Eq. (3.19) and (3.20), respectively.

$$S_3 = s_{33}^E T_3 + d_{33} E_3, \qquad (3.\ 19)$$

$$D_3 = d_{33}T_3 + \varepsilon_{33}E_3. \tag{3. 20}$$

3.1.1.2.1   Calculation of the Electrical Parameters by Applied Force

To calculate the electrical parameters of piezoelectric materials, the applied force on the piezoelectric material can be used to calculate the created charge, Q as

$$Q = d_{33}F. \tag{3. 21}$$

In this method, compression stress can be calculated as

$$T_3 = \frac{F}{A_{pz}}. \tag{3. 22}$$

By this model, the dynamic parameters of piezoelectric materials are not taken into account.

3.1.1.2.2   Calculation of the Electrical Parameters by Mechanical Stress

In this method, the mechanical strain and stress in piezoelectric material calculated by modelling the piezoelectric material both lumped parameter and distributed parameter modelling methods.

3.1.1.2.2.1 Lumped Parameter Modelling

In this section, piezoelectric material is modelled as a single degree of freedom system as in Figure 3.6.
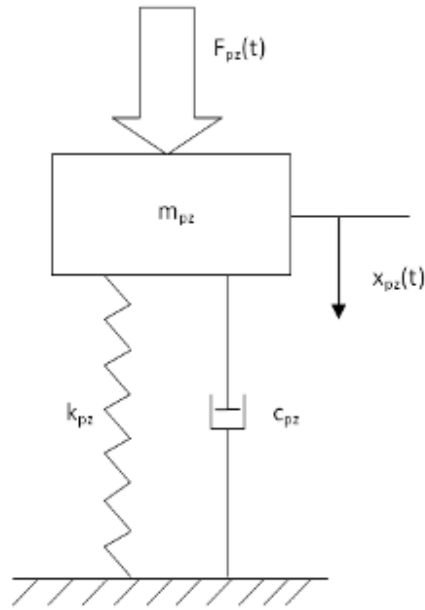
Figure 3.6 Lumped Parameter Mechanical Modelling of Piezoelectric Material

To calculate the stress by this model, the same analogy with Section 3.1.1.1 is used. Displacement response, which is concluded in Eq. (3.15) with zero initial velocity and displacement input, is

$$x_{pz}(t) = \frac{1}{m_{pz} w_{dpz}} \int_0^t F_{pz}(\tau) e^{-\zeta_{pz} w_{npz}(t-\tau)} \sin w_{dpz}(t-\tau) d\tau ,$$

(3. 23)

where m_{pz} is the mass, w_{npz} is the natural frequency, w_{dpz} is the damped natural frequency, ζ_{pz} is the damping ratio of the piezoelectric material. The damping ratio of the piezoelectric materials can be found by the mechanical quality factor, Q_m of them which is displayed in the material data sheet as

$$\zeta_{pz} = \frac{1}{2Q_m} \,. \tag{3.24}$$

To get the displacement response of the system by Eq. (3.23), it is necessary to have the forcing function depending on time. However, it is impossible to fit the function especially in shock environments. As an alternative method in such cases, the forcing function in time domain transferred to frequency domain by taking the Fast Fourier Transform (FFT) as

$$F_{pz}(\omega) = \mathcal{F}\left(F_{pz}(t)\right), \tag{3.25}$$

where $\mathcal{F}$ symbolizes FFT algorithm.

Frequency response function of single degree of freedom system in Figure 3.6, $H_{pz}(\omega)$ is calculated as

$$H_{pz}(\omega) = \frac{1}{-\omega^2 m_{pz} + k_{pz} + i\omega\, c_{pz}}, \tag{3.26}$$

where ω is frequency.

Displacement response of the piezoelectric material in frequency domain, $X_{pz}(w)$ is calculated as

$$X_{pz}(\omega) = H_{pz}(\omega)F_{pz}(\omega).$$ (3. 27)

To transfer the displacement response to time domain, the real part of inverse FFT of $X_{pz}(\omega)$ is calculated as

$$x_{pz}(t) = real(\ \mathscr{F}^{-1}(X_{pz}(\omega)))),$$ (3. 28)

where $\mathscr{F}^{-1}$ symbolizes inverse FFT algorithm.

The strain, $S_3(t)$ can be calculated by dividing it by the height of the piezoelectric material, h_{pz} as

$$S_3(t) = \frac{x_{pz}(t)}{h_{pz}}.$$ (3. 29)

Multiplying the strain created in piezoelectric material with the modulus of elasticity, Y_{33}, the stress, T_{pz} can be found as follows

$$T_3(t) = S_3(t)Y_{33}.$$ (3. 30)

Generally, in the piezoelectric materials' datasheet, elastic compliance, s, values are illustrated instead of the modulus of elasticity. The modulus of elasticity can be found by taking the inverse of the related elastic compliance value as

$$Y_{33} = \frac{1}{s_{33}}.$$ (3. 31)

The electrical field can be calculated by multiplying it with piezoelectric voltage constant, g as

$$E_{33}(t) = T_3(t)g_{33}.$$
<div align="right">(3. 32)</div>

The other electrical terms can be calculated by the electrical field value. This will be discussed in the following related sections. In this approach, the dynamic characteristics of the piezoelectric element are taken into account. However, if the second or more resonance frequencies are efficient, their effect is not taken into account.

3.1.1.2.2.2 Distributed Parameter Modelling

In this section, the piezoelectric material is modelled as in Figure 3.7. The distributed parameter solution for the systems with external forces at boundaries is used; it is fixed at $x = 0$ and applied an axial force at $x = h_{pz}$ [31].
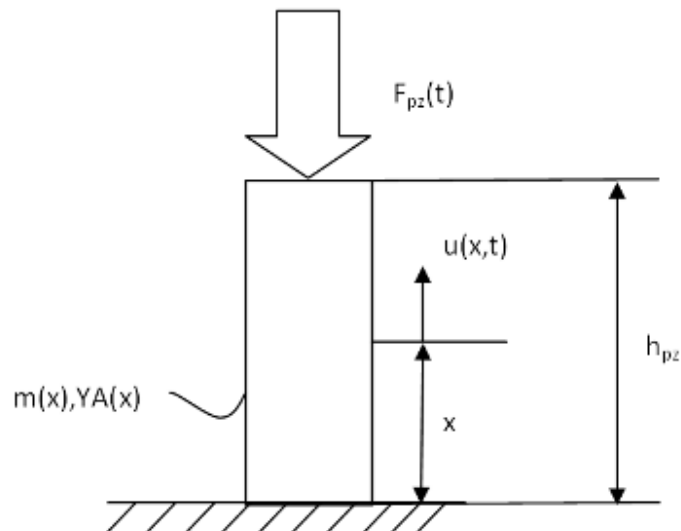
Figure 3.7 Distributed Parameter Model of Piezoelectric Material

The initial conditions, displacement and velocity, are assumed to be zero. The partial differential equation of the system is as in

$$\frac{\partial}{\partial x}\left[Y_{33}A(x)\frac{\partial u(x,t)}{\partial x}\right] = m(x)\frac{\partial^2 u(x,t)}{\partial t^2}, \qquad 0 < x < h_{pz}, \qquad (3.33)$$

where Y_{33} is the modulus of elasticity, $A(x)$ is the cross-sectional area and $m(x)$ is the mass per length of the piezoelectric material.

Displacement response, $u(x,t)$ must satisfy the boundary conditions

$$u(0,t) = 0, \qquad (3.34)$$

$$Y_{33}A(x)\frac{\partial u(x,t)}{\partial x}\Big|_{x=h_{pz}} = F_{pz}(t). \qquad (3.35)$$

Since the second boundary condition, Eq. (3.35) is non-homogenous; applying the modal analysis for the response is not possible. To simplify the solution of Eq. (3.27), the forcing function, $F_{pz}(t)$ is treated as distributed over $h_{pz}^- < x < h_{pz}$ as in Figure 3.8. h_{pz}^- is used to denote a point to the immediate left of $x = h_{pz}$.

The equivalent distributed force can be calculated by

$$f(x,t) = F_{pz}(t)\delta(x - h_{pz}), \qquad (3.36)$$

where $\delta(x - h_{pz})$ is the Dirac delta function defined as

$$\delta(x - h_{pz}) = 0, \quad x \neq h_{pz},$$

$$\int_0^L \delta(x - h_{pz})dx = 1.$$

(3. 37)
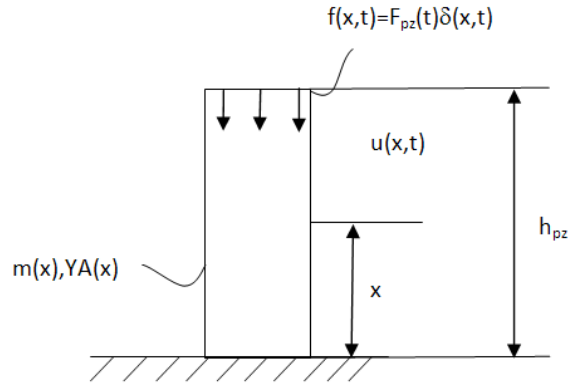
Figure 3.8 Distributed Forcing Symbolization

Eq. (3.33) is then formed as

$$\frac{\partial}{\partial x}\left[Y_{33}A(x)\frac{\partial u(x,t)}{\partial x}\right] + F_{pz}(t)\delta(x - h_{pz}) = m(x)\frac{\partial^2 u(x,t)}{\partial t^2}, \qquad 0 < x < h_{pz}.$$ (3. 38)

Eq. (3.38) is non-homogenous equation. The boundary conditions are as in Eq. (3.39) and Eq. (3.40) which are both homogenous.

$$u(0,t) = 0,$$

(3. 39)

$$Y_{33}A(x)\frac{\partial u(x,t)}{\partial x}\Big|_{x=h_{pz}} = 0.$$

(3. 40)

To obtain the response of this system, the eigenvalue problem defined by the differential equation, Eq. (3.41), and the boundary conditions, Eq. (3.42) and (3.43) should be solved.

$$\frac{d}{dx}\left[Y_{33}A(x)\frac{dU(x)}{dx}\right] = w^2 m(x)U(x), \qquad 0 < x < h_{pz}, \qquad (3.41)$$

$$U(0) = 0, \qquad (3.42)$$

$$Y_{33}A(x)\frac{dU(x)}{dx}\Big|_{x=h_{pz}} = 0. \qquad (3.43)$$

The solution of this equations is concluded with eigenfunctions, $U_r(x)$ and eigenvalues, w_r^2 where $r = 1,2,...$. The eigenfunctions are orthogonal and assumed to have been normalized to satisfy the orthonormality conditions as in

$$\int_0^{h_{pz}} m(x)U_r(x)U_s(x)dx = \delta_{rs}, \qquad r,s = 1,2,..., \qquad (3.44)$$

$$-\int_0^{h_{pz}} U_s(x)\frac{d}{dx}\left[Y_{33}A(x)\frac{dU_r(x)}{dx}\right]dx = w_r^2\delta_{rs}, \qquad r,s = 1,2,..., \qquad (3.45)$$

δ_{rs} is defined as

$$\begin{aligned}\delta_{rs} &= 0, \quad if \ \ r \neq s, \\ \delta_{rs} &= 1, \quad if \ \ r = s.\end{aligned} \qquad (3.46)$$

A solution is assumed in the form of

$$u(x,t) = \sum_{r=1}^{\infty} U_r(x)\eta_r(t).$$ (3. 47)

Inserting Eq. (3.47) in to (3.38), multiplying by $U_s(x)$, integrating over the height of the piezoelectric material, and considering orthonormality relations which are as in Eq. (3.44) and (3.45), the modal equations are obtained as

$$\ddot{\eta}_r(t) + w_r^2 \eta_r(t) = N_r(t), \qquad\qquad r = 1,2,\dots\,,$$ (3. 48)

where modal forces, $N_r(t)$ are calculated as

$$N_r(t) = \int_0^L U_r(x)F(t)\delta(x-L)dx = U_r(L)F(t), \qquad r = 1,2,\dots\,.$$ (3. 49)

Then, the solution of Eq. (3.48) can be calculated as

$$\eta_r(t) = \frac{1}{w_r}\int_0^t N_r(t-\tau)\sin(w_r\tau)d\tau,$$

$$= \frac{U_r(L)}{w_r}\int_0^t F(t-\tau)\sin(w_r\tau)d\tau, \qquad r = 1,2,\dots\,.$$ (3. 50)

For the piezoelectric device having $Y_{33}A(x) = Y_{33}A =$ constant, $m(x) = m =$ constant, fixed at $x = 0$ and forced by a boundary force at $x = h_{pz}$, the solution of the eigenvalue problem consists of the orthonormal modes

$$U_r(x) = \sqrt{\frac{2}{mh_{pz}}}\sin(\frac{(2r-1)\pi x}{2h_{pz}}), \qquad r = 1,2,\dots\,,$$ (3. 51)

and the natural frequencies

$$w_r = \frac{(2r-1)\pi}{2}\sqrt{\frac{Y_{33}A}{mh_{pz}^2}}, \qquad\qquad r = 1,2,\dots \qquad\qquad (3.52)$$

By calculating the response of the system, the strain, S_3 can be calculated depending on both the location and time as

$$S_3(x,t) = \frac{\partial u(x,t)}{\partial x}. \qquad\qquad (3.53)$$

The stress, T_3 and corresponding electrical field, E_{33} is calculated by

$$T_3(x,t) = S_3(x,t)Y_{33}, \qquad\qquad (3.54)$$

$$E_{33}(x,t) = T_{33}(x,t)g_{33}. \qquad\qquad (3.55)$$

By this approach, the dynamic characteristics of the piezoelectric element are taken into account for all frequency range. In addition, if a multilayer piezoelectric element as in Figure 3.9 whose properties will be discussed in the following sections is analyzed; the different levels of stress and concluded electrical field for different layers can be taken into account.
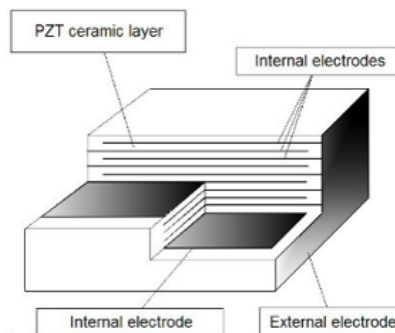
Figure 3.9 Multilayer Piezoelectric Material Cutaway Drawing [4]

3.1.2   Electrical Modelling of High Power Piezoelectric Systems

The electrical characteristics of piezoelectric elements are dependent on the conditions of the usage. When the loading conditions are static or quasi-static which means well below resonance of piezoelectric elements, the piezoelectric effect is obtained by piezoelectric d and g constants. Under dynamic conditions where the loading conditions are near to resonance frequency of piezoelectric elements, the piezoelectric effect is characterized by an equivalent electrical circuit, which exhibits the conditions of parallel and series resonance frequencies [32].

3.1.2.1   Static and Quasi-Static Operation

In high power applications in munitions, the excitation characteristic is as in Figure 3.4 depending on the pressure characteristics inside the cartridge characteristics. For instance, the pressure characteristic of a 35 mm gun is as in Figure 3.10 which results in acceleration form in a similar form with corresponding amplitudes [33].
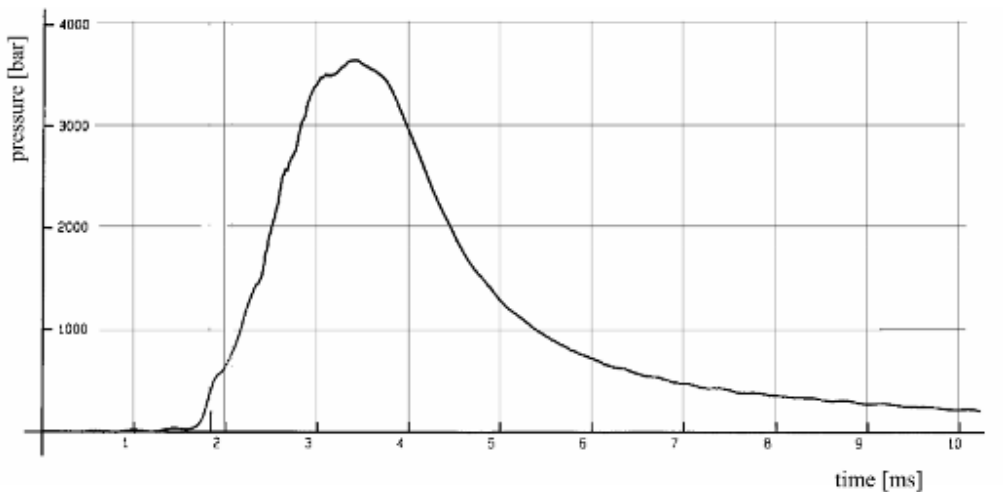
Figure 3.10 Pressure vs. Time Curve Measured inside the 35 mm Cartridge Case [33]

43

As it can be seen from both Figure 3.4 and Figure 3.10, the duration of the loading is about 10 milliseconds. Designing a piezoelectric power generator working in resonance condition in this loading condition is not possible because of the mechanical strength limitations since it should have a resonance frequency of about 50-100 Hz. To have a piezoelectric device having the resonance frequency in this range, it should be in the cantilevered condition as in Figure 3.11. In this cantilevered condition, piezoelectric device works in "31" mode where the mechanical stress is in the 1st direction and the electrodes are vertical to 3rd direction in Figure 2.1.
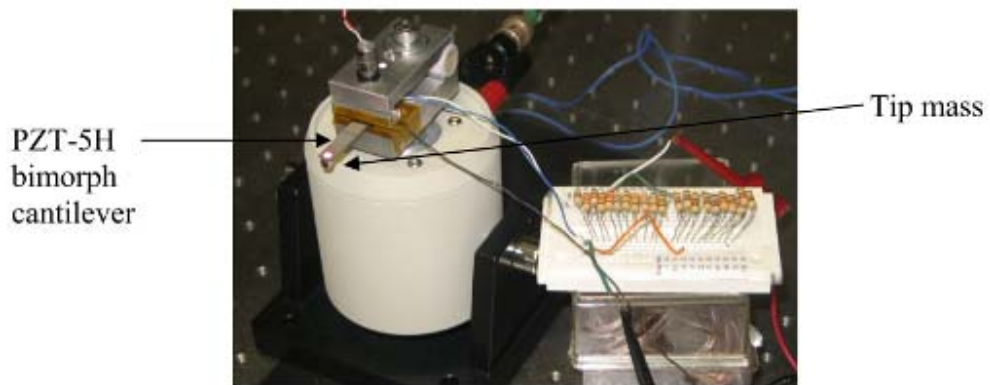
Figure 3.11 PZT-5H bimorph cantilever with a tip mass [8]

To get a piezoelectric device having the mechanical strength to work in high acceleration environment, piezoelectric devices working in compression mode like in Figure 3.12 with a compression mass or resonator system should be used. In this condition, piezoelectric device works in "33" mode where the mechanical stress is in the 3rd direction and the electrodes are vertical to 3rd direction. Since in this condition the piezoelectric devices have the natural frequency in kHz range, they are treated as

working in quasi-static condition. In static or quasi-static conditions, electrical circuit of piezoelectric devices is as as in Figure 3.13 [4].
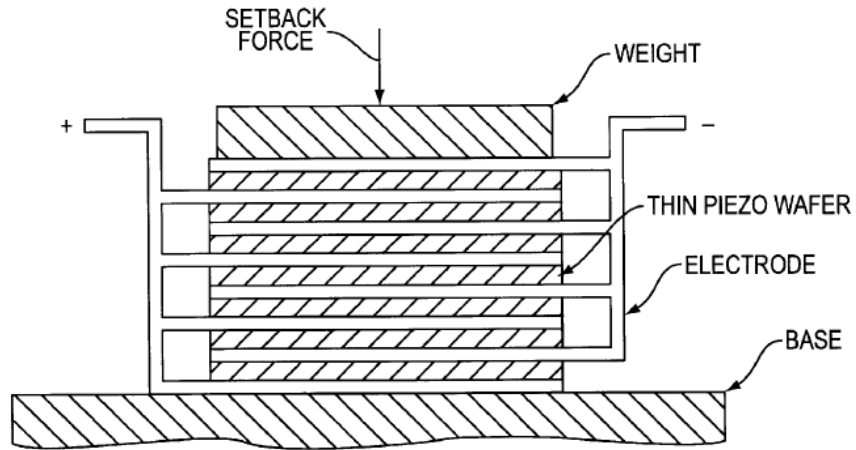
Figure 3.12 33 mode Piezoelectric Stack [34]
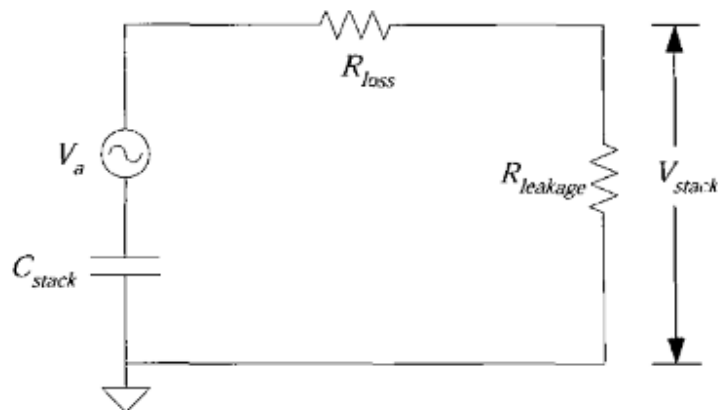
Figure 3.13 Equivalent Circuit of Piezoelectric Power Generator in Static and Quasi-Static Conditions [4]

When the piezoelectric effects are not activated, piezoelectric ceramics are basically capacitors. Therefore, the capacitance of the piezoelectric element can be calculated by

$$C_{stk} = \frac{\varepsilon_{33}A}{h_{pz}},$$ (3. 56)

where ε_{33} is the permittivity of the material in usage mode, A is the area of the electrode surfaces and h_{pz} is the thickness of the piezoelectric material.

The permittivity of the material, ε_{33} is related to permittivity of free space, ε_0 and the relative permittivity of the material, $\varepsilon_{3,r}$ as

$$\varepsilon_{33} = \varepsilon_0 \varepsilon_{3,r}.$$ (3. 57)

The permittivity of free space, ε_0 is $8.85x10^{-12}[Farads / meters]$. In a piezoelectric material datasheet, the relative permittivity of the material, $\varepsilon_{3,r}$ is defined for constant stress and constant strain condition as $\varepsilon_{3,r}^T$ or $\varepsilon_{3,r}^\sigma$ and $\varepsilon_{3,r}^S$ relatively. In static or quasi-static condition the permittivity in constant stress condition, $\varepsilon_{3,r}^T$ should be used [32].

V_a is the voltage source which is added to the electrical model to simulate the energy produced by piezoelectric material because of its piezoelectric characteristics. V_a can be calculated by dividing the produced charge, Q, by the capacitance of the piezoelectric stack.

$$V_a = \frac{Q}{C_{stk}}.$$ (3. 58)

The produced charge, Q is calculated by multiplying the compression force applied on the piezoelectric element, F_{pz} with the piezoelectric constant, d_{33} as

$$Q = d_{33} F_{pz} . \qquad (3.59)$$

Mechanical stress created in piezoelectric energy harvester can also be used to find the electrical parameters as mentioned before. By the mechanical stress, T_{pz} created electrical field, E is found by multiplying it with the piezoelectric voltage constant, g_{33} as

$$E = g_{33} T_{pz} , \qquad (3.60)$$

where g_{33} is the piezoelectric voltage constant. Electrical displacement value, D can be calculated by

$$D = E \varepsilon_0 \varepsilon_{3,r}^{T} . \qquad (3.61)$$

Then the produced charge can be found by

$$Q = DA_{pz} . \qquad (3.62)$$

Piezoelectric constants d_{33} and g_{33} are related with

$$d_{33} = g_{33} \varepsilon_0 \varepsilon_{3,r}^{T} . \qquad (3.63)$$

As an alternative method to calculate the produced voltage, V_a the energy relationships can also be used. Mechanical energy stored in the piezoelectric system, E_{mech} can be calculated by

$$E_{mech} = F_{pz} x_{pz},$$

(3.64)

where x_{pz} is found by Eq. (3.23).

The harvested electrical energy, E_{elec} can be calculated by

$$W_{elec} = \frac{1}{2} \frac{Q^2}{C_{stk}} = \frac{1}{2} C_{stk} V_a^2.$$

(3.65)

The mechanical and electrical energy has the relationship related with electromechanical coupling coefficient, k_{33} as

$$k_{33}^2 = \frac{E_{elec}}{E_{mech}}.$$

(3.66)

By Eqs. (3.64), (3.65) and (3.66), V_a can be calculated as

$$V_a = k_{33} \sqrt{\frac{2 F_{pz} x_{pz}}{C_{stk}}}.$$

(3.67)

The loss resistance, R_{loss} in the electrical circuit in Figure 3.13 is replaced in series to represent the losses from the current travelling across the surfaces of the material to the electrical leads and it is on the order of tens of ohms. It is calculated by the loss tangent of the material, $\tan(\delta)$ operating frequency, w and the capacitance of the piezoelectric material as

$$R_{loss} = \frac{\tan(\delta)}{w C_{stk}}.$$

(3.68)

The leakage resistance, $R_{leakage}$ is replaced in parallel to represent the losses as current travels through the material. It is on the order of mega ohms. It is experimentally determined which is described in experimental setup chapter.

After finding all of the electrical parameters of the circuit in Figure 3.13, this circuit is created in ORCAD PSPICE® to find the terminal voltage of the piezoelectric element. A sample electrical circuit of a piezoelectric element created in this program is as in Figure 3.14.
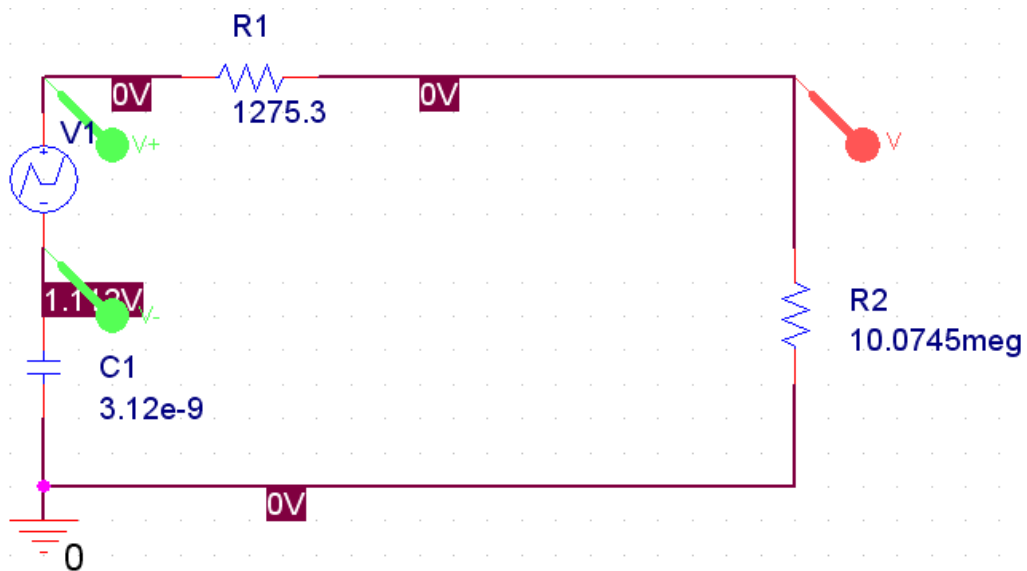
Figure 3.14 Sample ORCAD PSPICE® Piezoelectric Material Model

Impedance matching is an important concept to get the optimal power output. The power produced is calculated by

$$P = \frac{V_{rms}^2}{R},$$

(3. 69)

where R is the loading resistance connected to piezoelectric device and V_{rms} is the voltage measured in rms values. For example, for a harmonic forcing

$$V_{rms} = \frac{V_{pp}^2}{2\sqrt{2}}$$

(3. 70)

where V_{pp} is the peak voltage value which is measured.

The matching loading impedance is found by

$$R = \frac{1}{wC_{stk}} \, .$$

(3. 71)

When 33 mode piezoelectric materials in bulk form are used in high power applications, they produce the voltage in kilovolts ranges. This electrical energy cannot be used in electrical components without an electrical converter which is used to lower the voltage. Because of the space limitations, it is not practical to use such converters. In addition, energy lost is a big concern in this case. Instead of this, multilayer-piezoelectric stacks are used to lower the voltage and increase the charge amount. In Figure 3.15, multilayer CMAR 03 material contains 25 layers of piezoelectric elements in 2 mm thickness at total which are connected in parallel electrically and in series mechanically. Comparison of electrical properties of single layer and multilayer piezoelectric devices are as in Table 3.1.

Multilayer CMAR 03
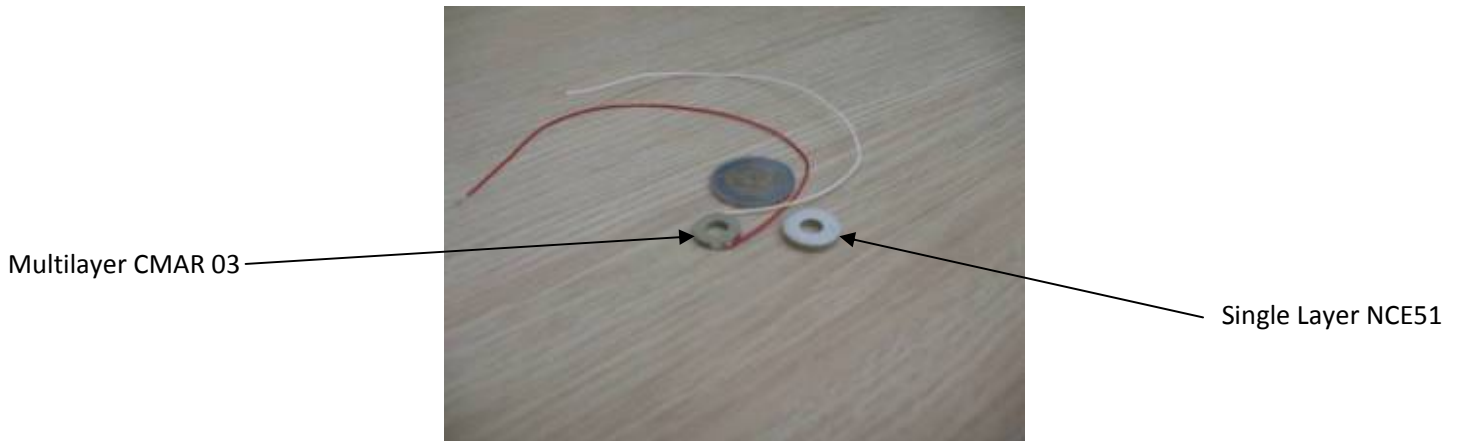
Single Layer NCE51

Figure 3.15 Multilayer CMAR03 and Single Layer NCE 51 Material

Table 3.1 Comparison of Electrical Characteristics of Single Layer and Multilayer
Piezoelectric Materials

Property	Capacitance	Charge	Open Circuit Voltage	Electrical Energy Harvested
Single Layer (Bulk) Piezoelectric	$C_{tot} = \dfrac{\varepsilon A}{h_{pz}}$	$Q_{tot} = Q$	$V_{tot} = V$	$E_{elec} = \dfrac{1}{2}\dfrac{Q_{tot}^2}{C_{tot}}$ $= \dfrac{1}{2}\dfrac{Q^2 \varepsilon A}{h_{pz}}$
Multilayer Piezoelectric (n layers)	$C_{tot} = n\dfrac{\varepsilon A}{h_{pz}/n}$ $= n^2\dfrac{\varepsilon A}{t}$	$Q_{tot} = nQ$	$V_{tot} = \dfrac{V}{n}$	$E_{elec} = \dfrac{1}{2}\dfrac{Q_{tot}^2}{C_{tot}}$ $= \dfrac{1}{2}\dfrac{Q^2 \varepsilon A}{h_{pz}}$

3.1.2.2   Dynamic Operation

In this thesis, scope of the study is high power applications in munitions and the piezoelectric elements work on quasi-static conditions because of the reasons which were defined above. However, in this section, the basics of electrical characteristics of piezoelectric devices in dynamic operation are displayed to be aware of the differences from static or quasi-static cases and having the knowledge for these applications.

In dynamic conditions, the behaviour of piezoelectric materials can be characterized by a complex equivalent circuit which exhibits the conditions of parallel and series resonance frequencies which is called as Mason Model and schematized in Figure 3.16.
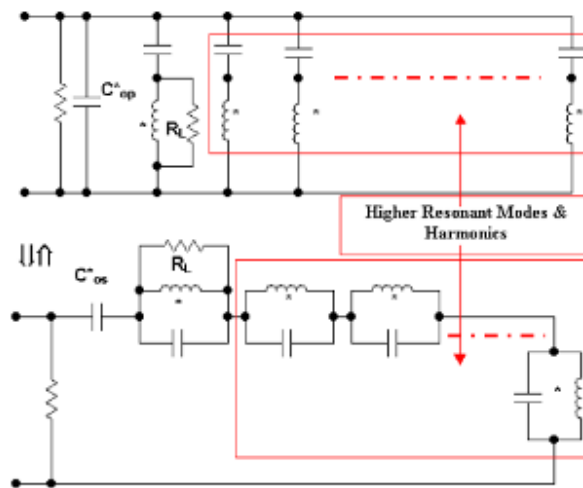
Figure 3.16 Mason Model with Higher Resonant Modes [5]

For a single degree of freedom system with one resonance frequency interested, impedance characteristics of the piezoelectric element as in Figure 3.17 looks like of a serial resonance circuit with some parallel capacitor as in Figure 3.18. Actually, the electro-mechanical equivalent circuit in Figure 3.18 is formed by composing the capacitance of the piezoelectric material and the mechanical parameters by electromechanical coupling factor, k. The electrical model in Figure 3.18 can also be used for static or quasi-static cases. However, it is more complicated than the electrical circuit in Figure 3.13.
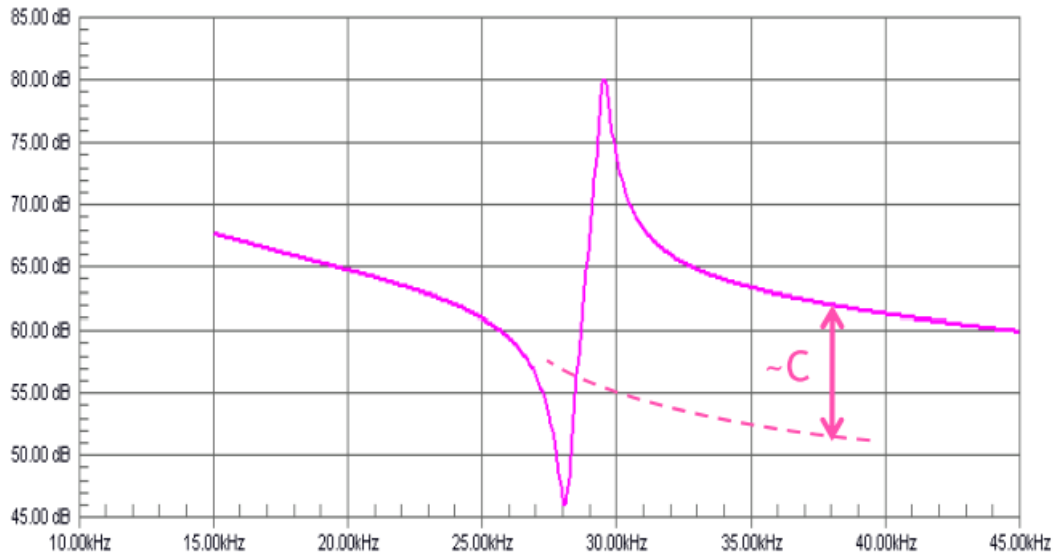
Figure 3.17 Impedance Characteristics of a Piezoelectric Device [5]
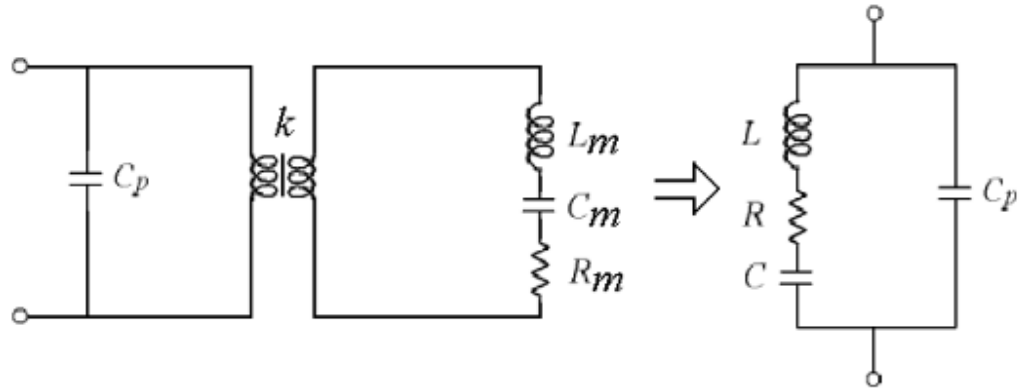
Figure 3.18 Electro-mechanical Equivalent Circuit of a Piezoelectric Device [5]

Theoretically mechanical inductance, L_m resistance, R_m and capacitance, C_m can be calculated by

$$L_m = \frac{\rho_s h_p^2}{2 A_{pz} e^2},$$
(3. 72)

$$R_m = \frac{v h_p}{A_{pz} e^2},$$
(3. 73)

$$C_m = \frac{A_{pz} e^2}{c h_p},$$
(3. 74)

respectively, where ρ_s is surface mass density, e is piezoelectric stress constant, c is elastic constant and v is viscosity.

The capacitance of the piezoelectric material, C_p is again calculated by Eq. (3.56). For the dynamic conditions well above all resonance frequencies, the relative

permittivity, $\varepsilon_{3,r}$ should be taken for constant strain condition which is symbolized as $\varepsilon_{3,r}^S$. Between the resonance frequencies, the permittivity is the product of static permittivity, $\varepsilon_{3,r}^T$ and a loss term based on the electromechanical coupling factor of the resonance mode. For excitation frequencies above the first resonance, the relative permittivity becomes

$$\varepsilon_{3,r} = \varepsilon_{3,r}^T (1 - k_1^2). \tag{3.75}$$

For excitation frequencies above the second resonance frequency, the relative permittivity becomes

$$\varepsilon_{3,r} = \varepsilon_{3,r}^T (1 - k_1^2)(1 - k_2^2). \tag{3.76}$$

If the energy harvester is in the shape of a thin disc, k_1 is k_p for the radial mode, k_2 is k_t for the thickness mode. If it is in the shape of rod, k_1 is k_{33} for the length mode and k_2 is k_p for the radial mode. [32]

The electrical parameters can also be found by impedance measurement results. The frequency of minimum impedance is resonance frequency, f_r and the frequency of maximum impedance is anti-resonance frequency, f_a. They are defined as

$$f_r = \frac{1}{2\pi\sqrt{LC}}, \tag{3.77}$$

$$f_a = \frac{1}{2\pi\sqrt{L\dfrac{CC_p}{C+C_p}}}. \tag{3.78}$$

$C + C_p$ can be measured and all parameters and L, C and C_p can be identified.

By applying the resonance and anti-resonance frequencies, the electromechanical coupling coefficient can also be determined. For example, for the piezoelectric energy harvesters in rod shape, it can be calculated as in

$$k_{33}^2 = \frac{\pi}{2} \frac{f_a}{f_r} \tan(\frac{\pi}{2} \frac{(f_a - f_r)}{f_a}) .$$

(3. 79)

3.2 Finite Element Modelling of High Power Piezoelectric Systems

Finite element modelling (FEM) is also a method to find the solutions of the systems containing the piezoelectric materials by numerical techniques. Some of general purpose commercial finite element analysis (FEA) program packages like ANSYS have the capability of modelling piezoelectric systems. In this thesis, ATILA$^®$ which is a FEA software package for the analysis of 2D & 3D structures based on smart materials like piezoelectric, magnetostrictive etc. with Gid Interface is used. In this section, the theory used in this program to analyze the piezoelectric energy harvesters is defined [35].

ATILA$^®$ has the solution capabilities in the domains as described in Figure 3.19. In the general formulation of modelling elastic, piezoelectric or magnetostrictive structures, the mesh of the structure under study and part of the space surrounding it are necessary for modelling magnetostrictive elements but not for piezoelectric materials since common piezoelectric materials have a high relative permittivity. The general equations are those of elasticity in the structure, Poisson's equation in the piezoelectric or electrostrictive material, Maxwell's equations for the magnetostatic case in the magnetic domain and Helmholtz's equation in the fluid. The electromechanical coupling exists in piezoelectric, electrostrictive or magnetostrictive domains.
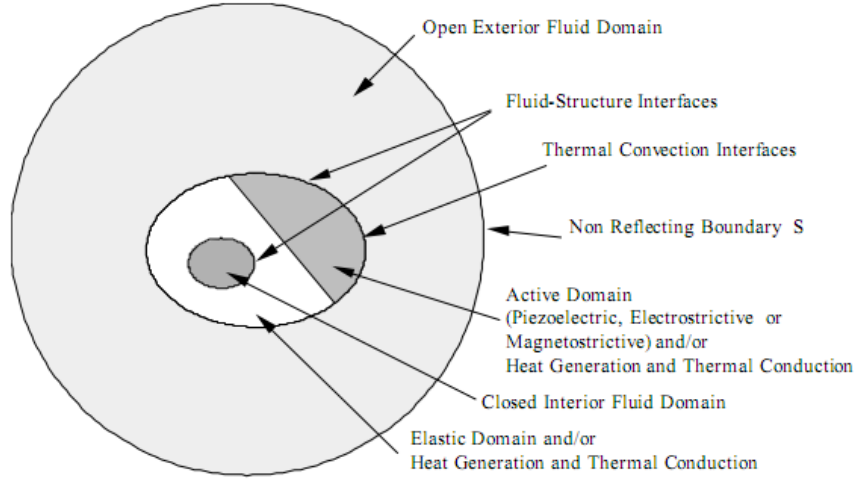
Figure 3.19 ATILA$^{®}$ General Solution Domains and Their Interrelations [35]

The concluded complete set of equations is written in the form of

$$
\begin{bmatrix}
[K_{uu} - w^2[M]] & [K_{u\phi}] & [K_{u\phi}] & [K_{uI}] & -[L] \\
[K_{u\phi}]^T & [K_{\phi\phi}] & [0] & [0] & [0] \\
[K_{u\phi}]^T & [0] & [K_{\phi\phi}] & [K_{\phi I}] & [0] \\
[K_{uI}]^T & [0] & [K_{\phi I}]^T & [K_{II}] & [0] \\
-\rho_f{}^2 c_f{}^2 w^2 [L]^T & [0] & [0] & [0] & [H] - w^2[M_1]
\end{bmatrix}
\begin{bmatrix}
\underline{U} \\
\underline{\Phi} \\
\underline{\phi} \\
\underline{I} \\
\underline{P}
\end{bmatrix}
=
\begin{bmatrix}
\underline{F} \\
-\underline{q} \\
-\underline{f} \\
-\underline{f_b} \\
\rho_f{}^2 c_f{}^2 \underline{\Psi}
\end{bmatrix}
\quad (3.80)
$$

where $\underline{U}$ is vector of nodal values of the components of the displacement field, $\underline{\Phi}$ is vector of the nodal values of the electric potential, $\underline{\phi}$ is vector of the nodal values of reduced magnetic potential, $\underline{I}$ is vector of the prescribed values of the excitation currents (one component for each coil), $\underline{P}$ is vector of the nodal values of the pressure field, $\underline{F}$ is the vector of the nodal values of the applied forces, $\underline{q}$ is the

vector of nodal values of the electrical charges, $\underline{f}$ is the vector of the nodal values of the reduced magnetic field flux across the magnetic domain boundary, $\underline{f_b}$ is the vector of the nodal values of the reduced magnetic field flux seen by the coils (one component for each coil), $\underline{\Psi}$ is the vector of the nodal values of the integrated normal derivative of the pressure on the surface boundary S, $[K_{uu}]$ is stiffness matrix, $[K_{u\Phi}]$ is piezoelectric matrix, $\lfloor K_{u\phi} \rfloor$ is piezomagnetic coupling matrix, $[K_{uI}]$ is source-structure coupling matrix, $[K_{\Phi\Phi}]$ is dielectric matrix, $\lfloor K_{\phi I} \rfloor$ is source-magnetization coupling matrix, $\lfloor K_{\phi\phi} \rfloor$ is magnetic (pseudo-) stiffness matrix, $[K_{II}]$ is inductance matrix in vacuum, $[M]$ is consistent mass matrix, $[H]$ is fluid (pseudo-) stiffness matrix, $[M_1]$ is consistent (pseudo-) fluid mass matrix, $[L]$ is coupling matrix at the fluid structure interface (connectivity matrix), w is angular frequency, ρ_f is fluid density, c_f is fluid sound speed.

ATILA$^{®}$ can solve static, modal, harmonic and transient analysis by Eq. (3.80).
For the static analysis of a piezoelectric structure, Eq. (3.80) is reduced to

$$
\begin{bmatrix} [K_{uu}] & [K_{u\Phi}] \\ [K_{u\Phi}]^T & [K_{\Phi\Phi}] \end{bmatrix} \begin{bmatrix} \underline{U} \\ \underline{\Phi} \end{bmatrix} = \begin{bmatrix} \underline{F} \\ -\underline{q} \end{bmatrix}
$$

(3. 81)

If the piezoelectric system subjected to a force, $\underline{F}$ (direct piezoelectric effect), or the prescribed electrical potentials on given nodes (converse piezoelectric effect), the ATILA$^{®}$ code computes the displacement field, $\underline{U}$ and the electric potential, $\underline{\Phi}$ over the entire structure. Internal losses are not taken into account in this analysis because it is not possible.

In the modal analysis of piezoelectric structure, the system of equations is reduced to

$$\begin{bmatrix} [K_{uu}]-w^2[M] & [K_{u\Phi}] \\ [K_{u\Phi}]^T & [K_{\Phi\Phi}] \end{bmatrix}\begin{bmatrix} \underline{U} \\ \underline{\Phi} \end{bmatrix} = \begin{bmatrix} 0 \\ -\underline{q} \end{bmatrix}$$

(3. 82)

ATILA$^®$ code computes the eigenvalues and the eigenvectors of the linear system for different boundary conditions. The computation uses real values with no internal losses. The eigenvectors are mass normalized as

$$\underline{U}^T[M]\underline{U} = [I]$$

(3. 83)

In harmonic analysis, known harmonic loads and/or excitations are applied on the piezoelectric structure and the system of equations becomes

$$\begin{bmatrix} [K_{uu}]-w^2[M] & [K_{u\Phi}] \\ [K_{u\Phi}]^T & [K_{\Phi\Phi}] \end{bmatrix}\begin{bmatrix} \underline{U} \\ \underline{\Phi} \end{bmatrix} = \begin{bmatrix} \underline{F} \\ -\underline{q} \end{bmatrix}$$

(3. 84)

For the piezoelectric element, ATILA$^®$ code computes the displacement field, $\underline{U}$ the electric potential, $\underline{\Phi}$ and the electrical impedance of the piezoelectric structure from the electric charge, $\underline{q}$. Gaussian algorithms are used to solve the problem in single or double precision. The internal losses in the materials can be taken into account.

In transient analysis, known loads such as forces $\underline{F}$ and electric charges $\underline{q}$ or known displacement $\underline{U}$ and electric potentials $\underline{\Phi}$ can be applied on the piezoelectric structure. The system of equation becomes

$$\begin{bmatrix} [M] & [0] \\ [0] & [0] \end{bmatrix}\begin{bmatrix} \ddot{\underline{U}} \\ \ddot{\underline{\Phi}} \end{bmatrix} + \frac{1}{w_0}\begin{bmatrix} [\ddot{K}_{uu}] & [\ddot{K}_{u\Phi}] \\ [\ddot{K}_{u\Phi}]^T & [\ddot{K}_{\Phi\Phi}] \end{bmatrix}\begin{bmatrix} \dot{\underline{U}} \\ \dot{\underline{\Phi}} \end{bmatrix} + \begin{bmatrix} [\dot{K}_{uu}] & [\dot{K}_{u\Phi}] \\ [\dot{K}_{u\Phi}]^T & [\dot{K}_{\Phi\Phi}] \end{bmatrix}\begin{bmatrix} \underline{U} \\ \underline{\Phi} \end{bmatrix} = \begin{bmatrix} \underline{F} \\ -\underline{q} \end{bmatrix}$$ (3. 85)

where " $\dot{}$ " and " $\ddot{}$ " symbolize first and second time derivatives, respectively. w_0 is the pulsation at which the material losses are defined. Eq. (3.85) is solved by an iterative method, taking a constant time step Δt. One of three methods can be used: the Central Difference Method, the Newmark Method and the Wilson-θ Method. The ATILA$^®$ code computes the displacement field, $\underline{U}$, and the electric potential, $\underline{\Phi}$, for the requested time steps.

ATILA$^®$ software has 2-D and 3-D piezoelectric elements for these piezoelectric analysis types. For 3-D analysis with or without losses, HEXA20P, PRIS15P, PYRA13P and TETR10P piezoelectric elements with three translational, U_x, U_y, U_z, and one electric potential, Φ, active degrees of freedom can be used. Topology of 3-D piezoelectric elements is as in Figure 3.20.
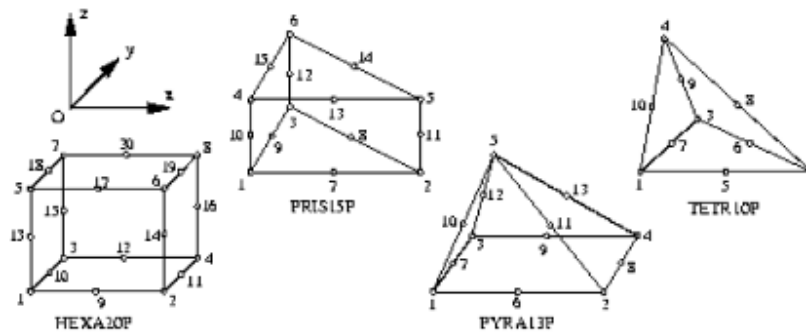
Figure 3.20 Topology of ATILA$^®$ Software 3-D Piezoelectric Elements

For 2-D analysis with or without losses, QUAD08P and TRIA06P piezoelectric elements with two translational, U_x, U_y and one electric potential, Φ, active degrees of freedom can be used. Topology of 2-D piezoelectric elements is as in Figure 3.21.

For the material definitions the elastic, piezoelectric, dielectric tensors and the density should be entered.
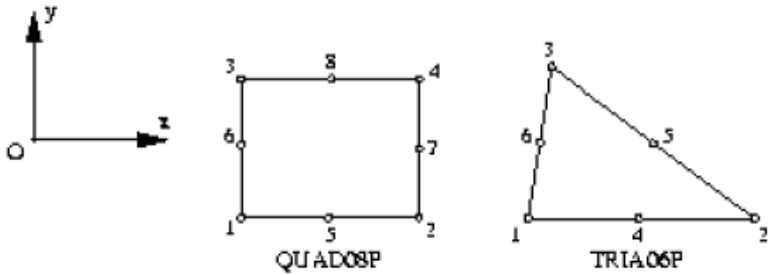
Figure 3.21 Topology of ATILA® Software 2-D Piezoelectric Elements

CHAPTER 4

EXPERIMENTAL ARRANGEMENT

Several experiments are arranged to measure the electrical parameters of piezoelectric materials or to verify the mathematical models.

In the first part of this chapter, the methods to measure the capacitance and leakage resistance of the piezoelectric materials are discussed.

In the latter part, the experimental setups to apply harmonic loading onto a bulk piezoelectric material for verification of the mathematical models in a simple way and to apply a mechanical shock for simulation of the gunfire environment with lower levels are described.

4.1. Electrical Parameters Measurement

4.1.1. Capacitance Measurement

Since there are always imperfections in a bulk piezoelectric material or multilayer stack, it is more confident to measure the capacitance of them. The capacitance can be directly measured by a multi-meter. Capacitance measurement are displayed in Appendix C.

4.1.2. Leakage Resistance Measurement

To measure the leakage resistance of a piezoelectric material by considering the electrical representation of piezoelectric materials in Figure 3.13, firstly it is considered to apply a voltage in piezoelectric material by a power supply as in Appendix C and recording the corresponding current.

Then, the leakage resistance could be calculated as

$$R_{leakage} = \frac{V}{I} \qquad (4.1)$$

However, most of the power supplies show the current in mili-ampers range at least. Since $R_{leakage}$ is expected to be in mega-ohms range the current is expected to be in micro-ampers range which is not possible to observe.

As a practical way, it is considered to create the electrical circuit in Figure 4.1. To describe, the piezoelectric element is connected a resistance having a value on the order of mega-ohms. Then, they are connected to a power supply and input voltage, V_{in} and output voltage, V_{out} is measured by a multi-meter as in Appendix C. By this measured voltage values and the known resistance value, R_1 leakage resistance, $R_{leakage}$ is calculated as

$$R_{leakage} = \frac{V_{out}}{V_{in} - V_{out}} R_1 \qquad (4.2)$$
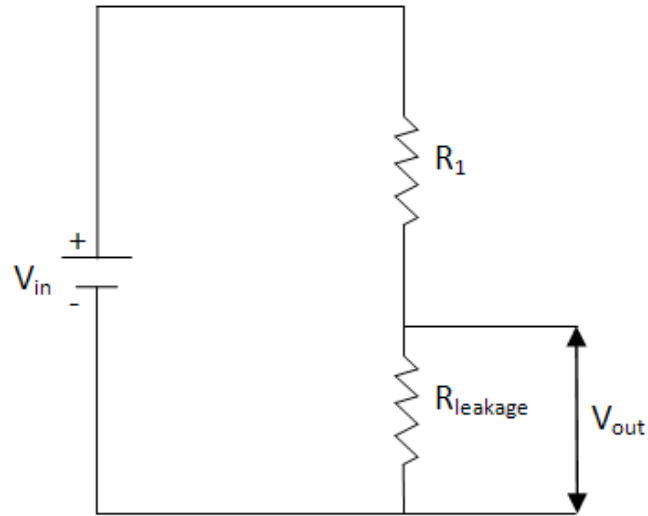
Figure 4.1 Leakage Resistance Measurement Experimental Setup Circuit Scheme

4.2. Mechanical Loading and Measurements

4.2.1. Harmonic Loadings

By harmonic loading conditions, the main aim was to have the basic capabilities to measure the piezoelectric characteristics in known loading conditions and compare the mathematical model results.

In these tests, single layer NCE 40 material whose material properties are illustrated in Appendix B with a ring shape is used. The outer diameter is 49.9 mm, the inner diameter is 15.1 mm and the height is 6 mm. To have the capability of measuring the voltage signal produced by the material, electrical cables are soldered. To insulate the piezoelectric material, electrode surfaces from the fixture and steel compression masses, an insulator material with 0.4 mm thickness is employed possessing the required geometrical properties. Piezoelectric material together with electrical isolators is illustrated in Appendix C.

64

To compress the piezoelectric material because of the acceleration, some steel compression masses with different heights and the required slots not to get the electrical current on them are produced as in Appendix C.

To connect the piezoelectric material together with insulator materials and compression masses to modal shaker, an aluminium apparatus with required helicoil inserts in both surfaces is produced as in Appendix C.

To measure the produced acceleration, PCB 356B21 type accelerometer with 500 g measuring capability having the sensitivity of 10 mV/g is glued on the top surface of steel compression masses as in Appendix C and its weight is also included in calculations.

All of these components are held together with M8 bolt connection as in Figure 4.2.

The structure in Figure 4.2 is connected to TMS Model 2100E11 modal shaker with the aid of threaded sections. LMS Test System is used to drive the modal shaker by interconnecting QSC amplifier and to collect the accelerometer and piezoelectric voltage data. The oscilloscope basically used to double-check the correctness of the measured signals. The whole experimental setup is as in Figure 4.3.

4.2.2. Mechanical Shock Loading

By mechanical shock loading conditions, the main aim is to simulate the gunfire acceleration environment with lower acceleration and different duration levels and by correcting the mathematical models in this environment having the capability of design a piezoelectric energy harvester for the specified environment.

To get the mechanical shock of ten thousands g's in laboratory conditions mainly pneumatic, free fall and air gun shock test systems are used.
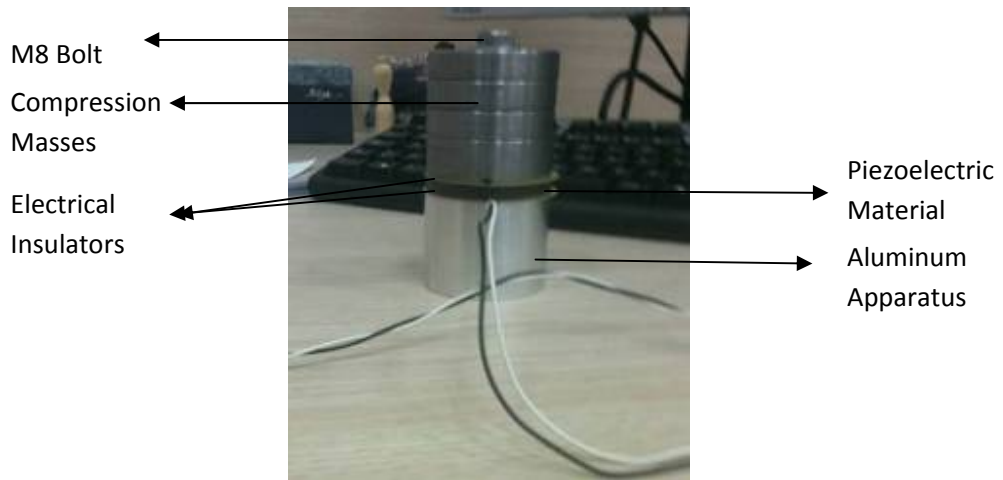
Figure 4.2 Piezoelectric Element Connected to Aluminium Apparatus
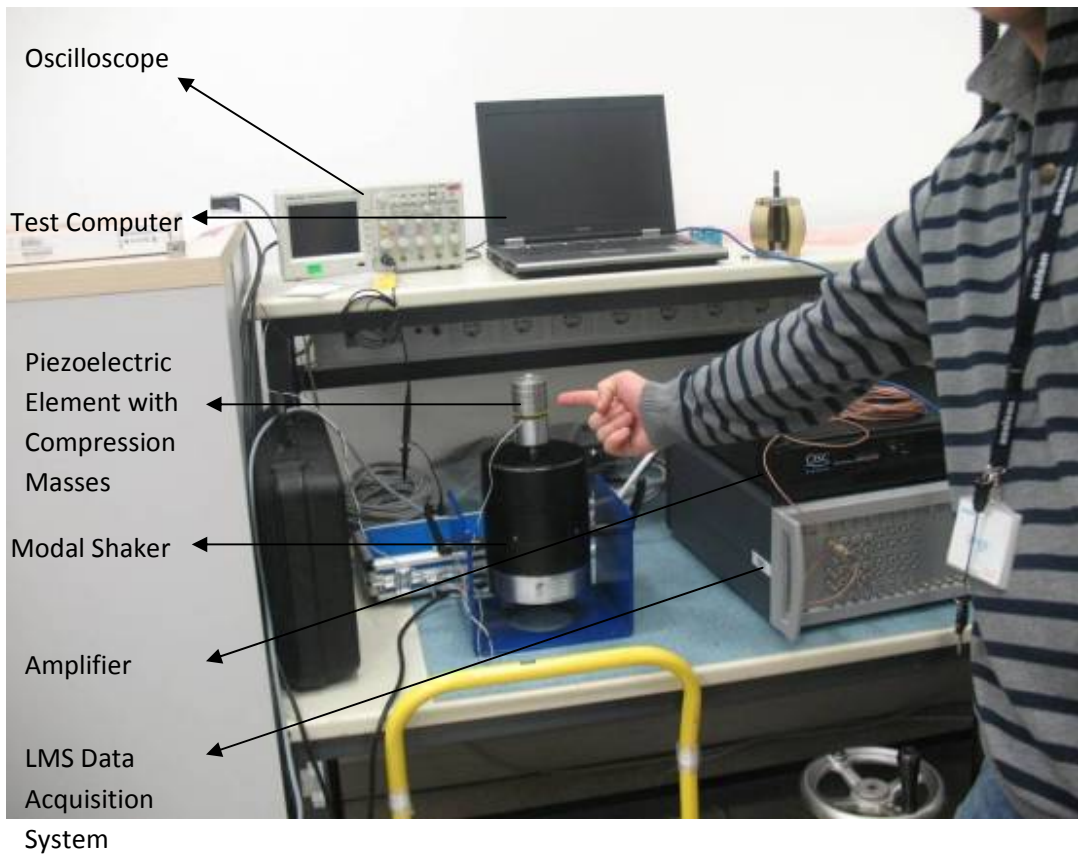
Figure 4.3 Harmonic Loading Test

4.2.2.1. Impact Hammer Test Setup

Free-fall shock test systems have the basic principle of producing acceleration by dropping a weight in test table in different speeds. Since any test system with high G capability is not available, a test system having the same logic with free fall shock test systems as in Figure 4.4 is designed. It is created by connecting a thick aluminium plate with mechanical shock isolators like Socitec HH15-20TM2 or MP8-230 model with different characteristics. Dytran 3200B2M model accelerometer with 50000 G acceleration measurement capability and 0.11 mV/g sensitivity is replaced as a control accelerometer. This structure is connected to a rigid table by mechanical clamps. Different types of impact hammers as in Appendix C are utilized to excite this system.

The acceleration levels up to 15000 G's with short durations like 0.04 ms is obtained by this test setup. The acceleration duration level is controlled by mechanical isolators with different stiffness and damping specifications. A sample shock measurement acceleration data with very high impact velocity is as in Figure 4.5.

Piezoelectric material, CMAR03 by Noliac Company whose properties are as in Appendix B, electrical isolator plates and compression masses are connected to an aluminium plate by means of a bolt as in Figure 4.6.

Some of multilayer piezoelectric ceramics are broken while tightening with bolt because they are very brittle and very sensitive to tensile stresses. Any tilting moment because of surface roughness or torsion and/or sliding of compression mass on piezoelectric element can cause such problems. Loctite Silver Anti-Seize in Appendix C is used to fill the porous metal surfaces and to prevent from sliding. It is a material which is used together with some kinds of piezoelectric material based force transducers for the same reasons.
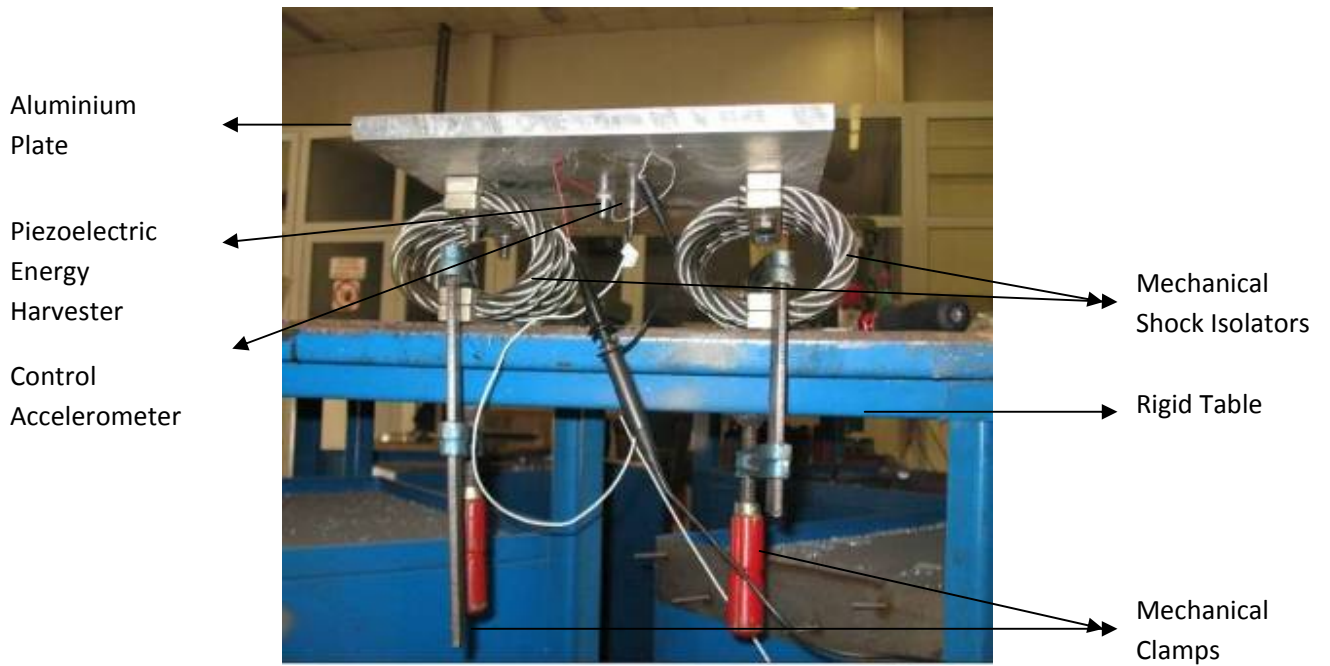
Figure 4.4 High G Shock Test System
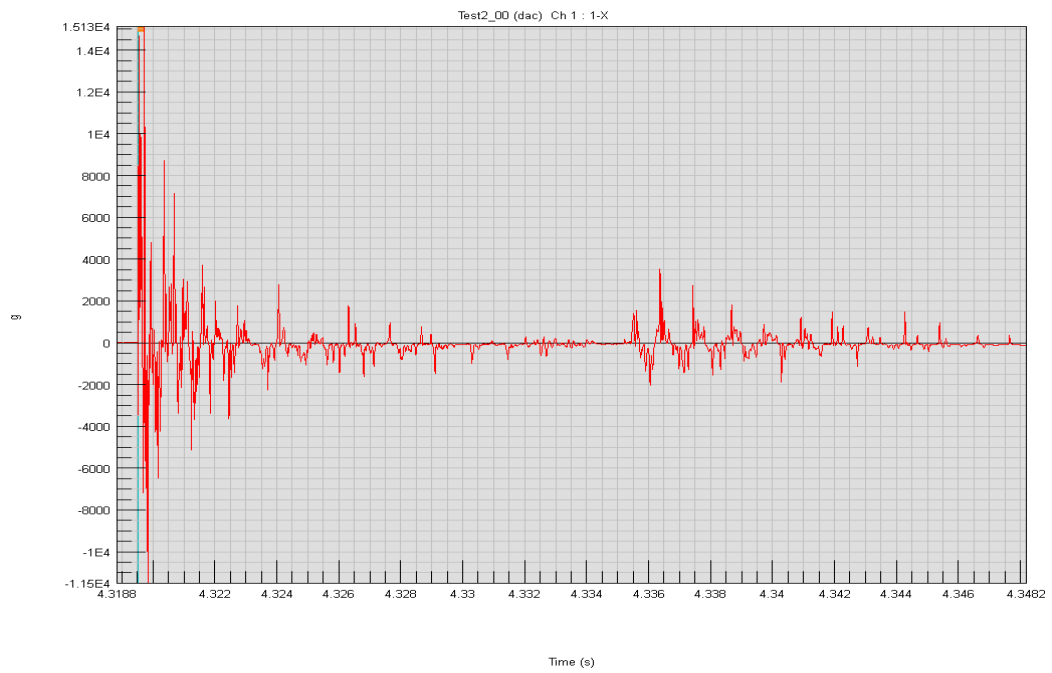
Figure 4.5 Sample Acceleration Data Measured in Impact Hammer Test Setup
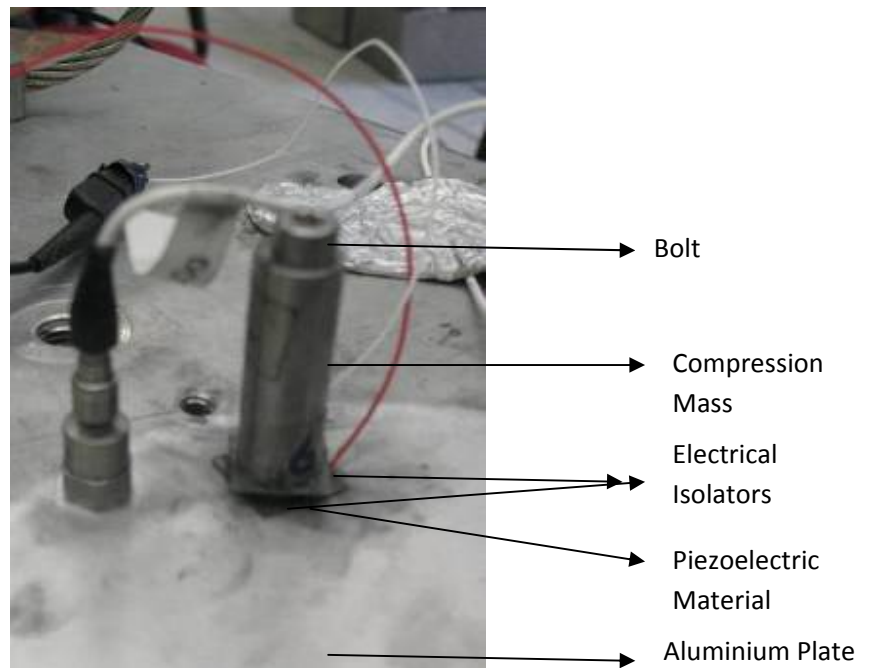
Figure 4.6 Piezoelectric Material and Compression Mass Connection

To get the displacement data as an additional control sensor, Micro-Epsilon laser displacement sensor as in Appendix C is used. However, since the excitation created in high frequency content which results in very small displacement values, the laser displacement results are not used.

Io-tech data acquisition system is used to collect laser displacement, accelerometer and piezoelectric material voltage data. It can collect data up to 256 kHz sampling rate which is very important in mechanical shock data collection according to channel numbers. The whole experimental setup is as in

Figure **4.7**.

In this test setup, the produced acceleration has lower durations than gunfire acceleration environment. This acceleration excites a large frequency band and also the resonance of piezoelectric energy harvester system. Exciting the resonance of

69

piezoelectric material can result in "zero-shift" phenomenon [38] . In addition, since the shock plate vibrates in positive and negative directions, piezoelectric material can withstand not only compression force but also tension forces which are out of concern in gunfire applications especially if the acceleration is very high and the resulted tension force is higher than preload applied by the bolt. To get the shock forms having more similar content with gunfire environment, pressure gun setup is also used.
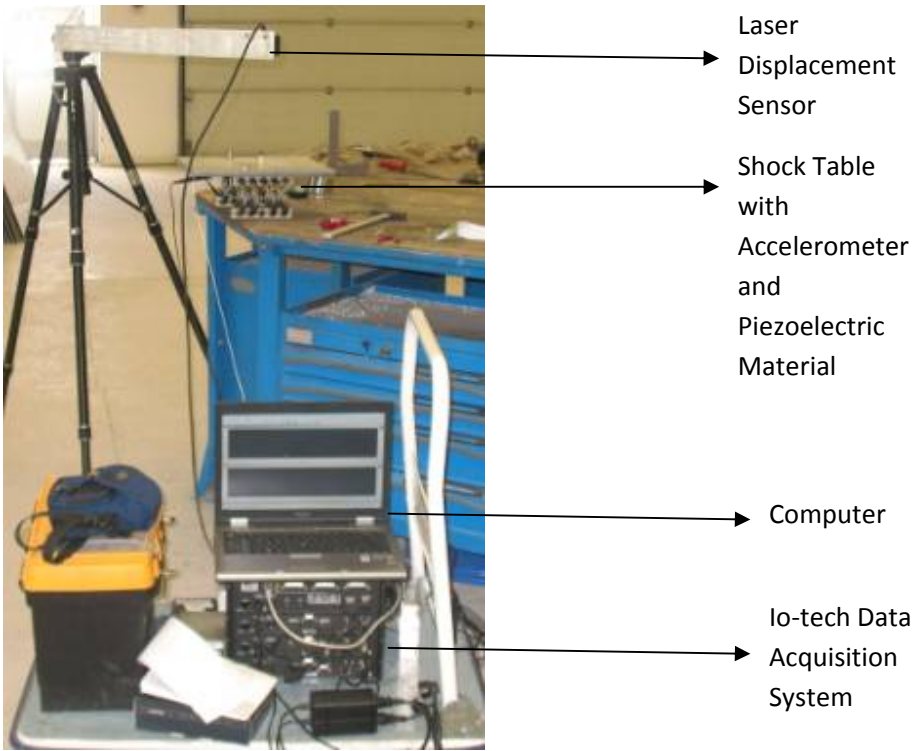
Figure 4.7 Impact Hammer Test Setup

4.2.2.2. Pressure Gun Test Setup

To have higher duration mechanical shocks, a pressure gun launcher as in Figure 4.8 is used. It uses a 230 bar nitrogen tube and can use it with 90-130 bar range to launch the test specimen.

To replace the piezoelectric energy harvester, accelerometer and wireless data acquisition system, the bottom flange of a cylindrical structure as in Figure 4.9 is used.

To get the test data, Slice Nano data acquisition system in Appendix C is used. It is used with standart 9 V batteries by arming for some duration just before the test with the aid of test computer. It can collect data up to 100 kHz.

Since the main concern is the shock pulse effect during the launch of test stand, a piezo-rezistive MSI Model 64 type accelerometer in Appendix C is connected to bottom flange of test stand in which the launching pressure is directly applied.

Sample acceleration data measured in pressure gun test stand during launch with 130 bars launch pressure is as in Figure 4.10.

To protect the piezoelectric material from tensile and bending stresses during the impact of test stand to the water which is out of concern, a protection apparatus is mounted on the upper side of compression mass to prevent the motion of it except the compression direction as in Appendix C. Piezoelectric material, CMAR03 or CMAR04 with electrical isolators, compression mass and protection apparatus is mounted on the bottom flange of test stand in which the launching pressure is directly applied as in Figure 4.11.

Figure 4.8 Pressure Gun Launcher

Figure 4.9 Test Stand for Pressure Gun System
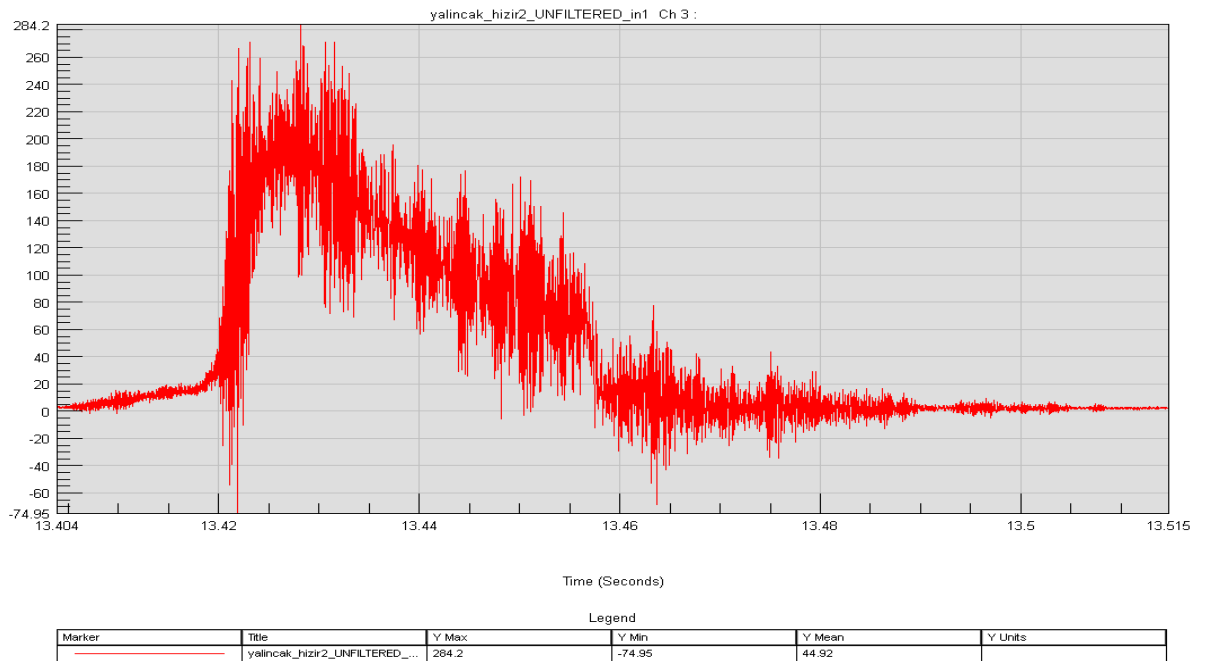
Figure 4.10 Sample Acceleration Data Measured in Pressure Gun Setup

Figure 4.11 Pressure Gun Test Configuration
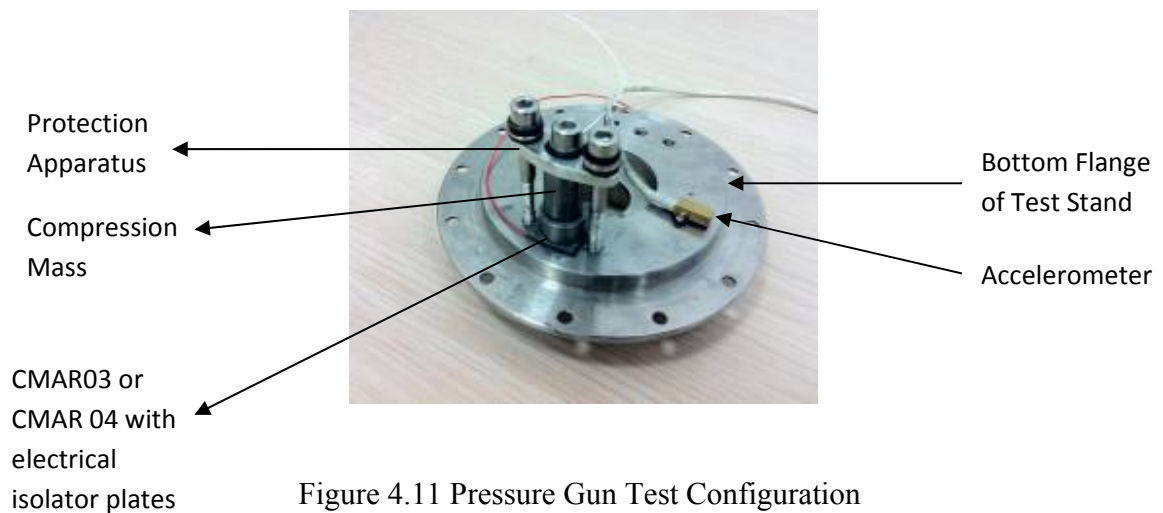
CHAPTER 5

RESULTS

In this part, the results obtained from the experiments and their comparison with mathematical models will be discussed in detail.

Firstly, the mechanical resonator model is verified by employing the resonator parameters and the results in the literature [4].

Secondly, the results obtained from harmonic loading test setup described above will be illustrated. In the third part, the results of mechanical shock loading tests, namely, impact hammer test and pressure gun test will be presented. In the last part of this chapter, the optimum electrical energy storage method to produce the maximum power will be discussed.

5.1. Mechanical Resonator Model Verification

The sample acceleration data in Figure 3.4 is digitized by Engauge program and imported to MATLAB®. 5th degree of polynomial is fitted by basic fitting toolbox of it as in Appendix D in which "y" is acceleration and "x" is time after the acceleration unit is converted to m/s^2.

The corresponding acceleration formula is as in

$$a(t) = \begin{cases} -1.8168 \times 10^{17} t^5 + 4.1122 \times 10^{15} t^4 - 3.1949 \times 10^{13} t^3 + 9.1334 \times 10^{10} t \\ -4.55228 \times 10^7 t + 2873.8 & \text{if} \quad 0 \le t \le 0.00835556 \\ 0 & \text{if} \quad t > 0.00835556 \end{cases} , (5.1)$$

where $a(t)$ is acceleration depending on time, t. The corresponding acceleration graph is as in Figure 5.1 in which the vertical axis unit is m/s^2 and the horizontal axis unit is seconds.
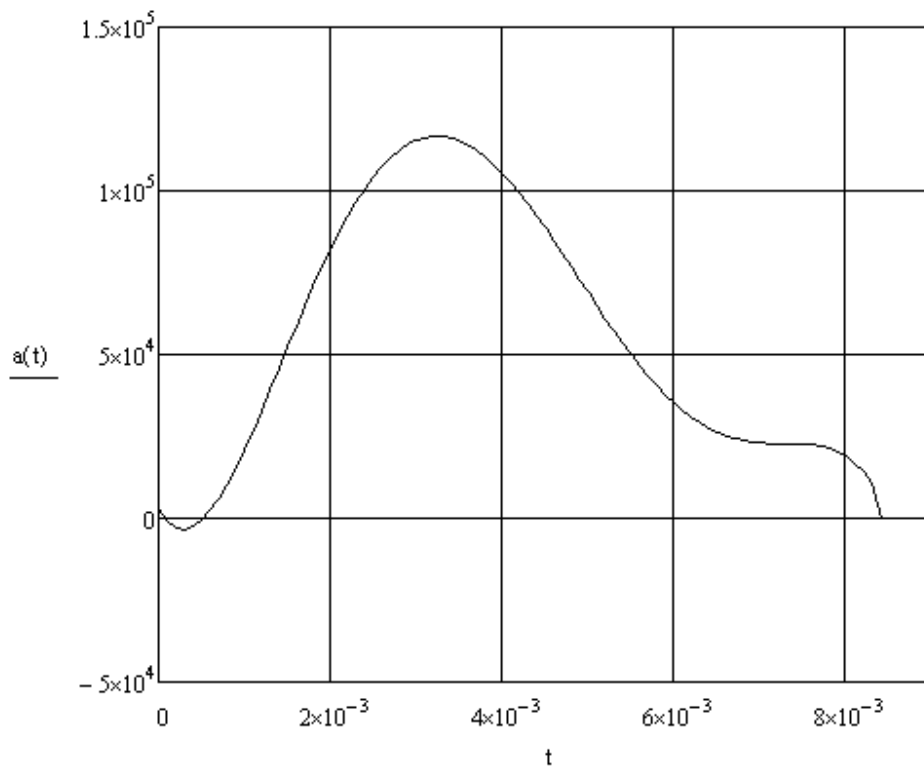
Figure 5.1 The Corresponding Acceleration Data

The resonator stiffness is $2 \times 10^7 \, N/m$ and the resonator mass is $0.1 \; kg$ in [4]. The damping ratio is assumed to be 5 % as an average value since it is not indicated and the structure is a metallic structure containing joints [37].

The implemented acceleration data is multiplied by mass to get the force data, $F(t)$ in mass-spring system.

To get the resonator response the equations in related section is used. To compare and verify the calculated response, the resonator spring acceleration in [4] as in Figure 5.3 is digitized by Engauge program and formulized by MATLAB[®] basic fitting tools similar with reference acceleration data.
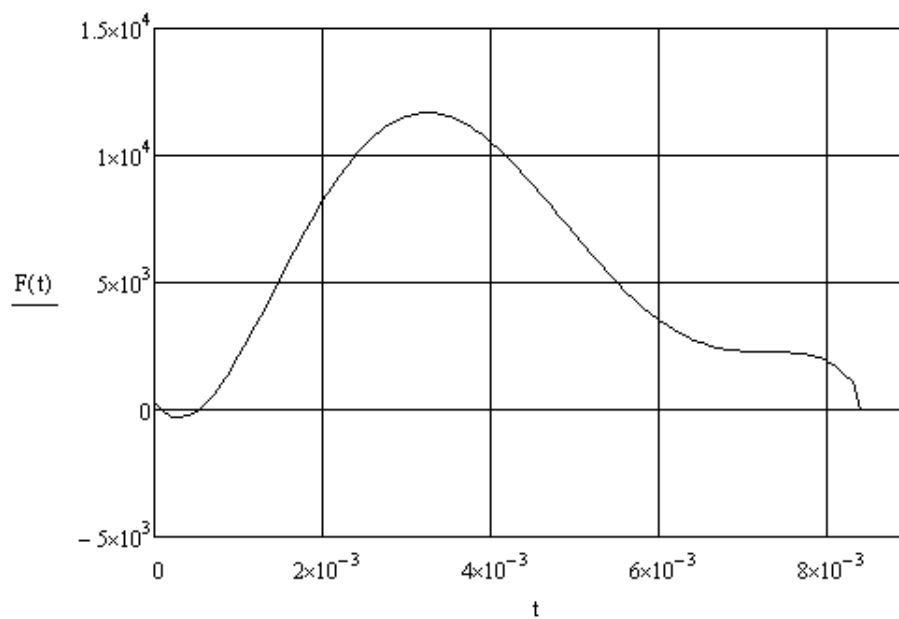
Figure 5.2 Force Developed on Resonator System
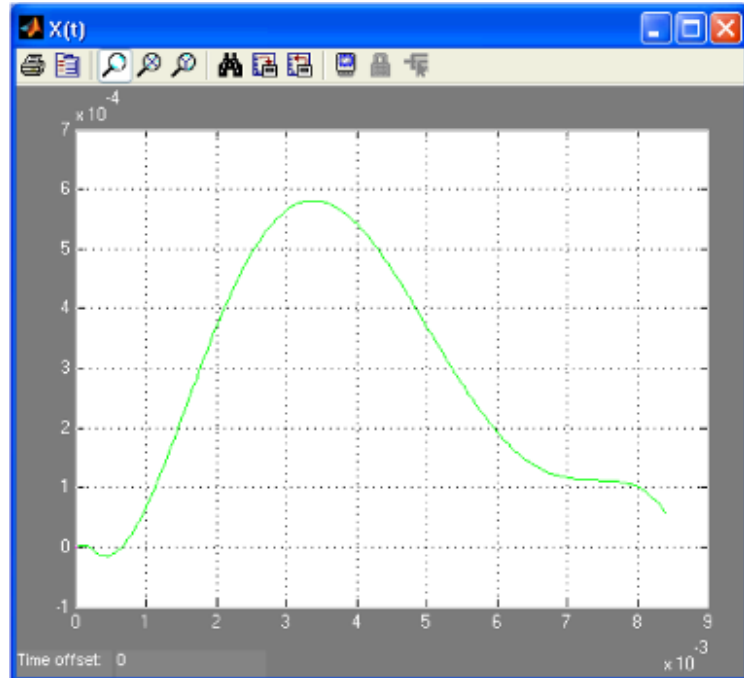
Figure 5.3 Reference Resonator Spring Extension [4]

The calculated and the reference resonator spring extension are compared as in Figure 5.4 where the vertical axis unit is meters and horizontal axis unit is seconds. The difference is because of the digitizing and formulization process and it is accepted that the mathematical model for resonator system is verified.

The force exerted on piezoelectric material could be calculated multiplying the resonator spring extension by the stiffness of the resonator as in Figure 5.5 where the vertical axis unit is Newton and horizontal axis unit is seconds.
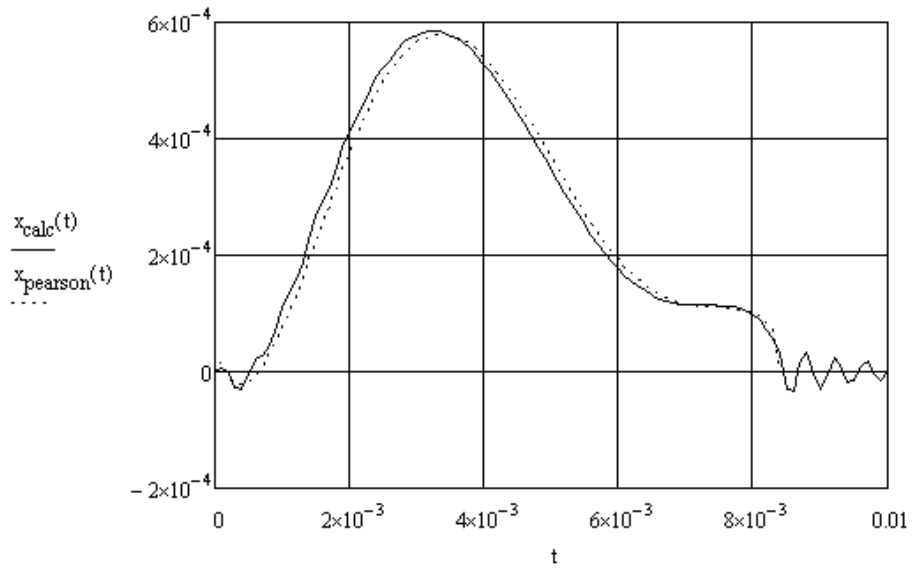
Figure 5.4 The Comparison of Calculated and Reference Resonator Spring Extension
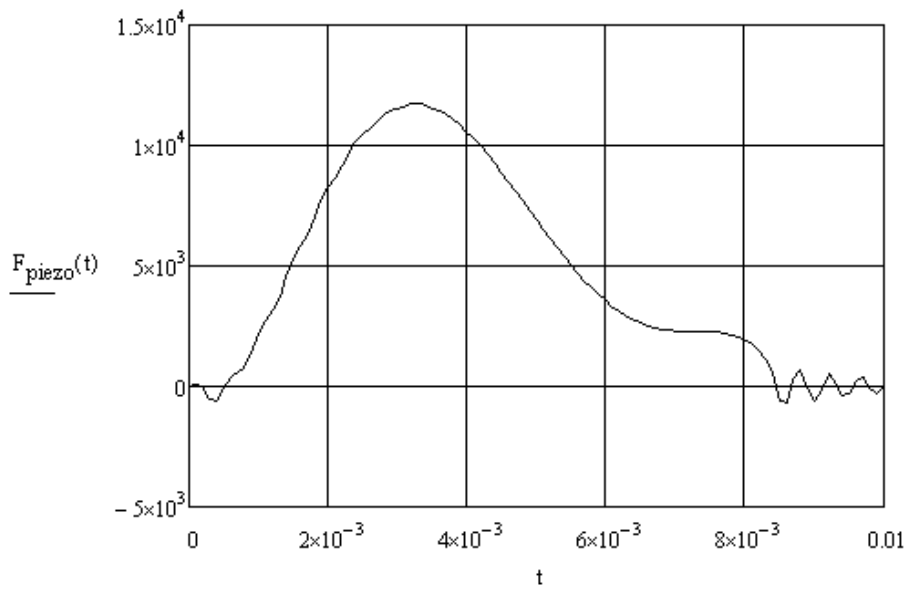
Figure 5.5 The Force Exerted on Piezoelectric Material

5.2. Harmonic Loading Test Results

To have the knowledge of testing a piezoelectric element, measuring the accelerometer and piezoelectric output voltage data, analyzing the problem with analytical and finite element methods, some tests in harmonic loading environment applied by a modal shaker are conducted as described in the previous chapter.

The piezoelectric element is attached with a compression mass of 369.55 grams together with accelerometer with the aid of a M8 bolt. The applied torque is very low because the loading environment concluded very low forces and not to change the characteristics of piezoelectric element like the capacitance.

The frequency of harmonic loading is 100 Hz and the sampling rate is 400 Hz. The acceleration profile is as in Figure 5.6 in which the acceleration level is increased by increasing the amplifier gain. The compression force exerted on piezoelectric element is as in Figure 5.7.

The capacitance of piezoelectric element is calculated as 3.28 nano Farads (nF). However it is measured as 3.12 nF by a multimeter as in Appendix C. This difference is because of uncertainties of the piezoelectric element. The measured capacitance value is used not to have the calculation error related with this difference.

The natural frequency of the material in compression direction is calculated about 33 kHz which is much bigger than excitation frequency, 100 Hz. Because of that, it is determined to calculate the produced voltage by the applied force. The calculated before ORCAD PSPICE® circuit calculations and measured voltage graphs are as in Figure 5.8.
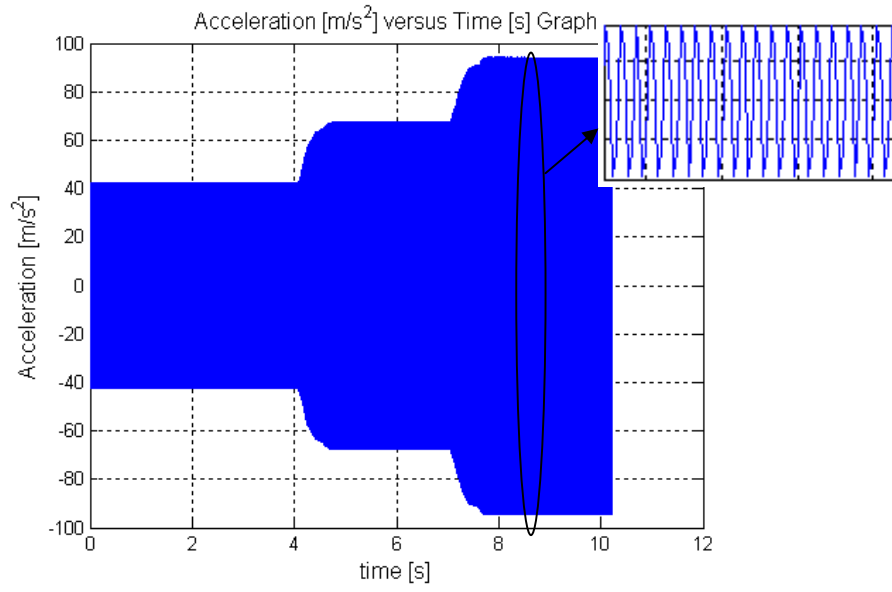
Figure 5.6 The Acceleration Applied on NCE 40 Energy Harvester System in
Harmonic Loading Test
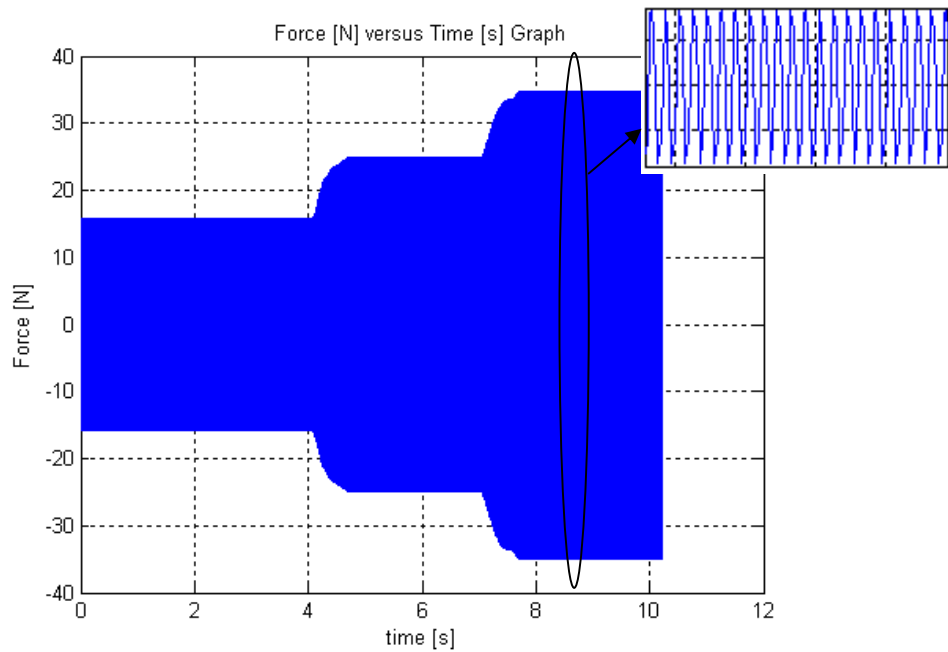
Figure 5.7 The Force Exerted on Piezoelectric Material
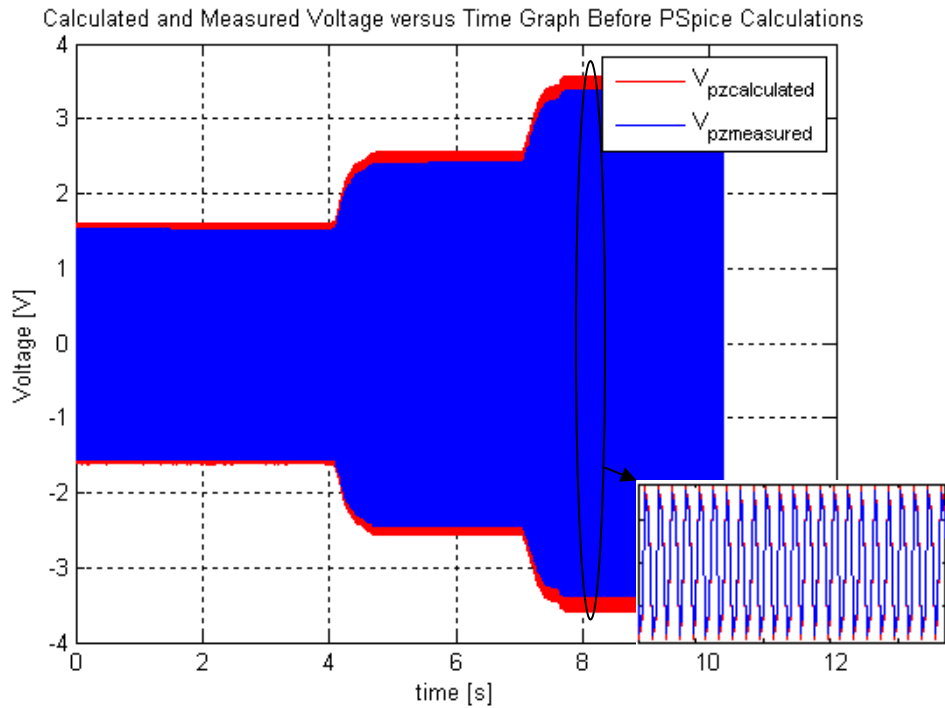
Figure 5.8 Calculated and Measured Voltage Comparison Before ORCAD PSPICE®
Calculations

The calculated voltage is loaded as voltage source in ORCAD PSPICE® model. The
loss resistance is calculated as 1275.3 ohms by taking the operating frequency 100
Hz. The leakage resistance is calculated as 10.0745 mega-ohms by an input voltage
of 10.003 volts and measuring the output voltage as 7.527 volts while by a 3.314
mega-ohms resistance in the related previously described test procedure. The resulted
ORCAD PSPICE® circuit scheme is as in Figure 5.9. The resulted input and output
voltage of the circuit in Figure 5.9 is as in Figure 5.10 in green and red colours,
respectively.
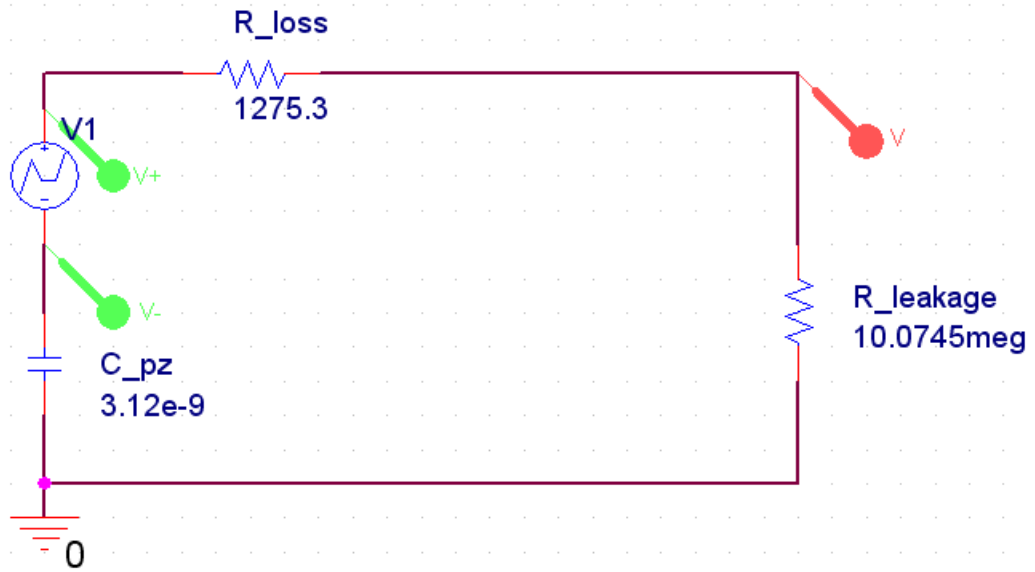
Figure 5.9 ORCAD PSPICE® Circuit Used in Harmonic Loading Test
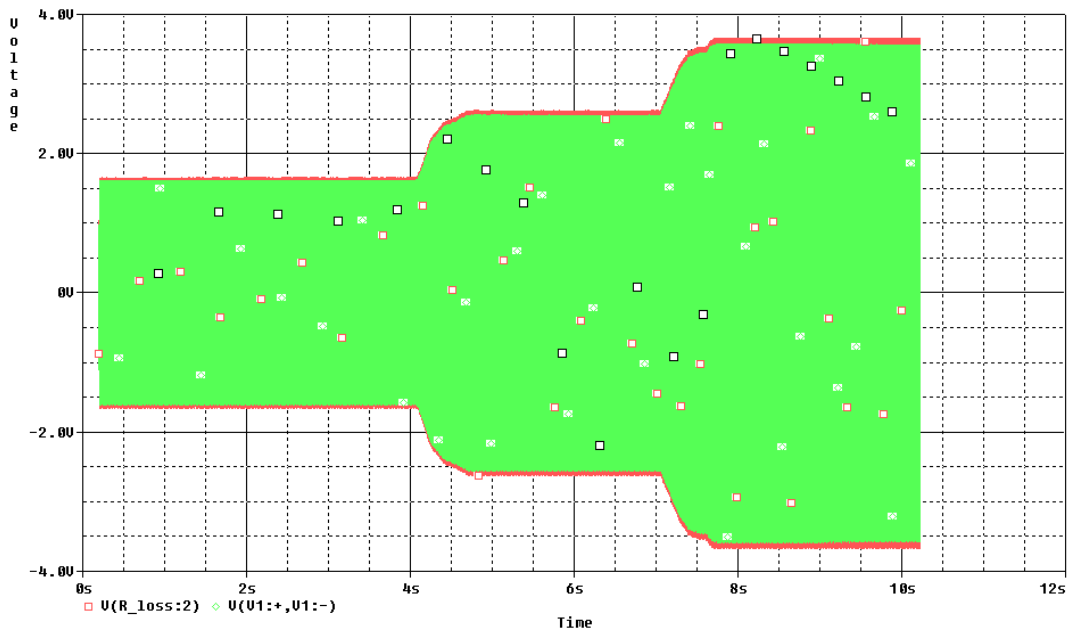
Figure 5.10 The Input and Output Voltage after ORCAD PSPICE® Calculations

The output voltage from ORCAD PSPICE® Calculations is exported from ORCAD PSPICE® and imported to MATLAB® to compare with the measured voltage values. The difference between the calculated and measured values is less than 9 % which can be accepted to come from manufacturing process etc.
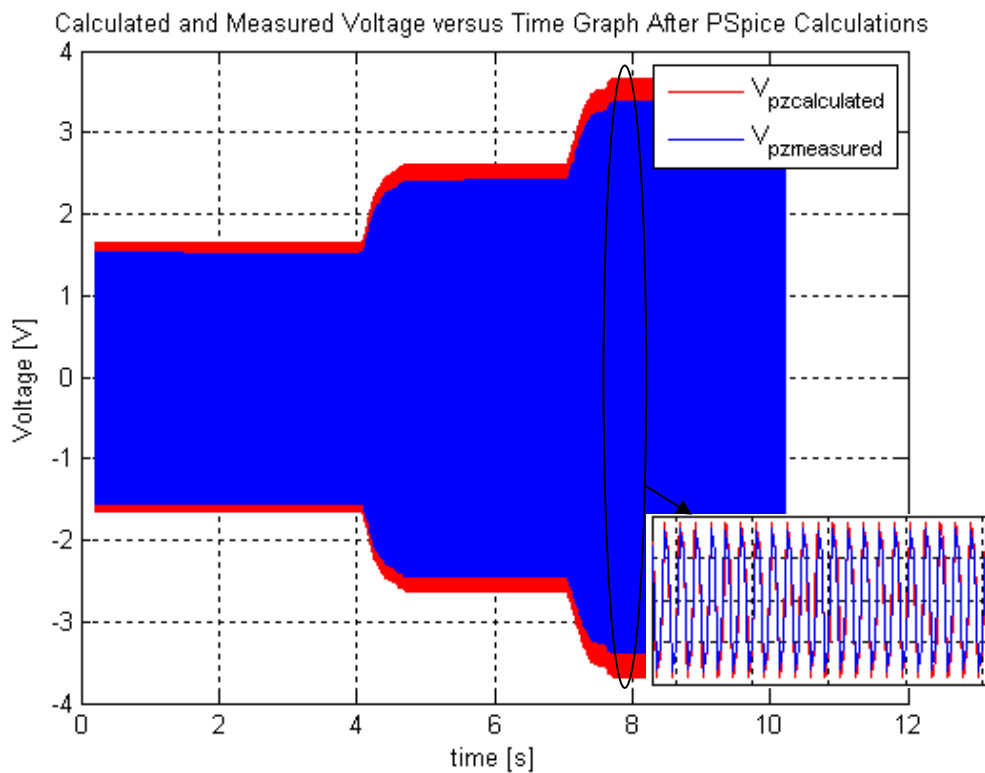
Figure 5.11 Calculated and Measured Voltage Comparison after ORCAD PSPICE® Calculations

This test is also analyzed in ATILA® finite element analysis module by harmonic analysis module.

NCE 40 ring material and compression mass is modelled in GID Pre-processor as in Figure 5.12 with blue and green colours, respectively. The compression mass height is arranged to have the same weight with measured value, 36.955 grams. Steel compression mass and piezoelectric material, NCE 40, properties are entered as in Appendix D. Some material properties, s_{12}^{E}, s_{13}^{E}, s_{44}^{E}, d_{15} and ε_{11}^{T} are not displayed in material data sheet and the producer also does not have this data. Since "33" mode is used, this material properties does not have a direct effect for the results. Because of that, they are entered same with PZT 4 material which is already in the ATILA$^{®}$ piezoelectric material database.

The electric potential conditions of electrodes of piezoelectric material are defined as in Figure 5.13. The upper surface of piezoelectric material is grounded to also isolate the steel compression mass as in the test conditions with the aid of electrical isolator plates. The lower surface of piezoelectric material is in floating boundary condition.
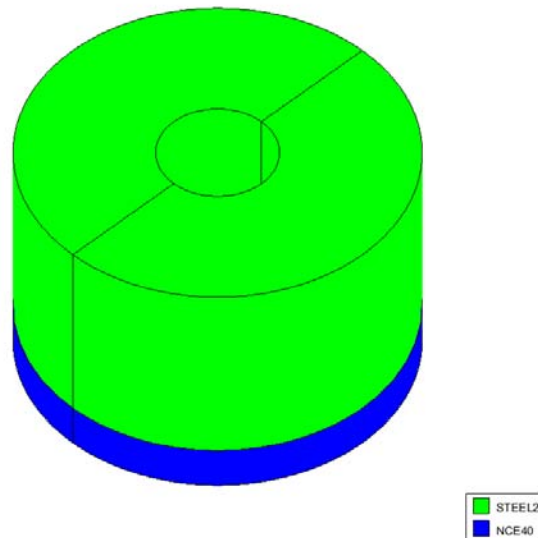
Figure 5.12 NCE 40 and Compression Mass in ATILA$^{®}$

Floating 0.0 0.0 0
0.0 0.0 0.0 External
1.0 10.0 0.001
Ground 0.0 0.0 0
0.0 0.0 0.0 External
1.0 10.0 0.001
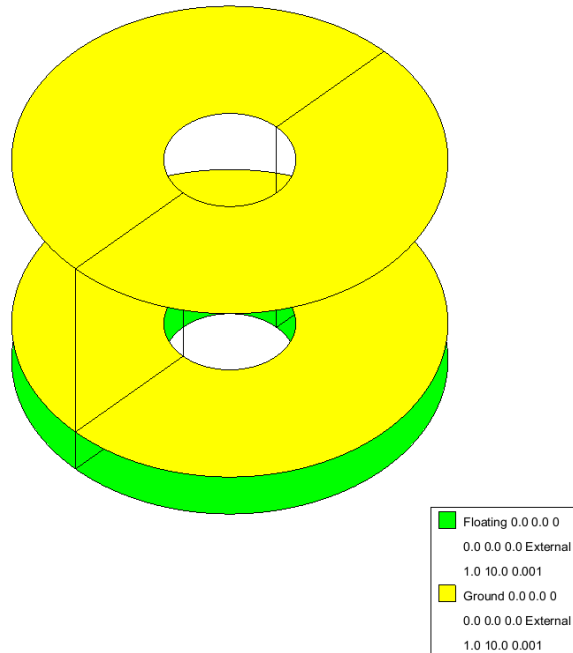
Figure 5.13 Surface Electric Potential Conditions

It is necessary to enter polarization conditions of materials including elastic materials in ATILA$^{®}$ piezoelectric analysis. The polarization condition of piezoelectric material is entered in positive z direction, 3rd direction in Figure 2.1, as in Figure 5.14. The polarization direction of the steel compression mass is entered the same.

In ATILA$^{®}$, the acceleration definition is not allowed in harmonic analysis module. It can only be defined in transient analysis module which will be applied in following sections. Instead, the displacement value is calculated and entered by

$$x = \frac{\ddot{x}}{-\omega^2} .$$
(5. 2)

The acceleration profile in Figure 5.11 has different levels. The acceleration value is taken to be -90.4564 m/s^2 from the acceleration measurements as in Appendix D.

The corresponding displacement is calculated as 0.2288 mm and defined in ATILA®
as in Figure 5.15.

Applying all boundary conditions, the finite element model of the piezoelectric
energy harvester is created as in Figure 5.16 with 256 HEXA20P piezoelectric
elements having 1440 nodes.

The corresponding voltage is calculated as 3.65 Volts as in Figure 5.17. The voltage
measured in the reference time is 3.19 Volts as in Appendix D.
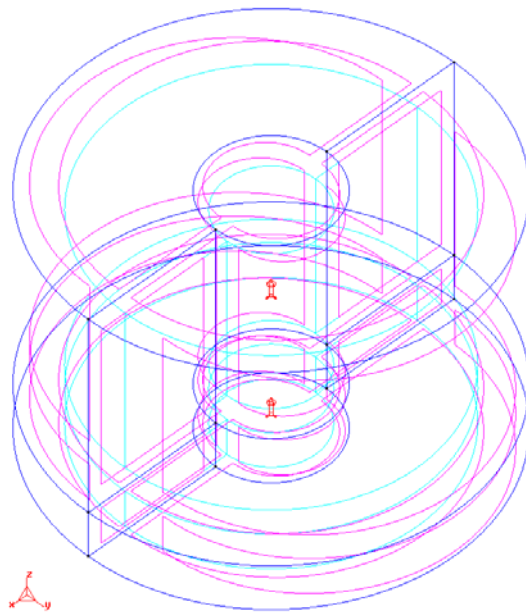
Figure 5.14 Polarization Conditions of Materials
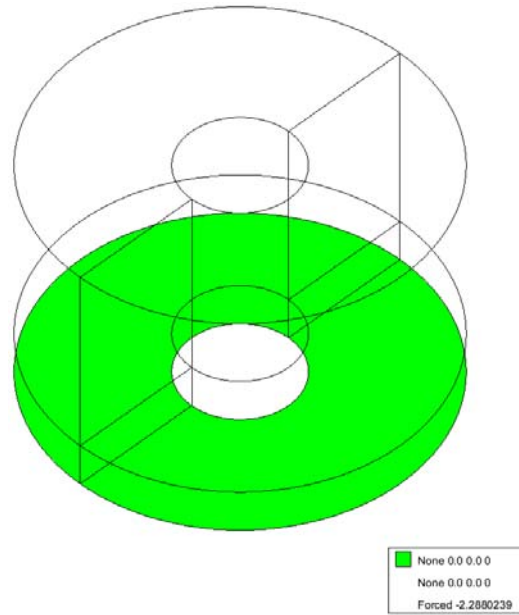
Figure 5.15 Displacement Definition in ATILA®
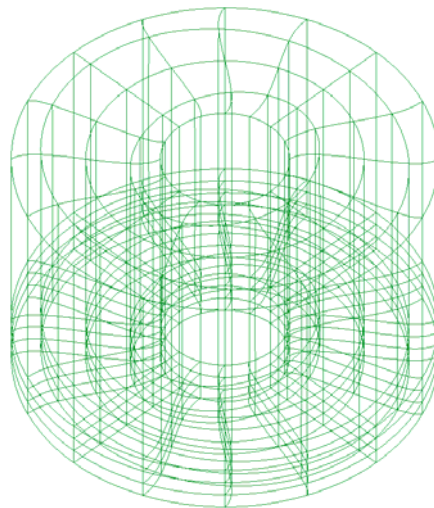
Figure 5.16 Finite Element Model of NCE40 and Compression Mass

87
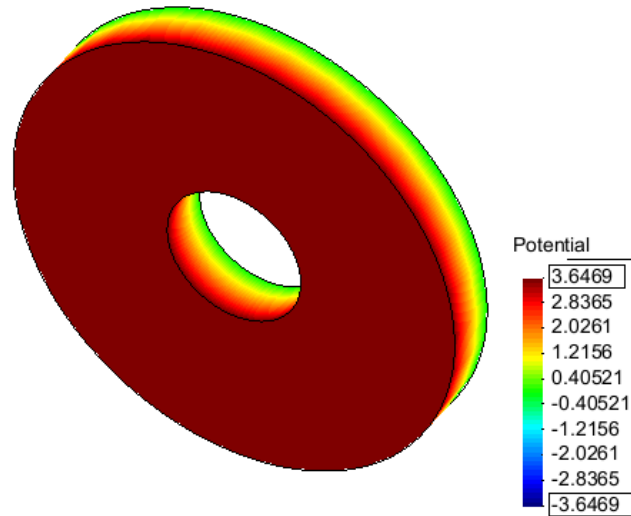
Figure 5.17 ATILA$^{®}$ FEM Result

Since the capacitance of piezoelectric material directly affects the output voltage, its correctness is controlled. In ATILA, there is not a direct menu to control the capacitance of the piezoelectric energy harvester. To control it, a methodology described by ATILA engineers is applied.

The displacement value entered as in Figure 5.15 is erased and the frequency is arranged as 1 Hz to eliminate the motional effects. 1 Volt is applied in the lower surface of piezoelectric material as in Figure 5.18.

After the harmonic analysis is done with these conditions, the reactance value which is the opposition of the piezoelectric energy harvester to a change of electric current or voltage is obtained as in Figure 5.19.

The corresponding capacitance value is calculated as 2.75 nF by

$$C = -\frac{1}{2\pi f x_c},$$ (5. 3)

where x_c is the capacitive reactance while the measured capacitance value is 3.12 nF. To correct this capacitance difference, a correction factor, 0.88 is used. The concluded voltage output is 3.22 Volts with an error smaller than 1 % when compared with measured value.
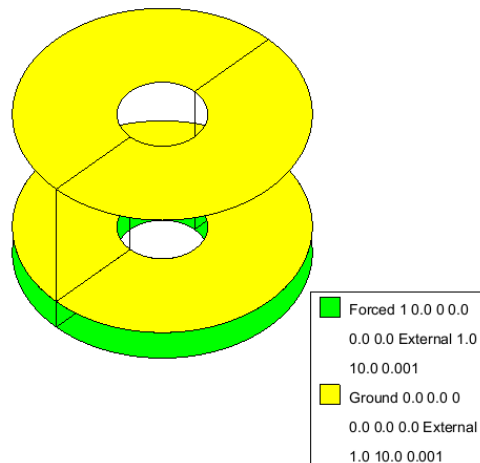
Figure 5.18 Voltage Application
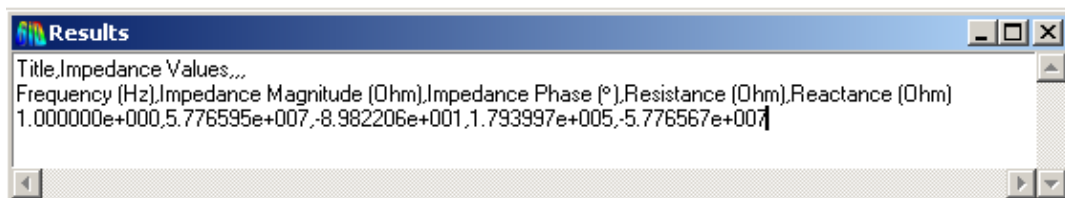
Figure 5.19 The Reactance Value Obtained in ATILA

5.3. Mechanical Shock Loading Test Results

5.3.1. Impact Hammer Test Results

In these tests, Dytran 3200B2M accelerometer with 50000 g measuring capability whose properties are as in Appendix is used. The upper frequency limit of this accelerometer is 10 kHz and the frequency content bigger than this limit is filtered by a low pass filter at 10 kHz in nCode Glyphworks[®].

The acceleration profile applied in impact hammer test setup is as in Figure 5.20. The measured piezoelectric energy harvester output voltage data is as in Figure 5.21.
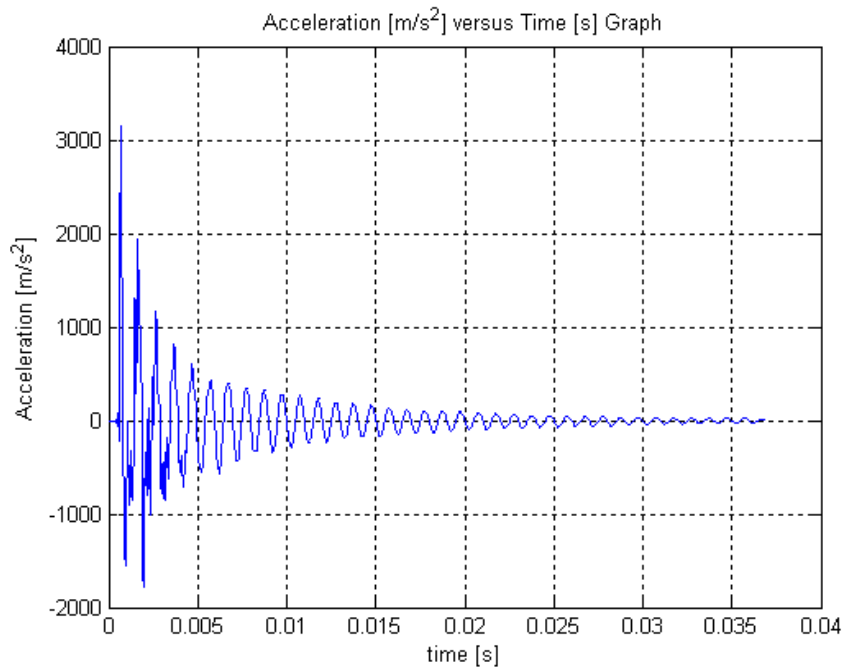
Figure 5.20 The Acceleration Applied on Impact Hammer Test Setup
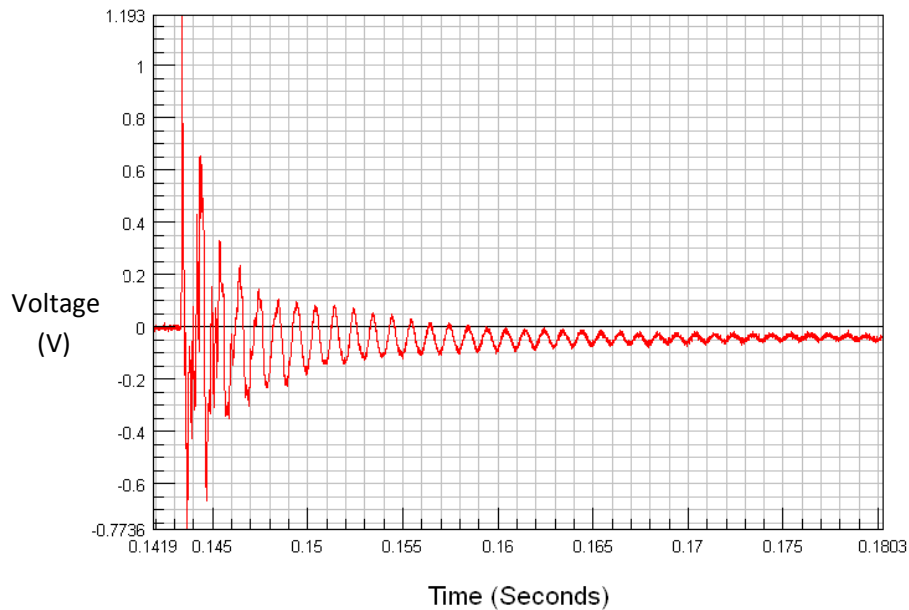
Figure 5.21 Piezoelectric Output Voltage Graph

When the reason behind the shift of voltage signal from the zero base-line is investigated, it is determined to be "zero shift" phenomenon which is mainly because of the excitation of the resonance of piezoelectric materials and considered especially in piezoelectric accelerometer design [42]. This shift has unpredictable amplitude and duration. The reasons behind this shift can be overstressing of sensing elements, physical movement of sensor parts, cable noise, base strain induced errors, inadequate low frequency response and overloading of signal conditioner [43]. In accelerometer design, to prevent overstressing of piezoelectric material and base strain induced errors, mechanical filters as in Figure 5.22 are used containing an internal butyl rubber core [44].

This effect is thought to be out of scope since the acceleration environment of gunfire applications as in Figure 3.4 has low frequency content different from impact hammer test setup case. To compare the calculations and measurements and not taking into account zero shift effects a high pass filter with 100 Hz [39] is applied to

piezoelectric voltage data as in Figure 5.23 by nCode Glyphworks$^®$ in which the graph with blue colour is filtered and the other is original data.

The compression mass is 16.6 grams including bolt head weight. Bolt head expected to act as a compression mass since the bolt is already in tension and when the compression mass moves in compression direction it also compresses the piezoelectric stack. The compression force exerted on piezoelectric element is as in Figure 5.24.

The capacitance of piezoelectric element is calculated as 378 nF by applying an area factor of 0.75 since the electrodes cover approximately 75 % of piezoelectric element which is indicated by Noliac Company. The capacitance is measured as 386 nF by a multimeter as in Appendix C. This difference is because of uncertainties of the piezoelectric element.
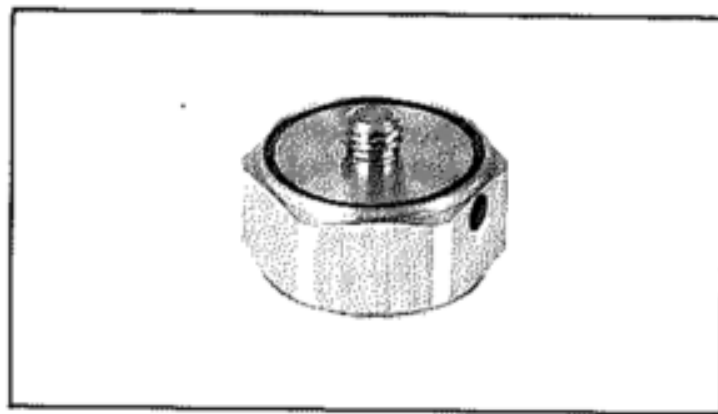
The Mechanical Filter UA 0559

Figure 5.22 Sample Mechanical Filter Used in Accelerometers [44]
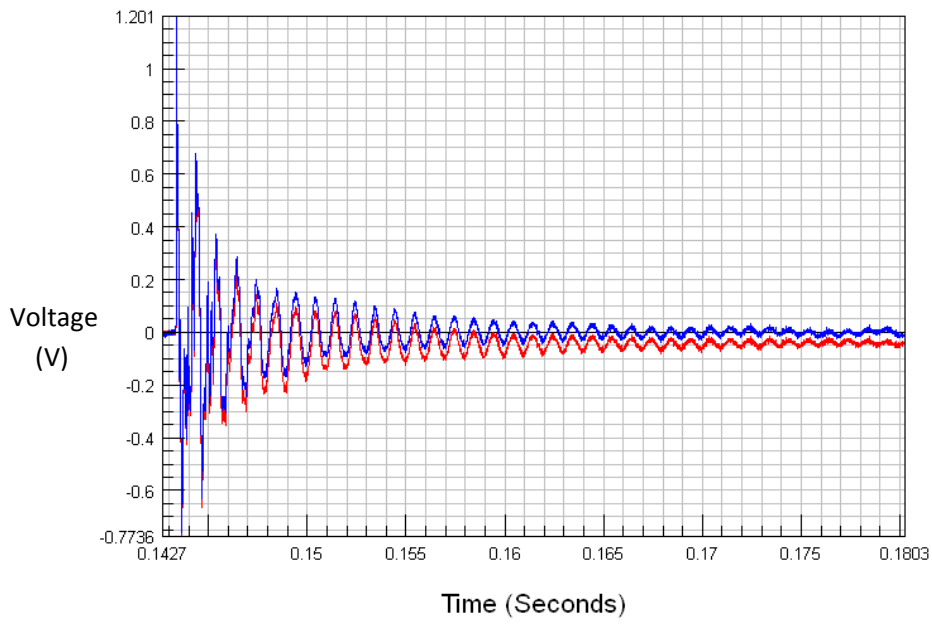
Figure 5.23 Filter Applied Piezoelectric Output Voltage Signal
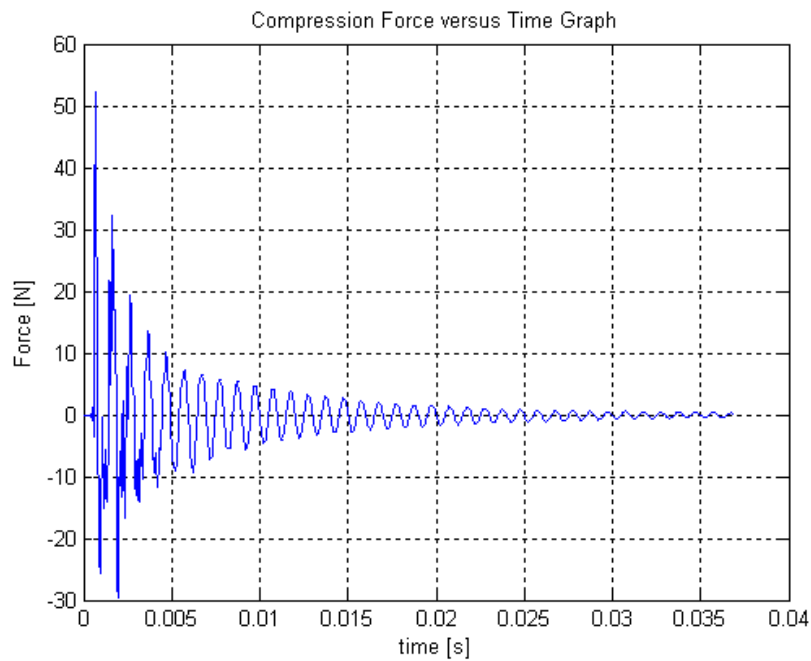
Figure 5.24 The Force Exerted on CMAR03 Piezoelectric Material

93

To attach the piezoelectric energy harvester system to the test stand, a M5 bolt is used with 1 Nm tightening torque. The preload because of tightening the bolt results in decrease in layer thickness and increase in layer area. This results in increase in capacitance of piezoelectric stack considering the capacitance calculation formula, 3.47. The capacitance of piezoelectric stack increases to 396 nF as in Appendix C. The measured capacitance value after tightening is used not to have the calculation error related with this difference.

The produced voltage is calculated by the applied force or the mechanical stress. Lumped parameter modelling is used by fast Fourier transform (FFT) method since it is not possible to formulate the compression loading depending on time. Distributed parameter modelling could not be applied because of the same reason.

The natural frequency of piezoelectric material with compression mass is calculated as 53209 Hz. In the calculation of output voltage by the applied force, the produced charge difference between the layers because of the compression effect of upper layers is also considered. This effect would be important especially in thick multilayer piezoelectric stacks. The calculated and measured voltage graphs are as in Figure 5.34. The graph in dark blue colour is the voltage calculated by force not considering the charge difference in layers while the graph in red colour is created by considering this difference. The graph in black colour is the voltage calculated by lumped parameter modelling and mechanical stress.

The loss resistance is calculated as 6.8 ohm by finding the main frequency of loading as 1003 Hz taking the frequency spectrum of acceleration data in Figure 5.20 as in Figure 5.26 by nCode Glyphworks®.
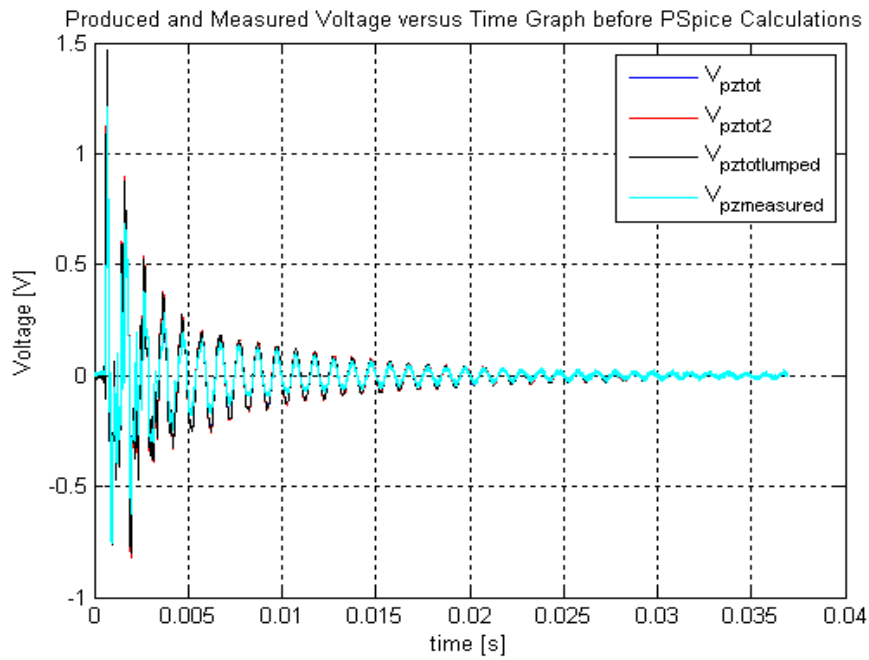
Figure 5.25 Calculated and Measured Voltage Comparison before ORCAD PSPICE[®]
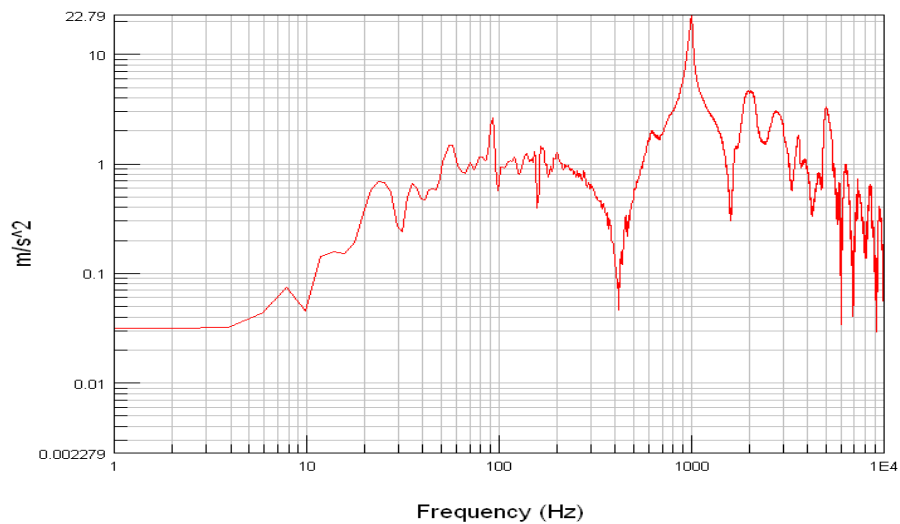
Calculations

Figure 5.26 Frequency Spectrum of Acceleration Data

The leakage resistance is calculated as 10.0962 mega-ohms by an input voltage of 10.003 volts and measuring the output voltage as 7.531 volts while by a 3.314 mega-ohms resistance in the related previously described test procedure.

The resistance of the data collection cable is also taken into account and it is measured 326.2 kilo-ohms as in Appendix C.

The resulted ORCAD PSPICE® circuit scheme by loading calculated voltages is as in Figure 5.27.

After simulating the piezoelectric energy harvester system in ORCAD PSPICE®, the results are exported to compare with voltage measurements. The produced and calculated voltage characteristics are not very convenient as in Figure 5.28 and Figure 5.29. Because of the zero shift effects, tensile loadings and different characteristics of acceleration in shock plate etc., the experimental test results are not harmonious enough with analysis results. These factors are not valid for munitions applications. Thus, it is determined to create a test setup having similar characteristics with gunfire applications.
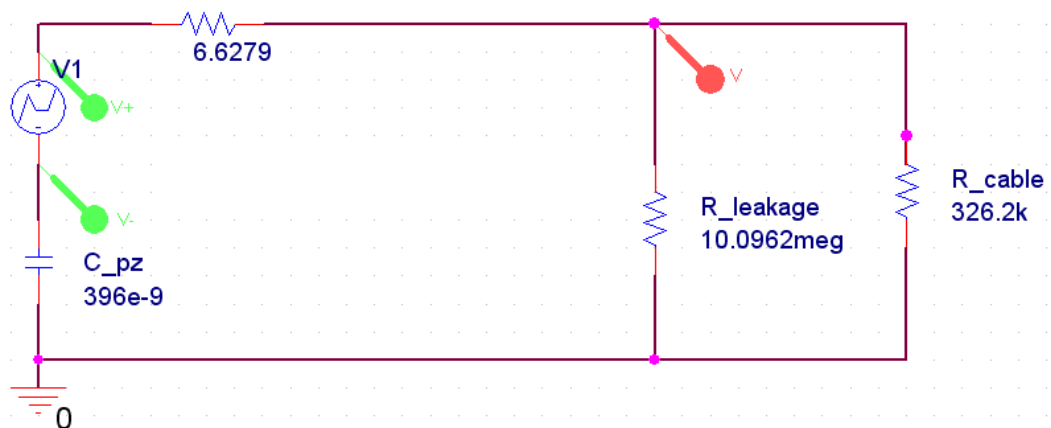
Figure 5.27 ORCAD PSPICE® Circuit of CMAR03
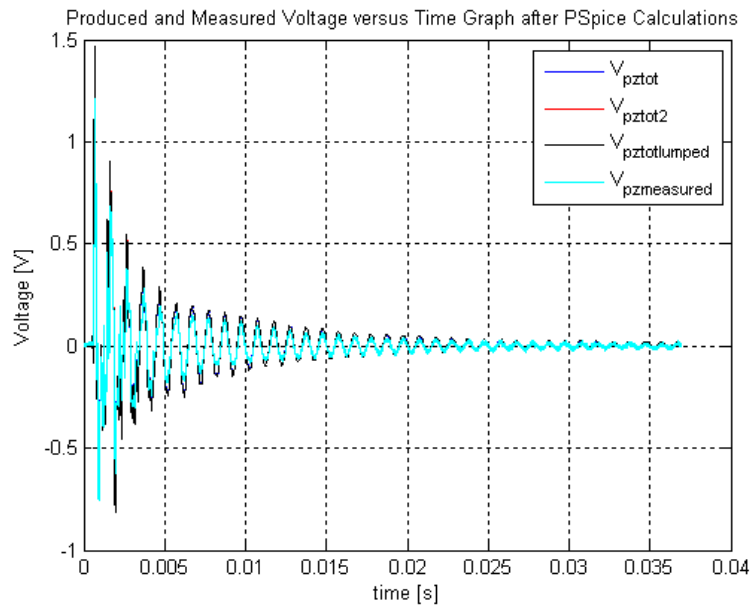
Figure 5.28 Calculated and Measured Voltage Comparison after ORCAD PSPICE®
Calculations
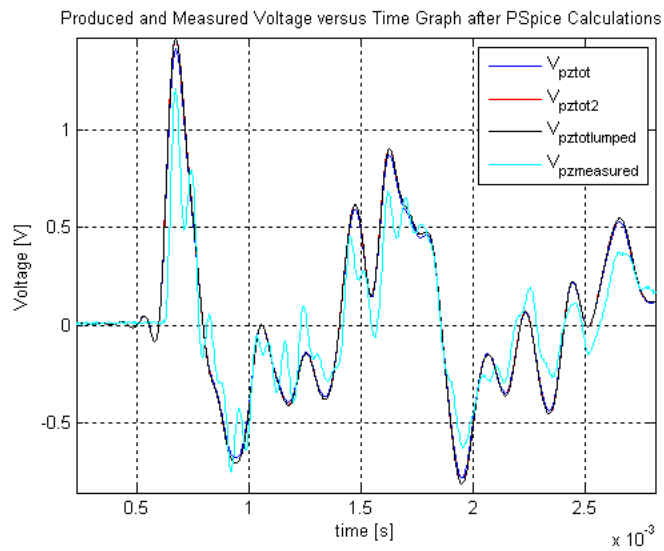
Figure 5.29 Calculated and Measured Voltage Comparison after ORCAD PSPICE®
Calculations - 2

5.3.2. Pressure Gun Test Results

To simulate the high-G shock environment, impact hammer tests are conducted. However, in these tests, impact hammer excites a big frequency band and zero-shift effect occurs as mentioned before. These effects are out of concern in gunfire environment when the sample gunfire acceleration in Figure 3.4 with duration of several milliseconds is considered.

Two different multilayer piezoelectric stacks, CMAR03 and CMAR04, are tested in this test setup. In these tests, the acceleration and piezoelectric voltage data is collected with 100 kHz sampling rate. The collected acceleration and piezoelectric voltage data is applied a low pass filter of 500 Hz not to deal with either the signal noise or high frequency vibrations because of lack of rigidity of bottom flange of pressure gun test stand. The comparison of sample acceleration and piezoelectric voltage data with and without filtering is as in Figure 5.30 and Figure 5.31, respectively.

Time (Seconds)

Marker	Axis	Title	Y Max	Y Min	Y Mean	Y Units
	A	yalincak_hizir3_...	2496	-587.9	688	m/s^2
	A	yalincak_hizir3_...	1652	0.508	687.7	m/s^2
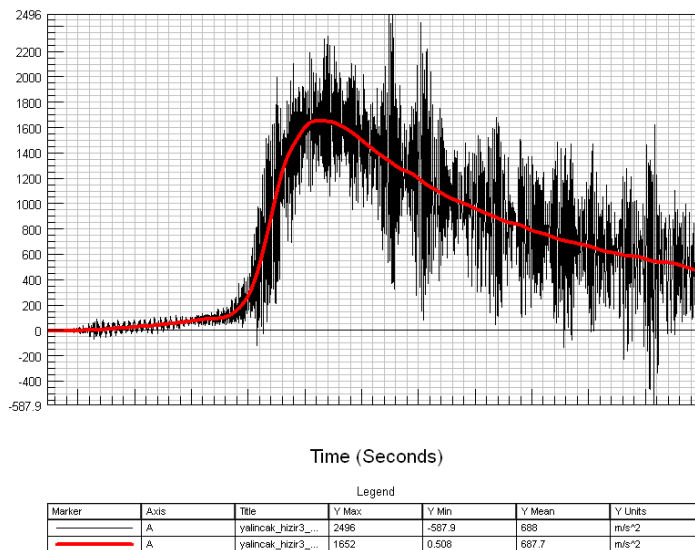
Figure 5.30 The Acceleration Data Comparison by Filtering

Marker	Axis	Title	Y Max	Y Min	Y Mean	Y Units
	A	piezo_test3_...	0.9306	-0.2312	0.2119	V
	A	piezo_test3_...	0.7201	-0.002073	0.2123	V
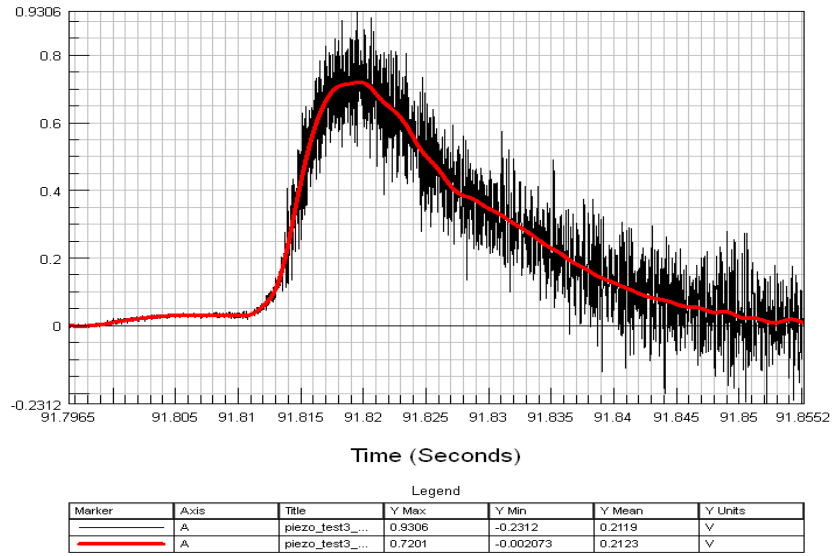
Figure 5.31 The Voltage Data Comparison by Filtering

5.3.2.1.   CMAR03 Test Results

The acceleration profile applied by pressure gun in the launch duration is as in Figure 5.32.

The compression mass is 16.12 grams including washer and bolt head weights. Bolt head expected to act as a compression mass since the bolt is already in tension and when the compression mass moves in compression direction it also compresses the piezoelectric stack. The compression force exerted on piezoelectric element is as in Figure 5.33.
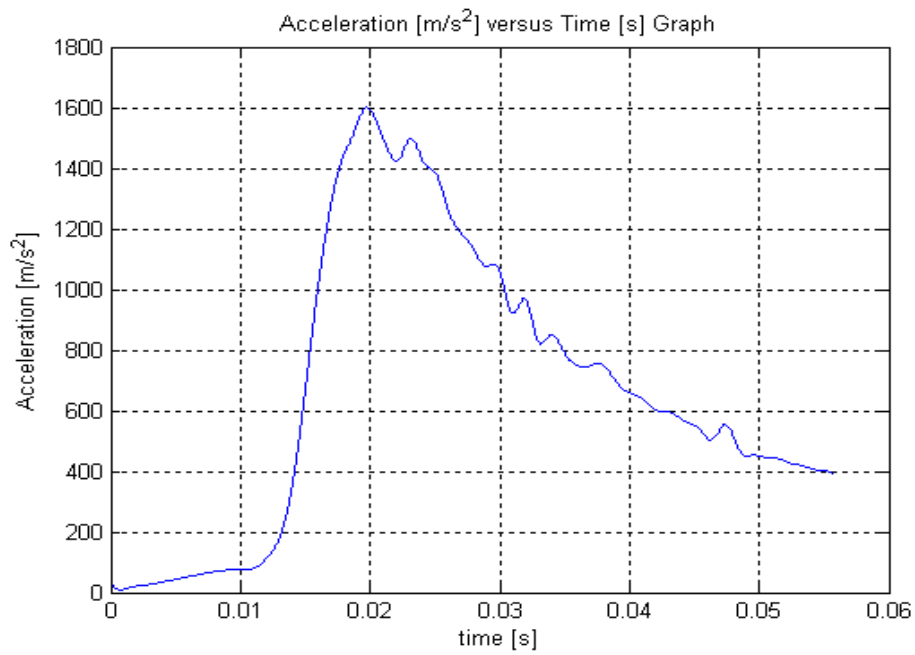
Figure 5.32 The Acceleration Applied on CMAR03 Piezoelectric Energy Harvester
System
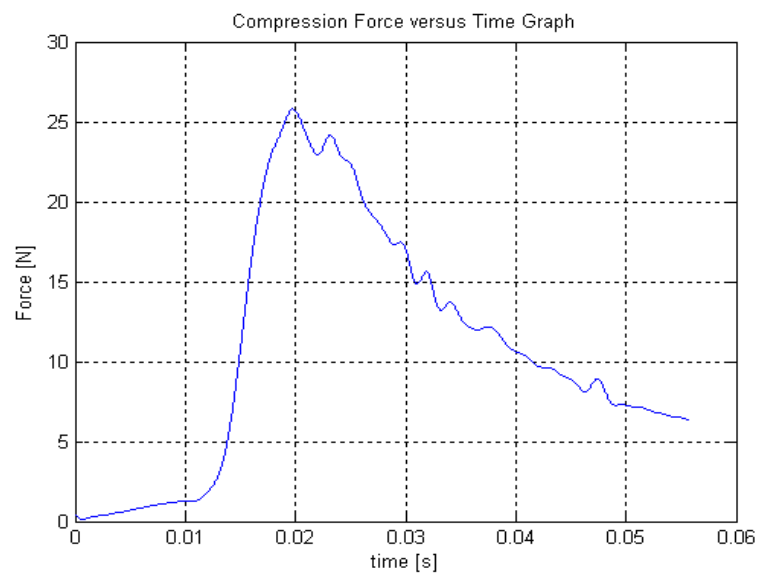
Figure 5.33 The Force Exerted on CMAR03 Piezoelectric Material

To attach the piezoelectric energy harvester system to the test stand, a M5 bolt is used with 2 Nm tightening torque. The capacitance of piezoelectric stack increases to 407 nF as in Appendix C. The measured capacitance value after tightening is used not to have the calculation error related with this difference.

The produced voltage is calculated by the applied force or the mechanical stress. Lumped parameter modelling is used by fast Fourier transform (FFT) method since it is not possible to formulate the compression loading depending on time. Distributed parameter modelling could not be applied because of the same reason.

The natural frequency of piezoelectric material with compression mass is calculated as 53124 Hz. In the calculation of output voltage by the applied force, the produced charge difference between the layers because of the compression effect of upper layers is also considered. This effect would be important especially in thick multilayer piezoelectric stacks. The calculated and measured voltage graphs are as in Figure 5.34. The graph in dark blue colour is the voltage calculated by force not considering the charge difference in layers while the graph in red colour is created by considering this difference. The graph in black colour is the voltage calculated by lumped parameter modelling and mechanical stress which is almost the same with the dark blue one. The reason behind is the loading condition is quasi-static condition with a frequency content much lower than the first natural frequency of piezoelectric energy harvester in compression mode. Because they are the same, only the output voltage with dark blue colour is used in ORCAD PSPICE® calculations. The graph in light blue colour is measured piezoelectric output voltage.

The loss resistance is calculated as 303 ohm by finding the main frequency of loading as 22 Hz taking the frequency spectrum of acceleration data in Figure 5.32 as in Figure 5.35.
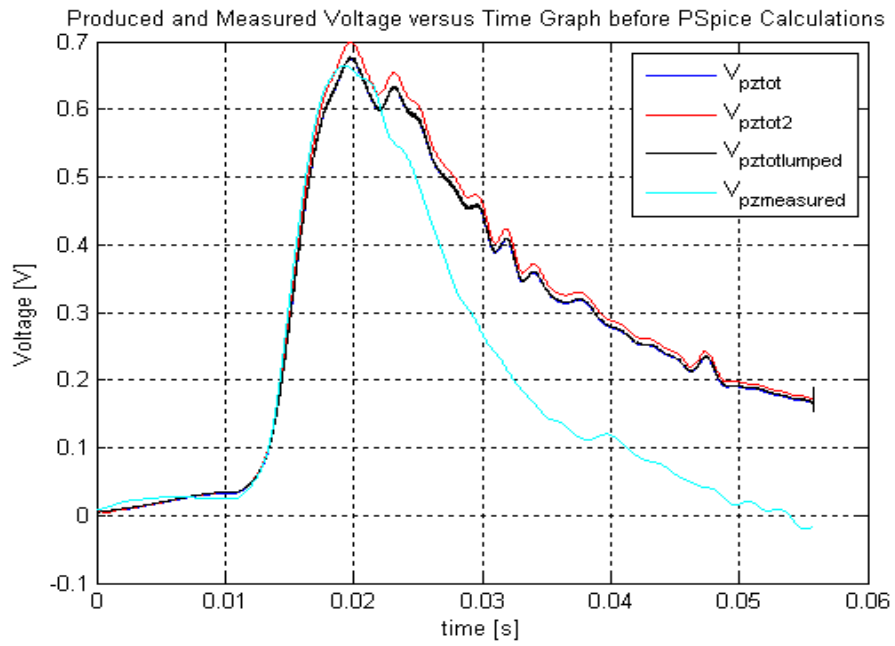
Figure 5.34 Calculated and Measured Voltage Comparison before ORCAD PSPICE®
Calculations
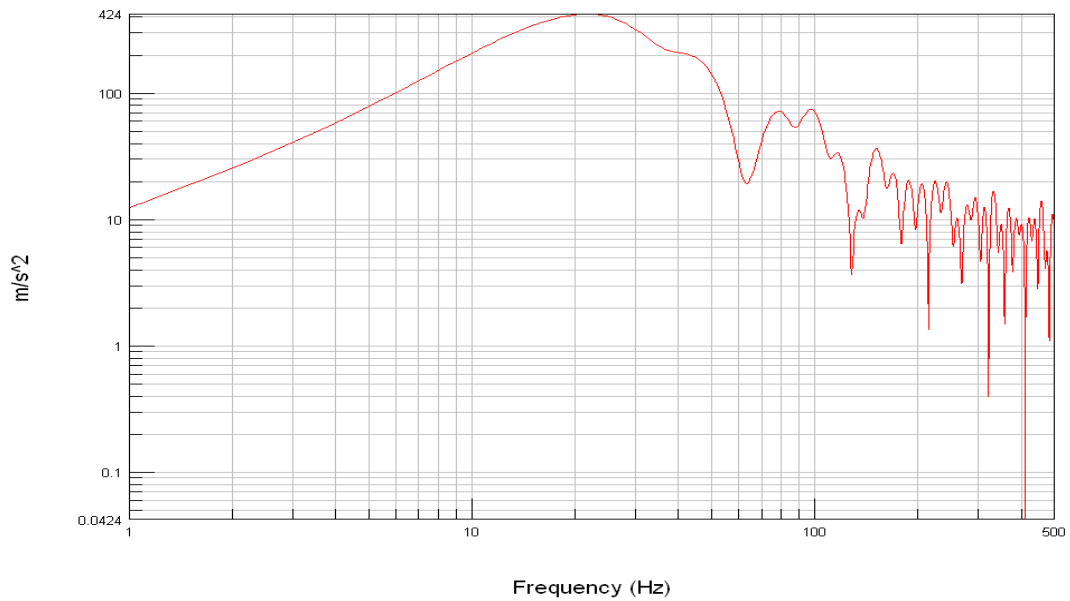
Figure 5.35 Frequency Spectrum of Acceleration Data

The leakage resistance is calculated as 10.0962 mega-ohms by an input voltage of 10.003 volts and measuring the output voltage as 7.531 volts while by a 3.314 mega-ohms resistance in the related previously described test procedure. The resulted ORCAD PSPICE® circuit scheme by loading calculated voltages is as in Figure 5.36. The resulted input and output voltage is as in Figure 5.37 in green and blue colours, respectively.

The output voltage from ORCAD PSPICE® Calculations is not similar with measured voltage in Figure 5.34. To collect the output voltage data by Slice Nano Data Acquisition System, a cable which enables to measure voltages up to 20 Volts with voltage divider is used. The electrical scheme of this cable is as in Appendix C.

Equivalent resistance of the cable is measured as 110.1 kilo-ohms as in Appendix C. This resistance is connected with piezoelectric element as in Figure 5.38.

After the modification, the resulted output voltage with blue colour changed its shape as in Figure 5.39.
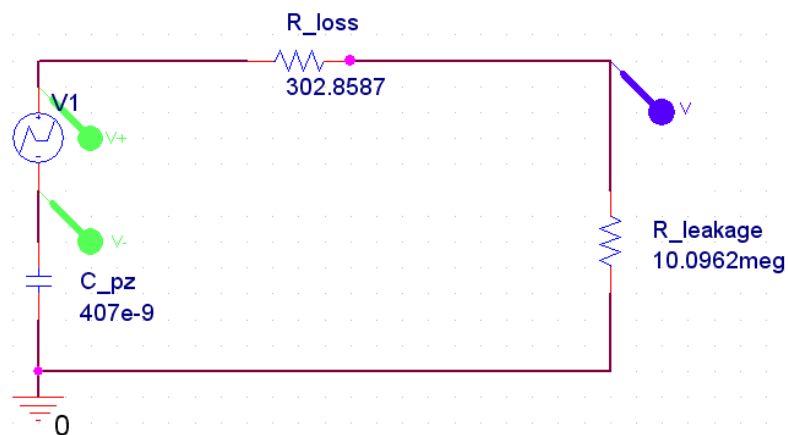
Figure 5.36 ORCAD PSPICE® Circuit of CMAR03
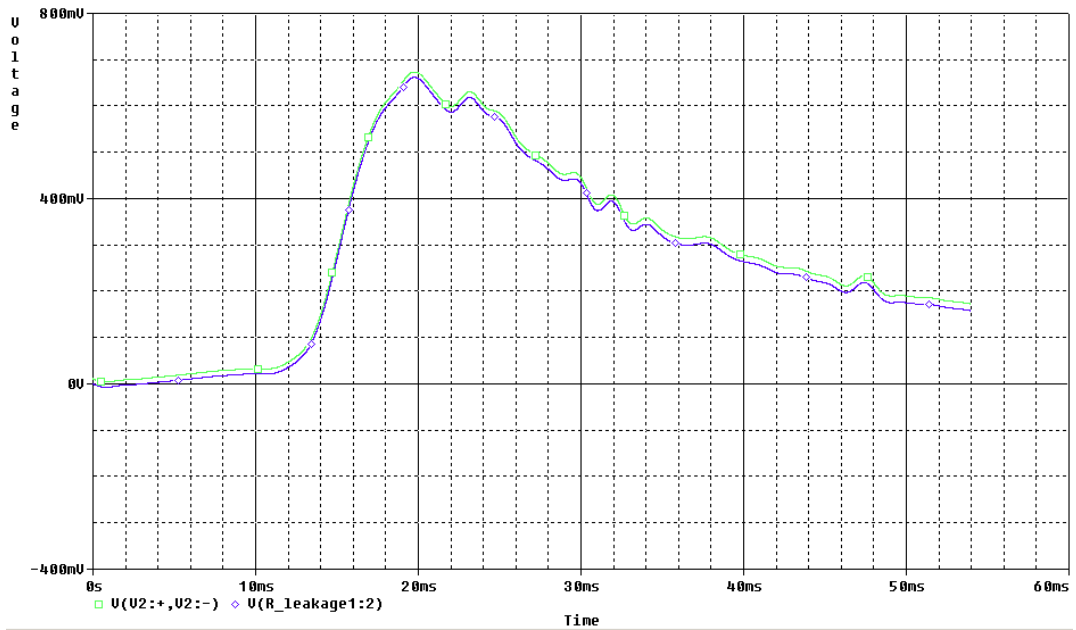
Figure 5.37 The Input and Output Voltage after ORCAD PSPICE® Calculations
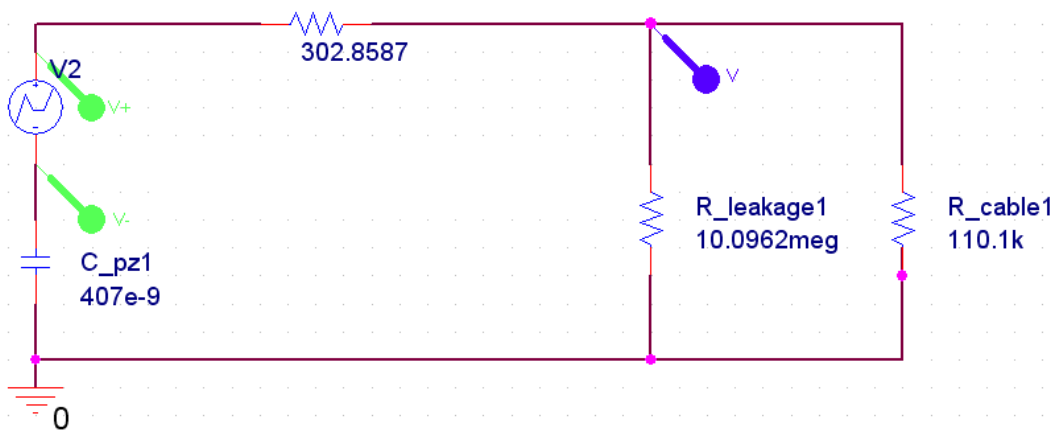
Figure 5.38 CMAR03 connected with 4865-01 Cable in ORCAD PSPICE®
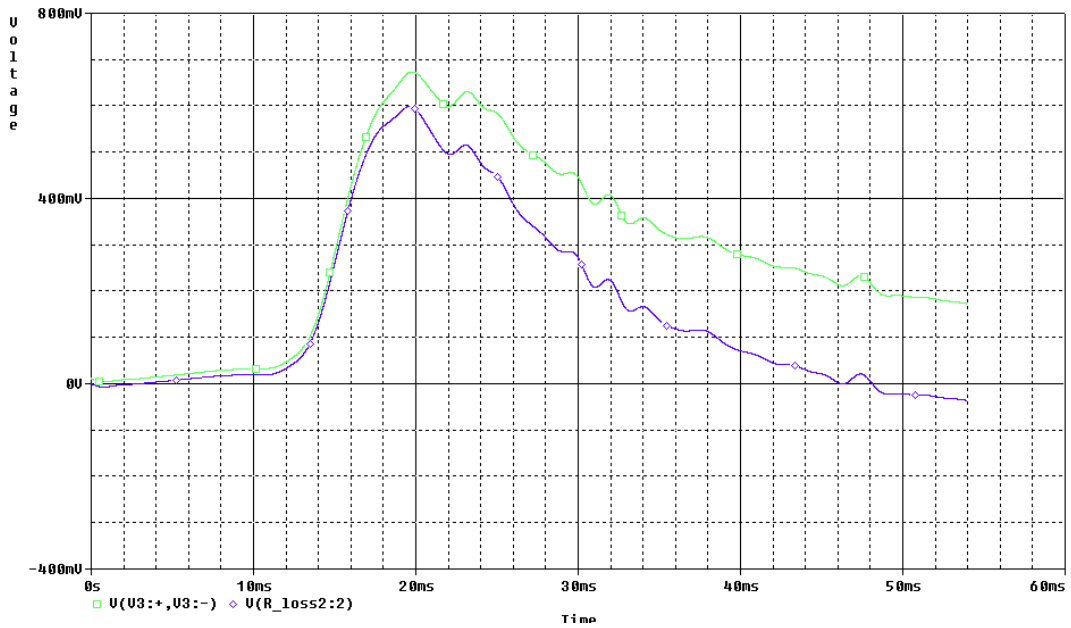
Figure 5.39 The Output Voltage Change after Modification

This change is related with time constant, τ is the time required to charge the capacitor, through the resistor, to 63 % of full charge; or to discharge it to 37 % of its initial voltage.

τ is determined by the product of the capacitance and the resistance of the system as in

$$\tau = RC .$$ (5. 4)

The ratio of output voltage to input voltage depends on

$$\frac{V_o}{V_{in}} = \frac{2\pi f \tau}{\sqrt{1 + (2\pi f \tau)^2}} ,$$ (5. 5)

where f is the frequency of voltage signal [39]. When the equations and the voltage signal is investigated, τ drops because of the data collection cable resistance. Since the frequency content also drops in the decay region of the voltage signal the ratio in Eqn. 5.3 also drops and results in the drop in output voltage.

After simulating the piezoelectric energy harvester system together with data collection cable, the results are exported to compare with voltage measurements. In Figure 5.40, the produced and calculated voltage characteristic is almost the same and the error is smaller than 6.5 % for maximum value. The reason for this small error could be the small difference in piezoelectric constant, additional mass effect of protection apparatus etc. As it can be seen, considering the charge created by the upper layers' mass is not so efficient since the total thickness of piezoelectric stack is only 2 mm.

In the design of piezoelectric energy harvesters for gunfire applications, the compression stress created in piezoelectric element and its strength is an important factor. The compression strength of piezoelectric elements is on the order of 250 MPa [21]. However, they are very sensitive to tensile stresses which can lead to depolarization and failure. In pressure gun test stand during the launch, the acceleration profile in Figure 5.32 is mainly in one direction which forces compression mass in compression direction like real gunfire applications.
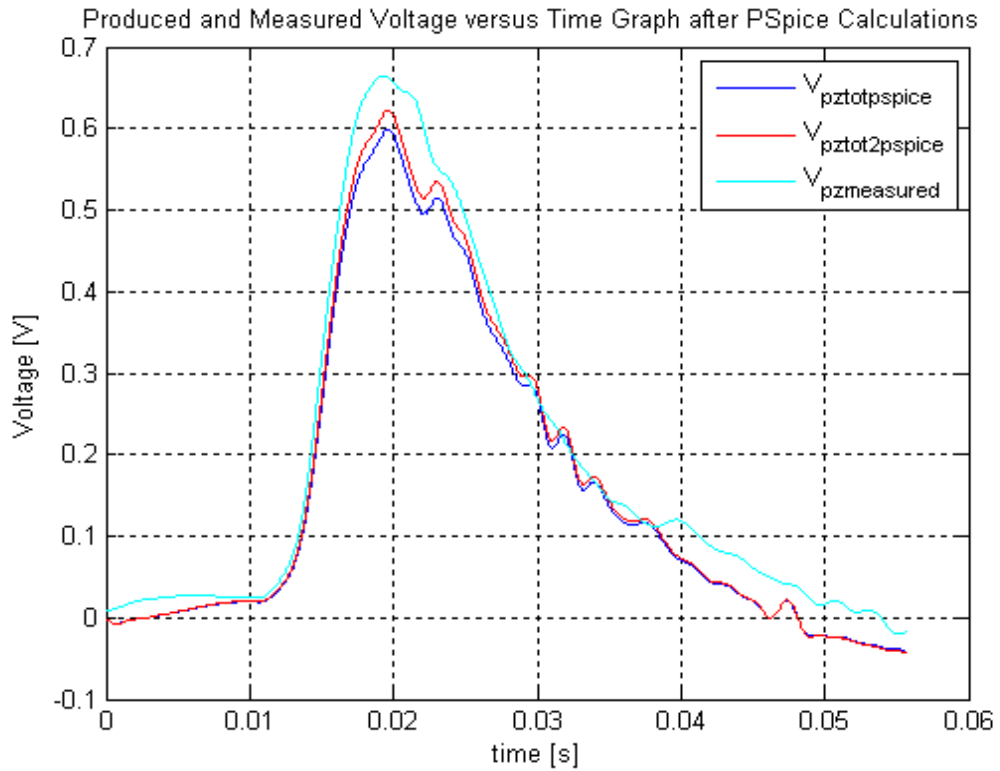
Figure 5.40 Calculated and Measured Voltage Comparison after ORCAD PSPICE[®] Calculations

The compression force created in piezoelectric element because of tightening torque, F_m, which is equal to axial force created in bolt since there is no external axial loading in the bolt calculated as

$$F_m = \frac{-T}{Kd},$$ (5. 6)

where K is torque coefficient which can be taken as 0.20 not depending on the size and the thread conditions of the bolt and d is bolt diameter [41].

The compression force due to tightening is calculated as 2000 Newtons. The resulting compression stress is calculated as 23.5 MPa by

$$\sigma_{tightening} = \frac{F_m}{A_{pz}},$$ (5. 7)

where A_{pz} is piezoelectric cross section area.

The compression stress due to launch acceleration, σ_{comp} is calculated as

$$\sigma_{comp} = \frac{F_{comp}}{A_{pz}},$$ (5. 8)

where F_{comp} is compression force due to acceleration during launch.

The compression stress can also be calculated by the response of piezoelectric element by lumped parameter modelling as described before.

The compression stress in launch duration is calculated as in Figure 5.41. The graph with blue colour is the compression stress calculated by above equations and the graph with red colour is the one calculated by lumped parameter model response. Because of the frequency content of acceleration, they are almost same and about 0.3 MPa at maximum for this case. Total compression stress created in piezoelectric stack is as in Figure 5.42 which is about 23.9 MPa much smaller than compression stress limitations of piezoelectric materials.
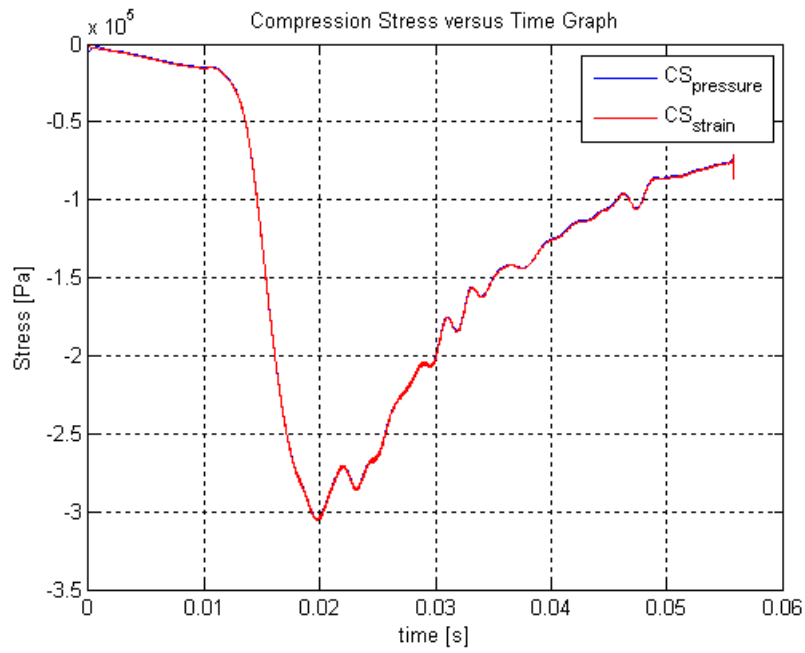
Figure 5.41 Compression Stress on CMAR03 due to Launch
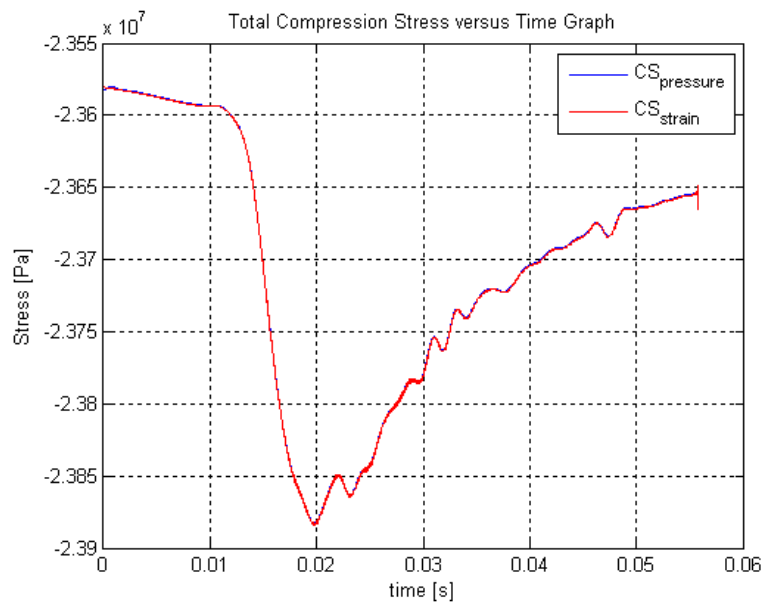
Figure 5.42 Total Compression Stress on CMAR03

The finite element analysis is also applied in pressure gun test results. Multilayer piezoelectric stack is modelled by the geometrical properties provided by Noliac Company. The piezoelectric stack is modelled as one layer having the same capacitance and charge producing capability. The piezoelectric material contains 25 layers with 67 microns thickness each having a total thickness of 1.675 millimetres. 75 % surface area of piezoelectric material covered by electrodes and polarized and the remaining part is non-polarized which means it has no charge producing capability. The electrodes having 2 microns thickness made of platinum are not modelled since they are very thin. The internal structure of piezoelectric material is modelled as in Figure 5.43.

Total thickness of piezoelectric stack is 2 millimetres. The remaining thickness of the piezoelectric stack is added as non-polarized piezoelectric material to lower and upper surfaces of the structure in Figure 5.43 with 162.5 microns thickness each as in Figure 5.44. Steel compression mass is added to upper surface of CMAR03 having the same weight in the tests as in Figure 5.45.
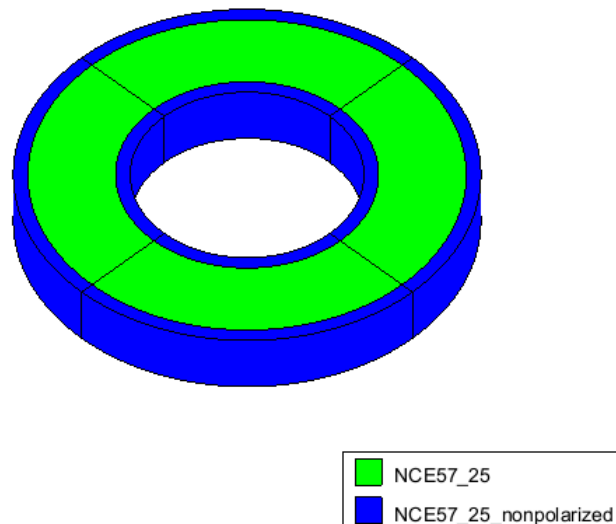
Figure 5.43 The Internal Structure of CMAR03 Piezoelectric Stack
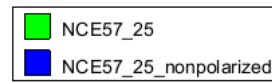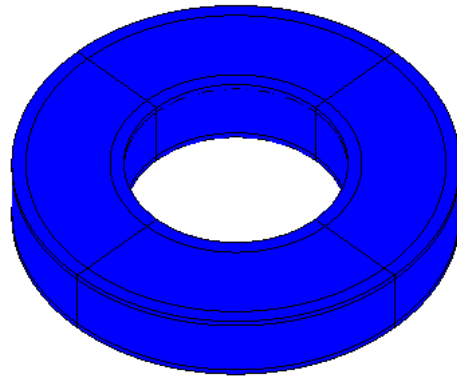
Figure 5.44 The Structure of CMAR03 Material
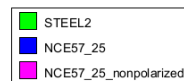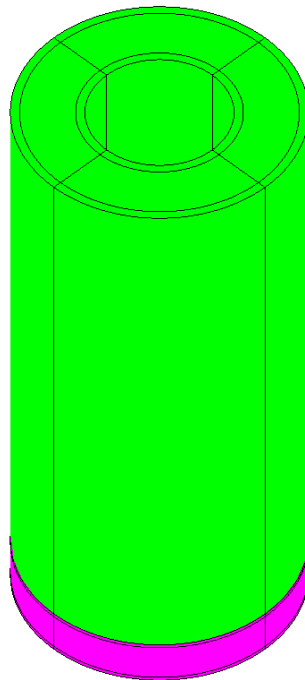
Figure 5.45 The Structure of CMAR03 Energy Harvester

The piezoelectric material, NCE 57 properties are entered as in Appendix D. To have the same capacitance with CMAR03 by modelling in one layer, relative dielectric constant of the material, ε_r is multiplied by the square of number of layers, 625 in polarization direction. To have the same charge producing capability, the piezoelectric constant, d_{33} is multiplied by number of layers, 25. For non-polarized condition of the piezoelectric material, the piezoelectric constants are taken to be zero to have no charge producing capability.

The electric potential conditions of electrodes of piezoelectric material are defined as in Figure 5.46. The upper surface of piezoelectric material is grounded and the lower surface of piezoelectric material is in floating boundary condition.

The polarization condition of the structure is entered in positive z direction, 3rd direction in Figure 2.1, as in Figure 5.47. If the multilayer structure was modelled with 25 layers, it would contain positive and negative polarization directions changing in each following layer.
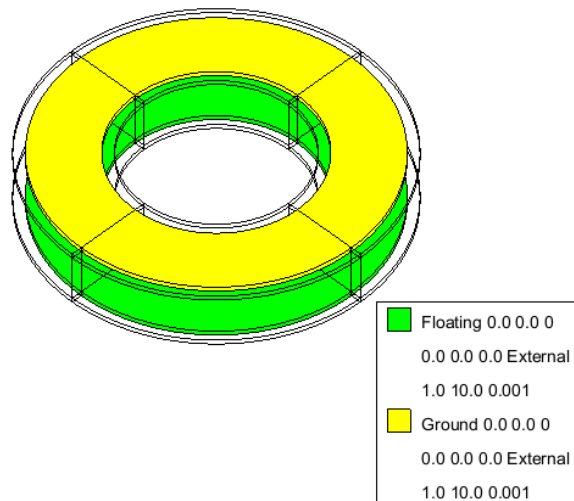
Figure 5.46 Surface Electric Potential Conditions
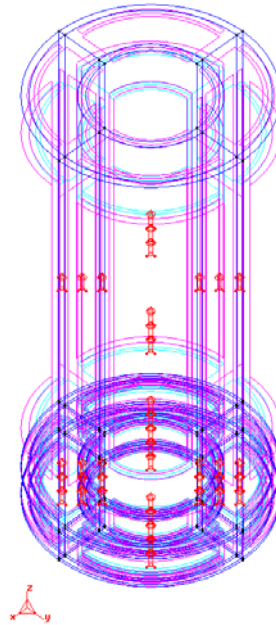
Figure 5.47 Polarization Conditions of Materials

In ATILA® transient analysis module, the acceleration is not allowed to define directly. To load the structure varying with time, a Microsoft Excel sheet as in Appendix D is created in which the first column is time, the second column is displacement and the third and fourth columns are velocity and acceleration which are first and second derivatives of displacement, respectively. Then, this file is saved in ".html" format and copied to "project.exc" file created in analysis folder. To make this file being recognized by ATILA®, a constant displacement input, i.e. 1 mm, is applied to bottom surface of CMAR03 as in Figure 5.48.

Applying all boundary conditions, the finite element model of the piezoelectric energy harvester is created as in Figure 5.16 with 1080 HEXA20P piezoelectric elements having 5376 nodes.

Transient analysis settings are defined as in Figure 5.50 in which Wilson-θ Method and related parameters are defined [45].
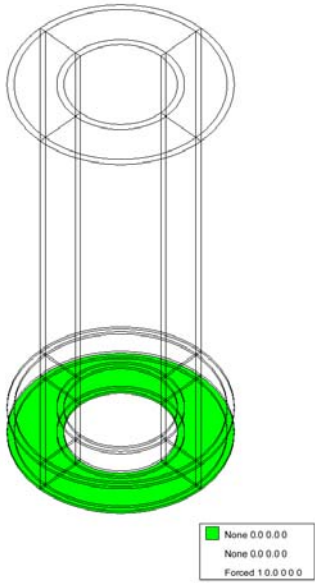
Figure 5.48 Displacement Definition in ATILA®
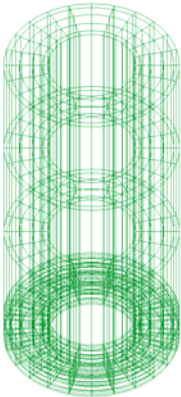
Figure 5.49 Finite Element Model of CMAR03 and Compression Mass
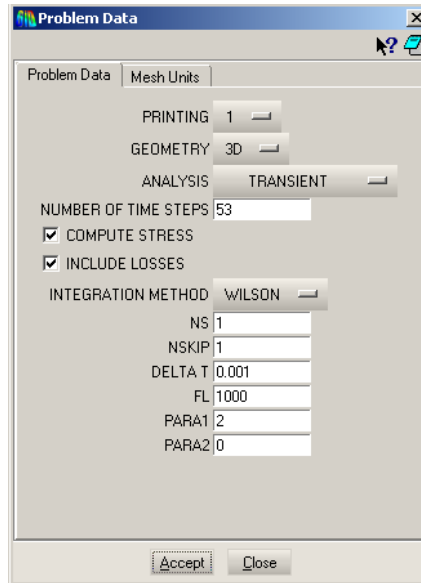
Figure 5.50 Transient Analysis Settings

To make the analysis, "ati" file is created and the defined displacement input is made "0" as in to use "project.exc" file defined before as in Appendix D.

Since the time step limit of ATILA® is 1000 steps, the collected acceleration data which is collected at 100 kHz sampling frequency is resampled. When the acceleration data is resampled at 10 kHz frequency by nCode Glyphworks®, almost the same acceleration signal is observed as in Figure 5.51 in which the graph with red colour is original data and the other one is resampled data.

When the voltage output in a node in which floating electrical boundary condition is applied is observed, the result contains meaningless spikes as in Figure 5.52.

When the reason is investigated, it is determined to be the frequency of acceleration data. When the data is resampled at 1 kHz, instead, the concluded acceleration is deviated in some regions which are not very important as in Figure 5.53.

Marker	Axis	Title	Y Max	Y Min	Y Mean	Y Units
	A	piezo_test6_...	1601	9.027	669	m/s^2
	A	piezo_test6_...	1601	9.027	669.4	m/s^2
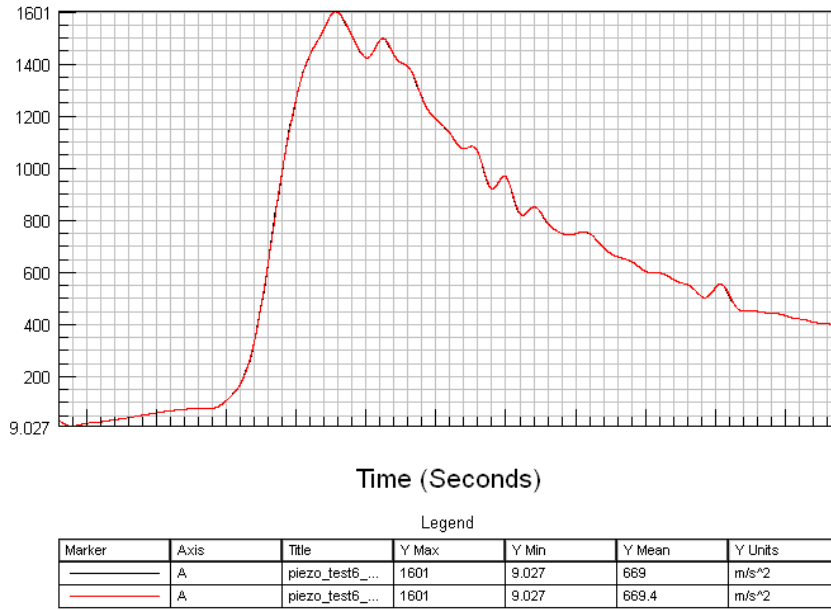
Figure 5.51 Comparison of Original Acceleration Data with Resampled Data at 10 kHz
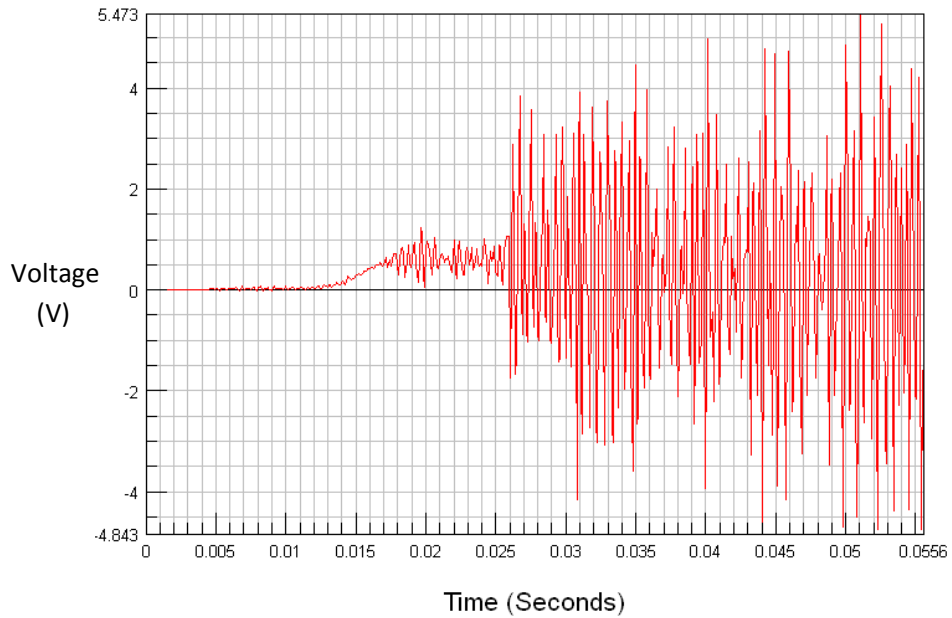
Figure 5.52 Voltage Output with Spikes

The resulted voltage output graph is as in Figure 5.54 which does not contain spikes. The resulted voltage distribution graph when the maximum voltage output is produced is as in Figure 5.55.

To compare the finite element analysis results with the measurement, the voltage output of ATILA® is imported to ORCAD PSPICE® model in Figure 5.38. The resulted output voltage of analysis and the measurement is as in Figure 5.57.

Marker	Axis	Title	Y Max	Y Min	Y Mean	Y Units
———	A	piezo_test6_...	1596	10	665.2	m/s^2
———	A	piezo_test6_...	1601	9.027	669.4	m/s^2
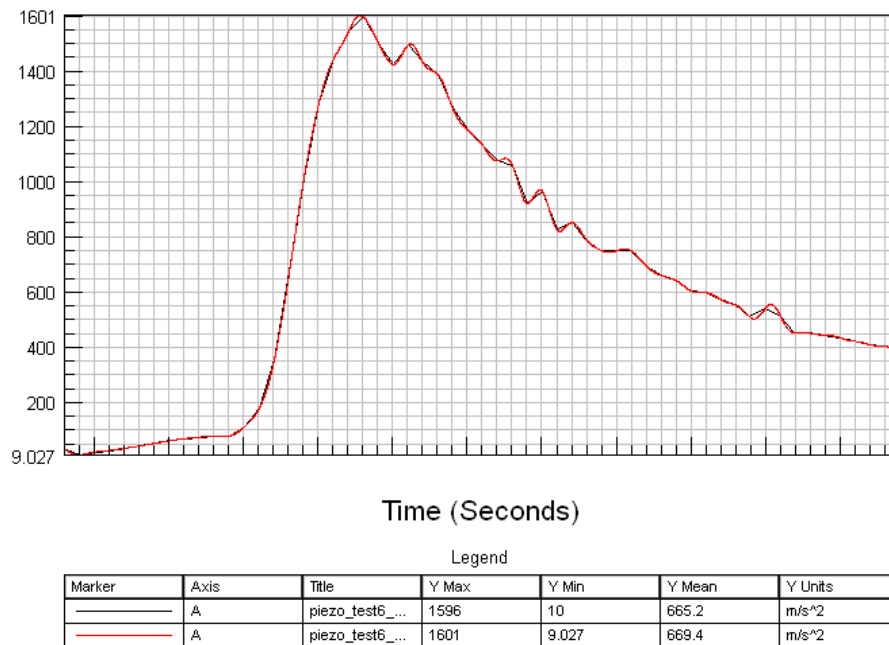
Figure 5.53 Comparison of Original Acceleration Data with Resampled Data at 1 kHz
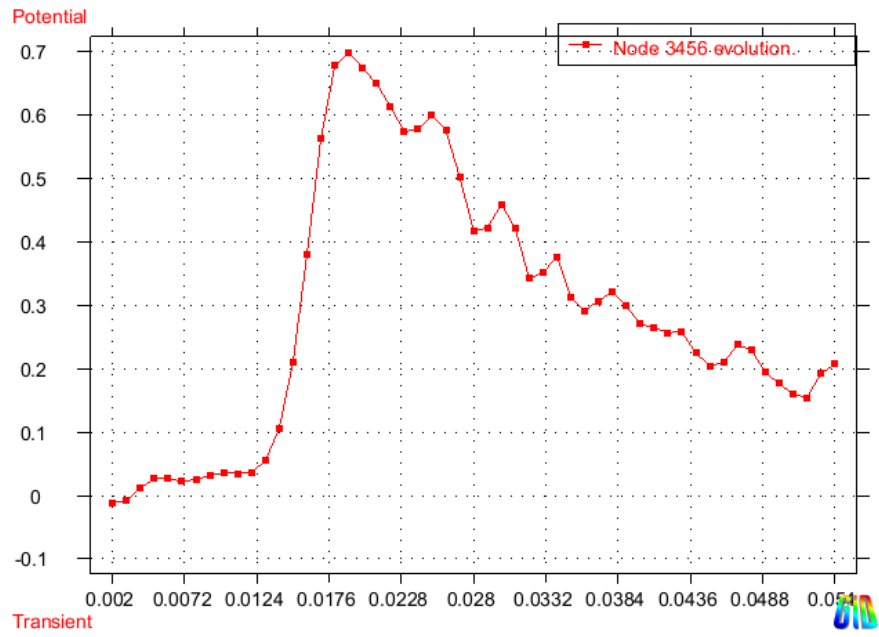
Figure 5.54 Voltage Output Graph of the CMAR03
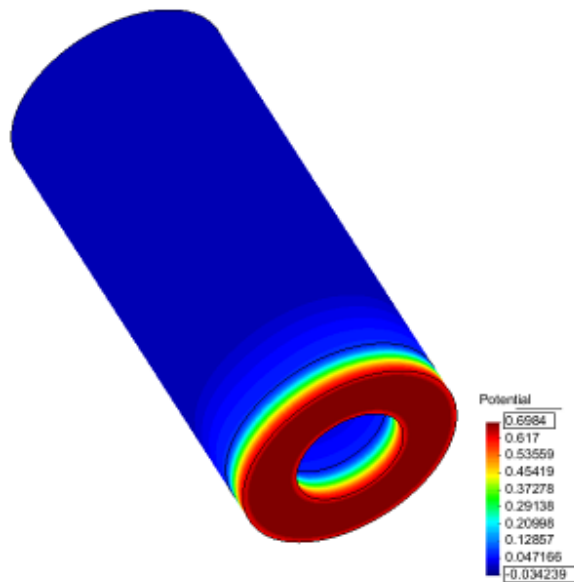
Figure 5.55 Voltage Output Distribution of CMAR03 Piezoelectric Energy Harvester
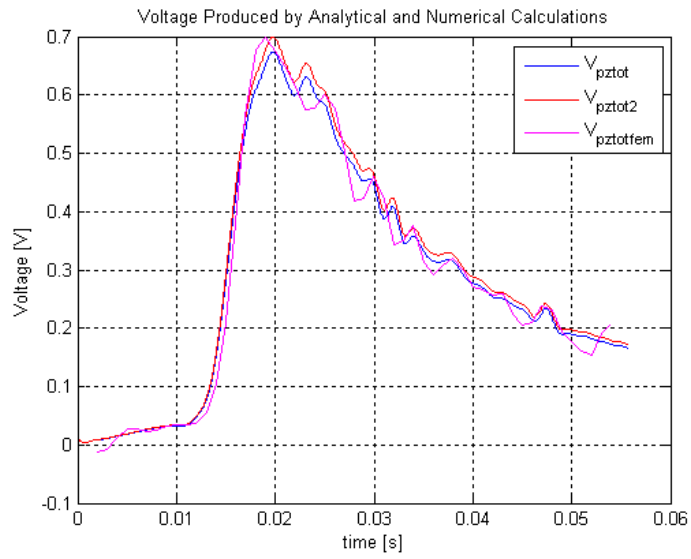
Figure 5.56 Comparison of Voltage Outputs Obtained by Analytical Methods and ATILA®
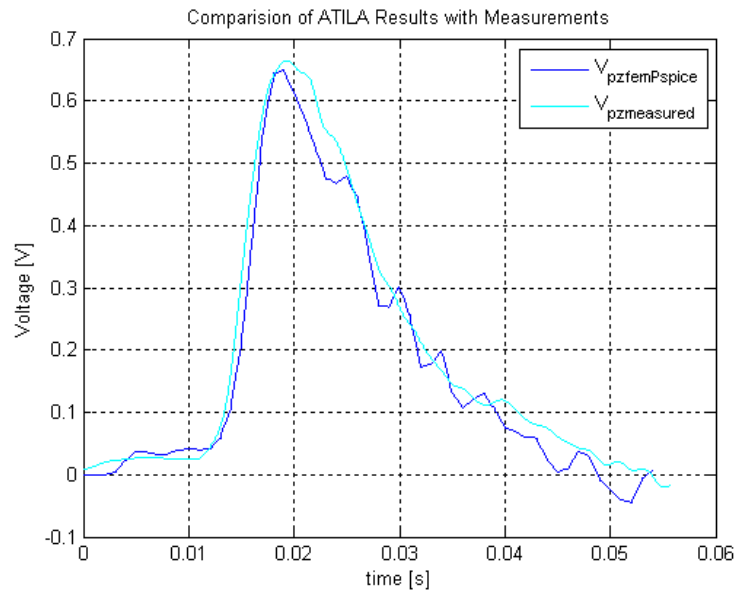
Figure 5.57 Comparison of Voltage Output of ATILA® and the Measurement

5.3.2.2. CMAR04 Test Results

The acceleration profile applied by pressure gun in the launch duration is as in Figure 5.58. The compression mass is 22.9 grams including washer and bolt head weights. The compression force exerted on piezoelectric element is as in Figure 5.33.

The capacitance of piezoelectric element is calculated as 504 nF by applying an area factor of 0.75 since the electrodes cover approximately 75 % of piezoelectric element which is indicated by Noliac Company. The capacitance is measured as 469 nF by a multimeter as in Appendix C. This difference is because of uncertainties of the piezoelectric element.
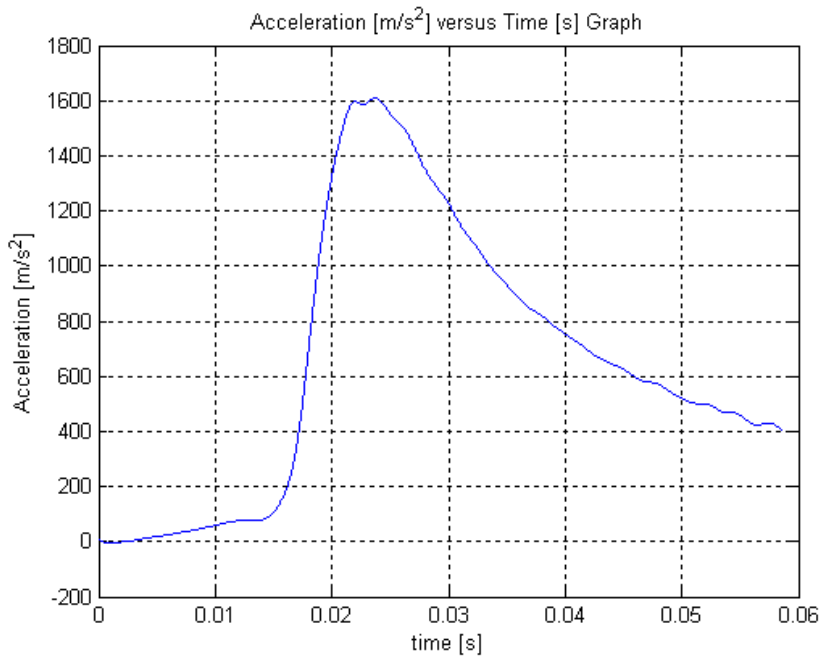
Figure 5.58 The Acceleration Applied on CMAR04 Piezoelectric Energy Harvester System
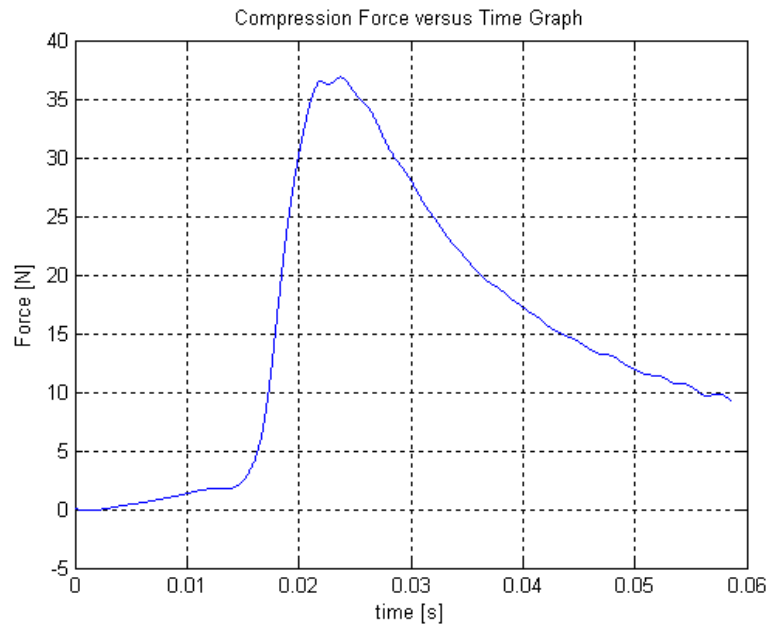
Figure 5.59 The Force Exerted on CMAR03 Piezoelectric Material

To attach the piezoelectric energy harvester system to the test stand, a M5 bolt is used with 2 Nm tightening torque. The capacitance of piezoelectric stack increases to 490 nF as in Appendix C. The measured capacitance value after tightening is used not to have the calculation error related with this difference.

The natural frequency of piezoelectric material with compression mass is calculated as 51528 Hz. The calculated and measured voltage graphs are as in Figure 5.60. The graph in dark blue colour is the voltage calculated by force not considering the charge difference in layers while the graph in red colour is created by considering this difference. The graph in black colour is the voltage calculated by lumped parameter modelling and mechanical stress which is almost the same with the dark blue one. The reason behind is the loading condition is quasi-static condition with a frequency content much lower than the first natural frequency of piezoelectric energy harvester in compression mode. Because they are the same, only the output voltage

with dark blue colour is used in ORCAD PSPICE® calculations. The graph in light blue colour is measured piezoelectric output voltage.

The loss resistance is calculated as 269 ohm by finding the main frequency of loading as 20.5 Hz taking the frequency spectrum of acceleration data in Figure 5.32 as in Figure 5.61.

The leakage resistance is calculated as 10.9942 mega-ohms by an input voltage of 5.004 volts and measuring the output voltage as 3.845 volts while by a 3.314 mega-ohms resistance in the related previously described test procedure. The resulted ORCAD PSPICE® circuit scheme is as in Figure 5.36 by including data collection cable resistance. The resulted output voltage with red colour changed its shape as in Figure 5.63.

After simulating the piezoelectric energy harvester the results are exported to compare with voltage measurements. In Figure 5.64, the produced and calculated voltage characteristics are in very good agreement.

The compression force due to tightening is calculated as 2000 Newtons. The resulting compression stress is calculated as 17.7 MPa.

The compression stress in launch duration is calculated as in Figure 5.65. The graph with blue colour is the compression stress calculated by Eqn. 5.6 and the graph with red colour is the one calculated by lumped parameter model response. Because of the frequency content of acceleration, they are almost same and about 0.33 MPa at maximum for this case.
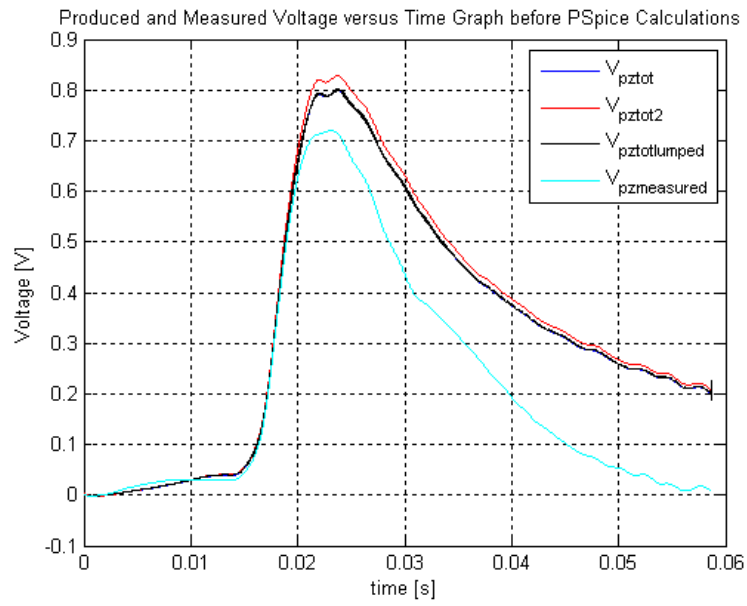
Figure 5.60 Calculated and Measured Voltage Comparison before ORCAD PSPICE[®]
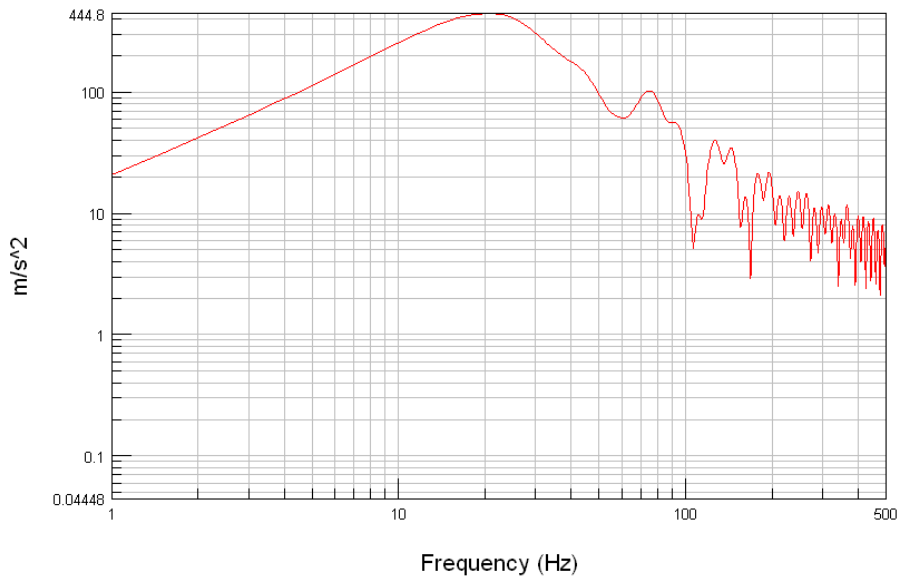
Calculations

Figure 5.61 Frequency Spectrum of Acceleration Data
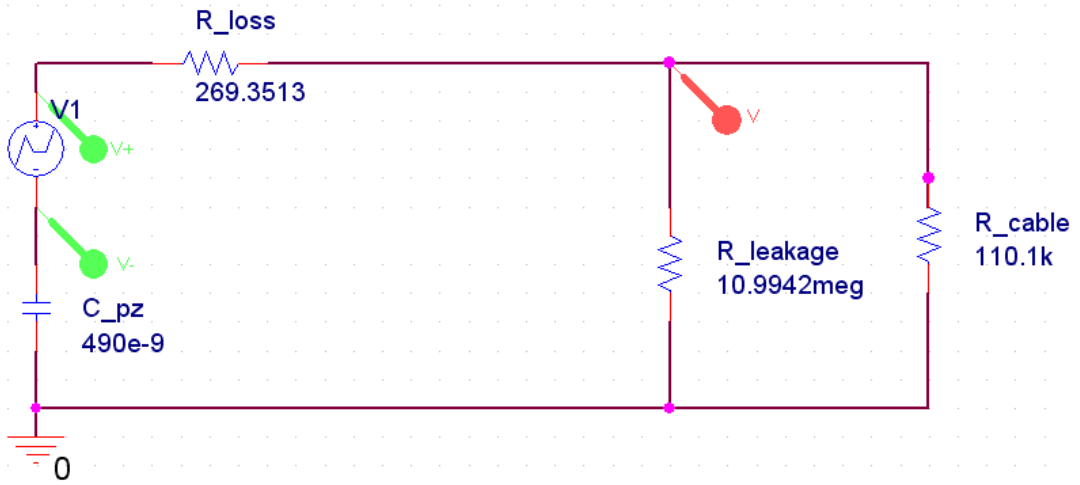
Figure 5.62 CMAR04 connected with 4865-01 Cable in ORCAD PSPICE®
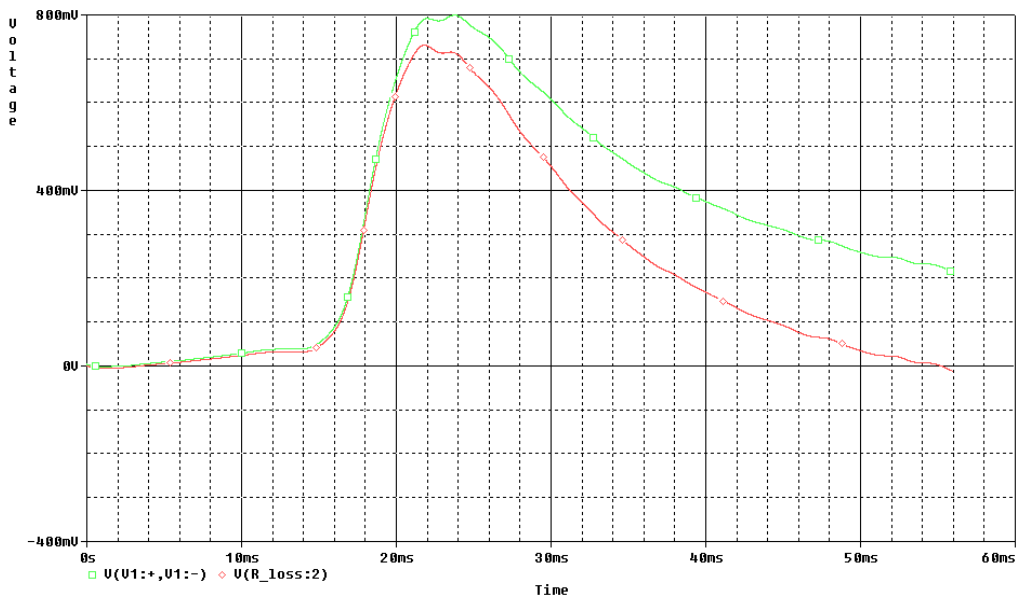
Figure 5.63 The Output Voltage Change After Modification
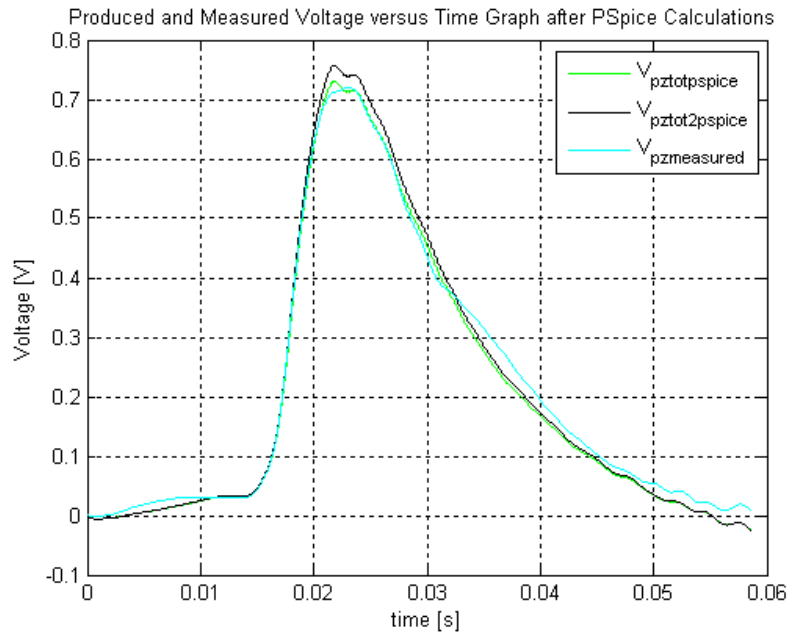
Figure 5.64 Calculated and Measured Voltage Comparison after ORCAD PSPICE[®] Calculations
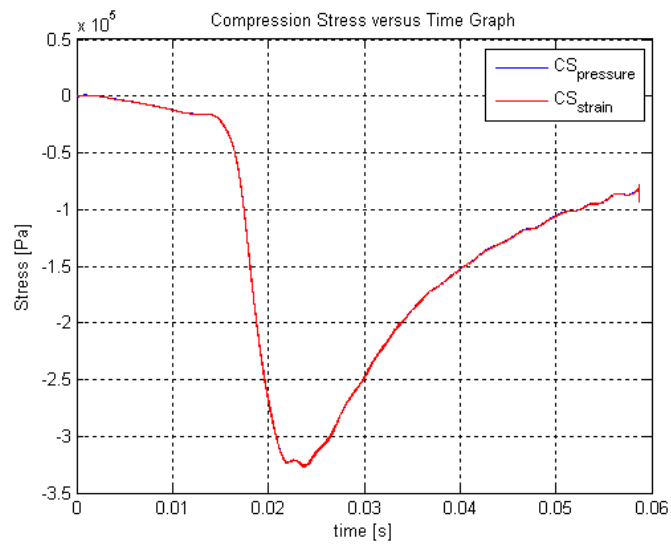
Figure 5.65 Compression Stress on CMAR04 on Launch

The finite element analysis is applied also for CMAR04 pressure gun tests. Since the main difference between CMAR04 and CMAR03 for which the modelling is described in detail above is the outer and inner diameters of materials, the details of finite element model of CMAR04 energy harvester is not discussed. The acceleration data is resampled again at 1 kHz not to deal spikes mentioned before. The comparison of the original data with resampled data is as in Figure 5.66. The resulted voltage output graph is as in Figure 5.67. The resulted voltage distribution graph when the maximum voltage output is produced is as in Figure 5.72.

The comparison of voltage output obtained by analytical methods and ATILA$^®$ is as in Figure 5.69 which results in similar values. To compare the finite element analysis results with the measurement, the voltage output of ATILA$^®$ is imported to ORCAD PSPICE$^®$ model in Figure 5.62. The resulted output voltage of analysis and the measurement is as in Figure 5.70. The results are deviated in some duration, since it is necessary to resample the loading condition and the piezoelectric stack has some imperfections which results in different capacitance etc.

Marker	Axis	Title	Y Max	Y Min	Y Mean	Y Units
	A	piezo_test3_UNFILTERED_in1 Ch 2 ...	1608	-4.757	645.7	m/s^2
	A	piezo_test3_UNFILTERED_in2 Ch 2 ...	1611	-4.781	650.3	m/s^2
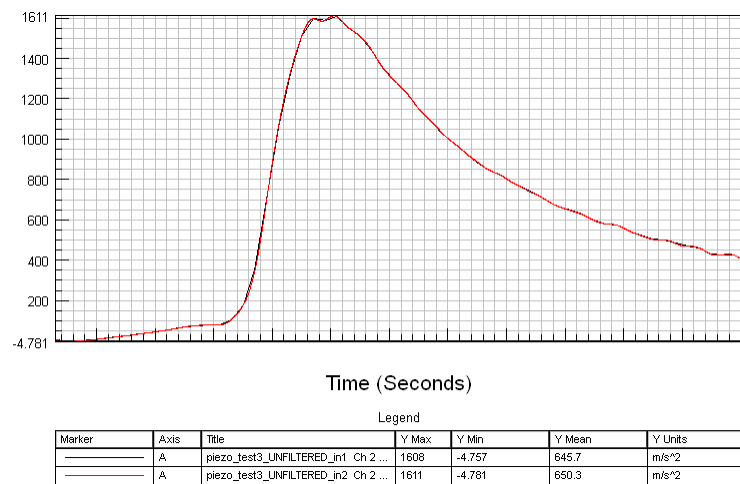
Figure 5.66 Comparison of Original Acceleration Data with Resampled Data at 1 kHz
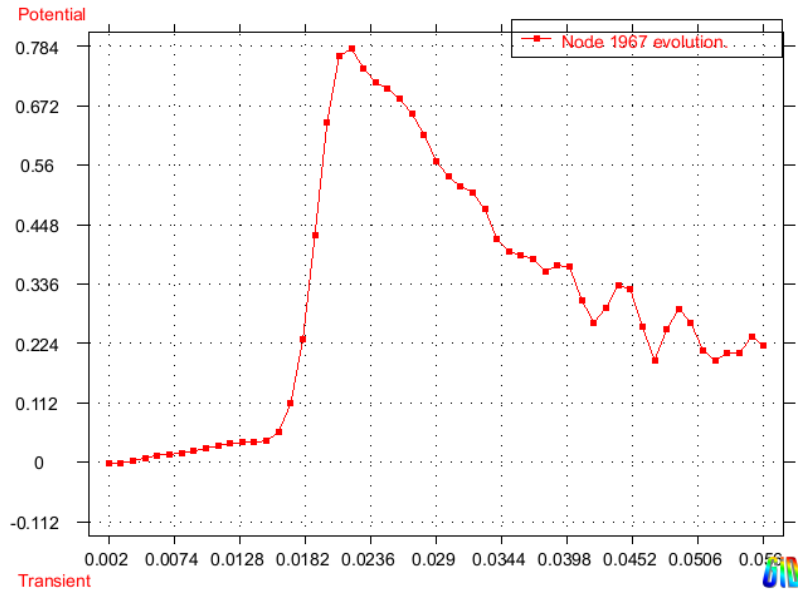
Figure 5.67 Voltage Output Graph of CMAR04
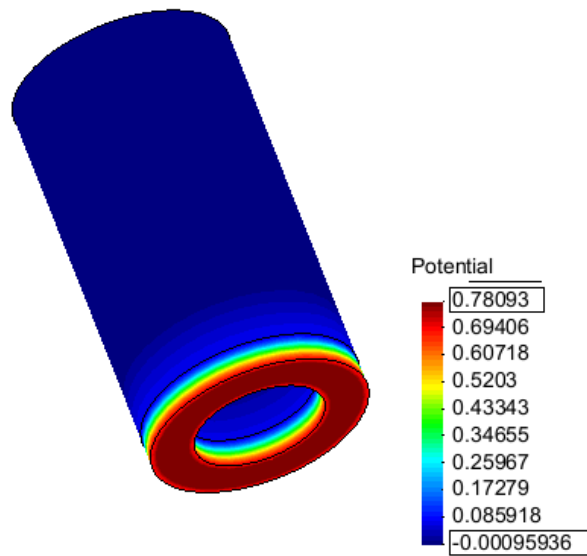
Figure 5.68 Voltage Output Distribution of CMAR04 Piezoelectric Energy Harvester
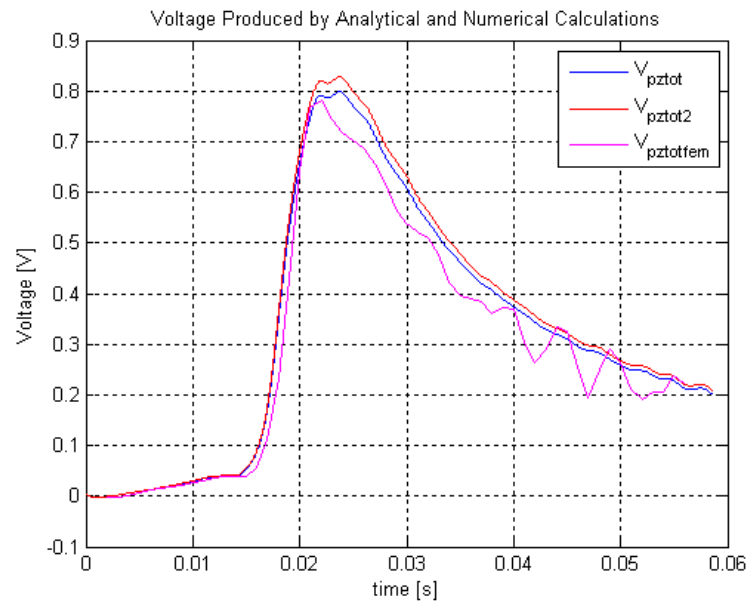
Figure 5.69 Comparison of Voltage Outputs Obtained by Analytical Methods and ATILA®
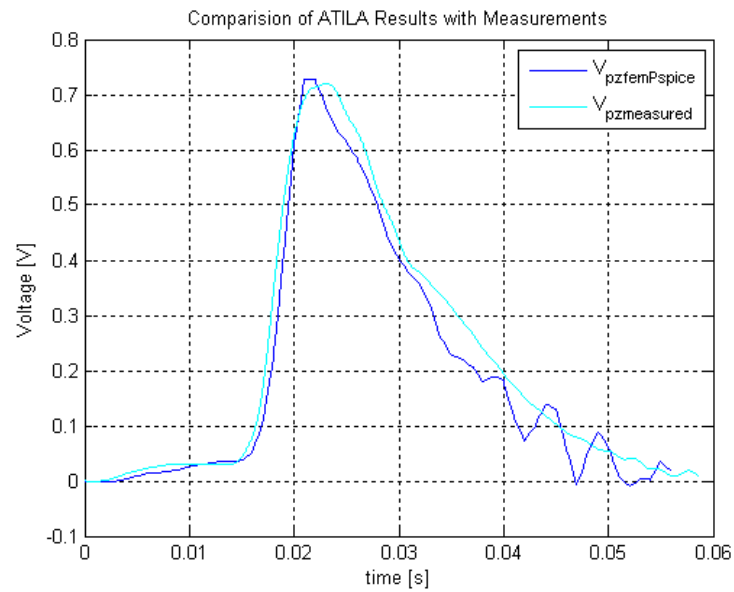
Figure 5.70 Comparison of Voltage Output of ATILA® and the Measurement

5.4.   Energy Optimization of Piezoelectric Energy Harvesters

In the design of piezoelectric energy harvesters, harvested electrical energy should be stored in a proper capacitor to be used by electrical elements of the required systems. To charge this energy at maximum level, the impedance matching which is mentioned before is an important concept.

The pressure gun test results for CMAR04 material is used to show the effect of connected stored capacitance in the energy levels. The storage capacitance is connected to CMAR04 material by ignoring the data collection cable resistance as in Figure 5.71.

The voltage created on the storage capacitor when the capacitor is 100 nF is as in Figure 5.72 in red colours. The capacitor is charged to 0.271 Volts corresponding to 3.67×10^{-9} Joules.

This analysis is done for different capacitance values. The resulted energy storage change with capacitance is as in Figure 5.73. The maximum energy is harvested when the storage capacitance is 400 nF which results in matched impedance for the piezoelectric energy harvester model and near to piezoelectric capacitance, 490 nF. The energy levels decreases sharply when the capacitors with lower capacitance than 300 nF and higher capacitance than 500 nF and almost the same 350-500 nF range.
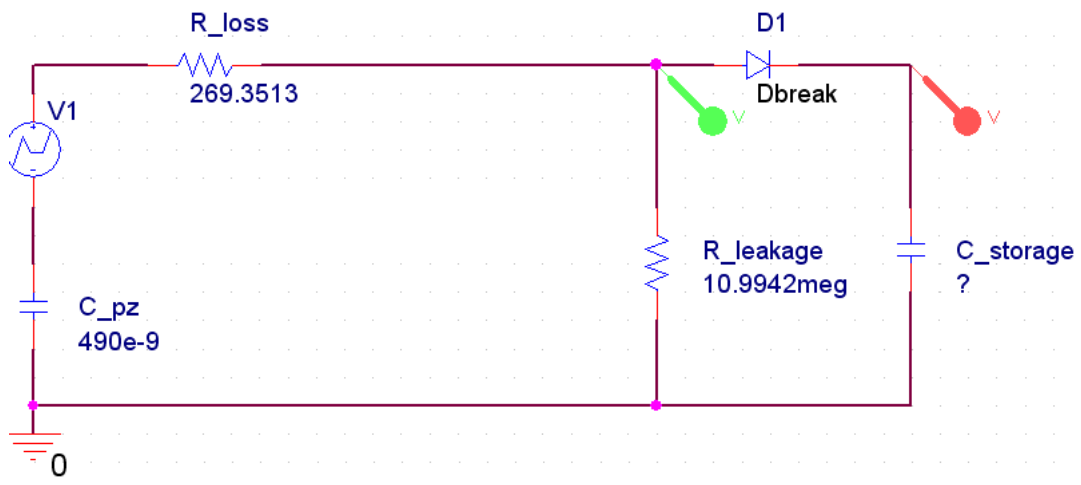
Figure 5.71 Piezoelectric Energy Harvester Model with Storage Capacitor
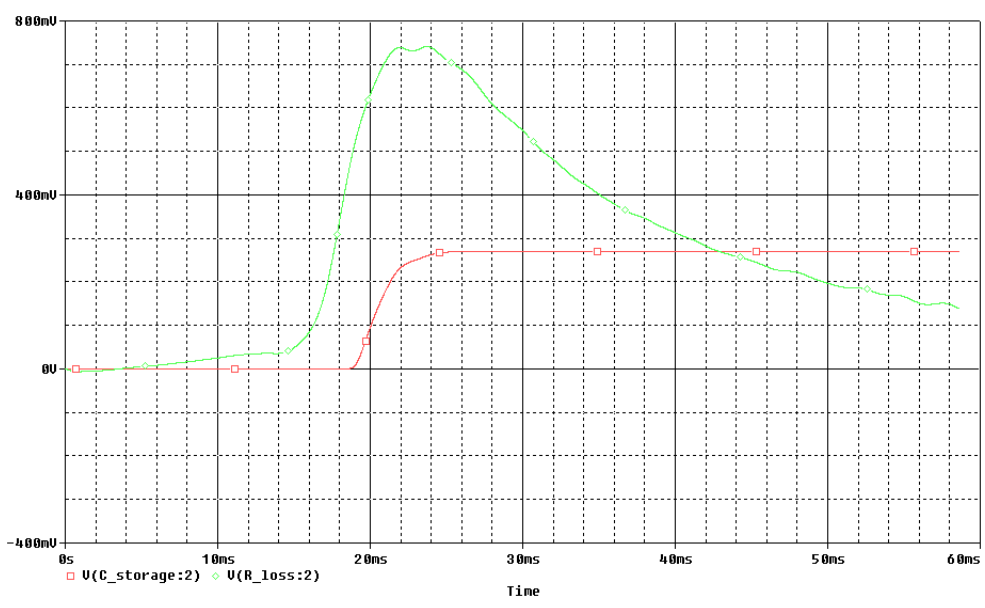
Figure 5.72 The Voltage Created on Storage Capacitor
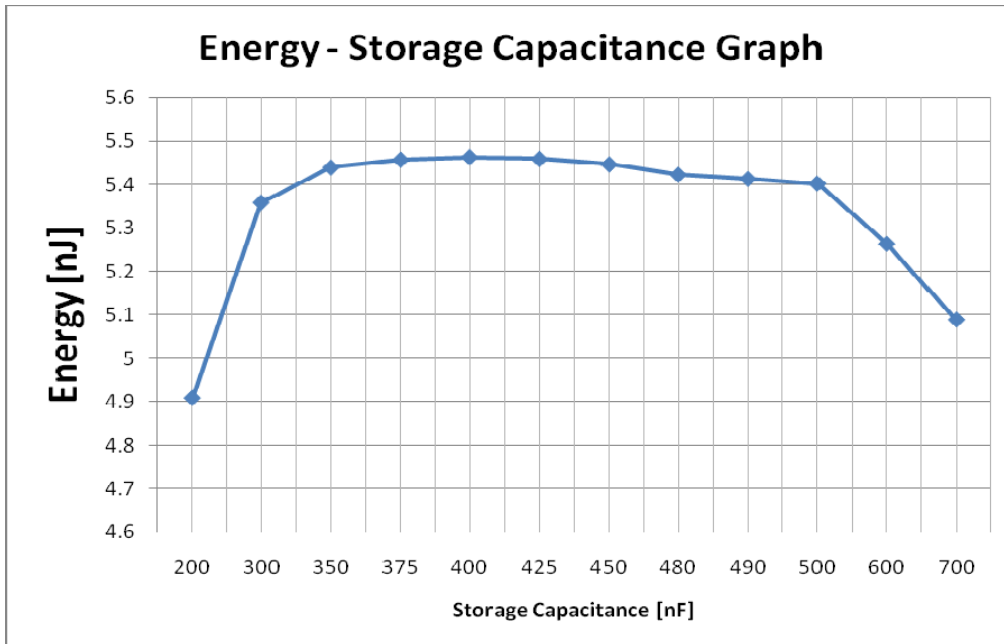
Figure 5.73 Energy Change with Storage Capacitance

CHAPTER 6

DISCUSSIONS AND CONCLUSIONS

In this thesis, it is aimed to apply the piezoelectric elements technology to develop means for energy storage in munitions launch. The practical problems encountered in the design of piezoelectric energy harvesters are investigated. The applicability of energy harvesting to high power needs are studied. The experience compiled in the study is to be exploited in designing piezoelectric energy harvesters for munitions applications.

In the first chapter, detailed information about piezoelectricity history, piezoelectric material types, physical phenomenon of piezoelectric materials, typical applications of piezoelectric materials is investigated. Information about piezoelectric material properties, polarization of piezoelectric materials, modelling of piezoelectric behaviour, common shapes and loading conditions of piezoelectric materials and literature survey is studied in the second chapter. Then, analytical and numerical approaches to obtain the electro-mechanical parameters of piezoelectric materials are proposed in the third chapter while the experimental test setups used to verify these mathematical models is given in the fourth chapter. In the fifth chapter, the results obtained from the experiments and their comparisons with mathematical models are discussed.

Firstly, the experimental setup is designed for a single layer piezoelectric material by a modal shaker to test it in a controlled acceleration environment, harmonic loading.

By conducting these tests, the knowledge about measuring the accelerometer and piezoelectric output voltage data, analyzing the problem with analytical and finite element methods is gained.

The tests are then conducted in high-g shock environments with multilayer piezoelectric materials. Multilayer piezoelectric materials usage is a must in munitions energy applications since the acceleration level is very high. In this level of loading, single layer piezoelectric materials result in producing output voltages in kilovolts range which is not possible to control. In recognition of this problem, some samples of multilayer piezoelectric elements from Noliac Company are acquired. In the literature, there is only one study with similar materials having layer thicknesses in micrometers range by Pearson [4]. However, he conducted the tests with a commercial product by Omnitek Company, which is a piezoelectric energy harvester with resonator. He used some correction factors according to the results of the experiments and calculations for each resonator because he had to rely on the information supplied by Omnitek engineers. In order to avoid such problems, in this study, the energy harvesters are designed by the compression mass. Firstly, mechanical loading test is conducted in the impact hammer test setup. Because of the zero shift effects, tensile loadings and different characteristics of acceleration in shock plate etc., the experimental test results are not harmonious enough with analysis results. These factors are not valid for munitions applications. To conduct the tests in a loading condition having similar acceleration environment with munitions applications, pressure gun test setup is adopted. The experimental test results in this test setup is harmonious with the analytical models developed in MATLAB$^®$ and finite element models developed in ATILA$^®$ by together with ORCAD PSPICE$^®$.

Storage of the harvested electrical energy is very important concern since by inconvenient capacitors the harvested energy levels can be reduced drastically. Impact of impedance matching phenomenon is demonstrated and underlined by test results and electrical analysis in ORCAD PSPICE$^®$.

Design of piezoelectric energy harvesters not requiring electrical converters to reduce the voltage levels according to space limitations and electrical energy and voltage requirements is exercised. According to the literature, piezoelectric energy harvesters in munitions application can be designed for high g environments up to 120.000 g [16] . For small-calibre fuses, for instance, electrical energy requirement is about 3 mJ [17]. In order to compare, during CMAR04 pressure gun tests the developed acceleration is about 164 g which results in 5.4 nJ electrical energy in the storage capacitance. Extrapolating the acceleration level to 120000 g by assuming linearity, the corresponding stored energy could increase up to 2.9 mJ which proves the feasibility of piezoelectric energy harvesters for supplying the energy requirement of munitions. Obviously, increasing the compression mass, designing mechanical resonators, by bigger size piezoelectric materials and fine tuning material parameters can increase the harvested energy levels.

In a future work, application of these energy harvesters for smart munitions can be realized. The energy harvesting capability due to spin of munitions and flight vibrations can also be investigated in future extensions of this study. Resonators can be designed to increase the force applied on piezoelectric materials. Their design parameters can be investigated to exercise the adoptability of resonators for a known gunfire acceleration environment. Non-linear effects can be introduced to mathematical models during launch of munitions with accelerations of thousands of g's. Production techniques of multilayer piezoelectric elements can also be investigated.

REFERENCES

[1]   S.P. Beeby, M.J. Tudor, N.M. White, 2006, "Energy Harvesting Vibration Sources For Microsystems Applications", Meas. Sci. Technol. 17 R175-R195.

[2]   A. Ertürk, 2009, "Electromechanical Modelling of Piezoelectric Energy Harvesters", Ph. D. thesis, Virginia Polytechnic Institute and State University, Blacksburg, VA.

[3]   G. Gautschi, 2002, "Piezoelectric Sensorics: Force, Strain, Pressure, Acceleration and Acoustic Emission Sensors, Materials and Amplifiers", Springer, New York.

[4]   S. R. Pearson, 2006, "Modelling and Development of Piezoceramic Energy Harvester for Munitions Applications" , Msc. Thesis, Villanova University.

[5]   M. Havranek, 2009, "Sensors & Transducers Noliac Piezo Technology Course", Noliac Course Notes.

[6]   J. Curie, P. Curie, 1880, "C. R. Academy of the Sciences 91 (1880) 294." Bull.soc.min.de France 3.

[7]   Piezo Systems Inc., Last accessed, May 22, 2011, http://www.piezo.com

[8]   APC International Ltd., Last accessed June 21, 2011, http://www.americanpiezo.com/piezo_theory/piezo_theory.pdf

[9]   Noliac Systems, Last accessed June 21, 2011, http://www.noliac.com/Application_overview-7795.aspx

[10]   Powerleap Inc., Last accessed January 1, 2011, http://www.powerleap.net/images/product.html

[11]   E. Bianchini and R. L. Spangler, 1998, "Use of piezoelectric devices to control snowboard vibrations" Proc. SPIE, Vol. 3329, 106.

[12]   U.S. Department of Transportation, Last accessed March 27, 2011, http://phmsa.dot.gov/hazmat

[13]   International Civil Aviation Organization, Last accessed March 27, 2011, http://www.icao.int/anb/fls/dangerousgoods/TechnicalInstructions

[14]   European Agreement Concerning the International Carriage of Dangerous Goods by Road, Last accessed March 27, 2011, http://www.unece.org/trans/danger/publi/adr/ADRagree_e.pdf

[15]   IATA, Last accessed March 27, 2011, http://www.iata.org/whatwedo/cargo/dangerous_goods/Pages/lithium_batteries.aspx

[16]   J. Rastegar, R. Murray, C. Pereira and H-L. Nguyen, 2009, "Event Sensing and Energy-Harvesting Power Sources for Gun-Fired Munitions" Proc. of SPIE Vol. 7288 72880Z-1.

[17]   S. Yoon, J. Oh, Y. Lee, S. Lee, 2005, "Miniaturized Inertia Generators as Power Supplies for Small-Caliber Fuzes" IEEE Transaction on Magnetics, Vol. 41, No. 7.

[18]   M. Havranek, 2006, "Piezo Power Generator, Energy Harvesting: Principles, Analysis, Improvement, Optimization", Noliac Course Notes.

[19]   H.A. Sodano, D. J. Inman and G. Park, 2004, "A Review of Power Harvesting from Vibration by Piezoelectric Materials" , The Shock and Vibration Digest, Vol. 36, No. 3.

[20]   S. R. Pearson, 2006, "Characterization and Modeling of Piezoelectric Devices", Independent Study, Villanova University.

[21]   C. S. Pinkston, 2005, "An Investigation and Characterization of A High Energy Piezoelectric Pulse Generator", Msc. Thesis, University of Missouri, Coulumbia.

[22]   C. Keawboonchuay, 2003, "Electrical Power Generation Characteristics of Piezoelectric Generator under Quasi-Static and Dynamic Stress Conditions", IEEE Transactions on Plasma Science, Vol.31, No. 1.

[23]   C. Keawboonchuay and T.G. Engel, 2002, "Design, Modeling, and Implementation of a 30-kW Piezoelectric Pulse Generator." IEEE Transactions on Plasma Science, Volume 30, Issue 2, Part 2, Page(s):679 – 686.

[24]   T.G. Engel, C. Keawboonchuay and W.C. Nunnally, 2000, "Energy conversion and high power pulse production by miniature piezoelectric compressors." IEEE Transactions on Plasma Science, Volume 28, Issue 5, Page(s):1338 – 1341.

[25]   C. Keawboonchuay and T.G. Engel, 2003, "Maximum power generation in a piezoelectric pulse generator." IEEE Transactions on Plasma Science, vol. 31, Issue 1, Part 2, Page(s):123 – 128.

[26]   C. Keawboonchuay and T.G. Engel, 2004. "Scaling relationships and maximum peak power generation in a piezoelectric pulse generator." IEEE Transactions on Plasma Science, Volume 32, Issue 5, Part 1, Page(s):1879 – 1885.

[27]   J. Rastegar, R. Murray, C. Pereira and H-L. Nguyen, 2007, "Novel Piezoelectric-Based Energy-Harvesting Power Sources for Gun-Fired Munitions" Proc. of SPIE Vol. 6527 65270Y-1.

[28]   G.A. Lesieutre, G.K. Ottman and H.F. Hofmann, 2004, "Damping as a result of piezoelectric energy harvesting" , Journal of Sound and Vibration 269 991–100.

[29]   V. R. Challa, M. G. Prasad, Y. Shi and F. T. Fisher, 2007, "A Vibration Energy Harvesting Device with Bidirectional Resonance Frequency Tunability", Smart Mater. Struct. 17 015035

[30]   Omnitek   Partners,   Last   accessed   April   27,   2011, http://omnitekpartners.com/index.php?option=com_content&view=article&id=49:mi litarty-technologies&catid=36:military-technologies&Itemid=57

[31]   L. Meirovitch, 2001, "Fundamentals of Vibrations", McGraw-Hill International Edition.

[32]   Morgan   Piezoelectric   Ceramics,   Last   accessed   April   27, www.morganelectroceramics.com

[33]   S. Gheorghian, N. Jula, M. Pearsicá, C. Rácaciu, H.F. Hofmann, "Some Aspects Regarding the Use of Piezoelectric Transducers for Measurement of Propellant Gas Pressure during Weapon's Firing" , Technical Sciences and Applied Mathematics, Military Technical Academy, Braşov.

[34]   R. P. Oberlin, R. T. Soranno, "One-Shot High-Output Piezoid Power Supply", U.S. Patent 6, 198, 205 B1, issued Mar. 6, 2001.

[35]   J.C. Debus and P. Mosbah, 2005, "ATILA$^{®}$ Finite-Element Software Package for the Analysis of 2D & 3D Structures Based on Smart Materials User's Manual" , Institut Supérieur d'Electronique et du Numérique, Acoustics Laboratory.

[36] M/RAD Cooperation, Last accessed June 6 2011, http://www.mradcorp.com/prod_shocktesting.html

[37] T. Irvine, 2004, "Damping Properties of Materials". Last accessed July 13, 2011,

http://www.cs.wright.edu/~jslater/SDTCOutreachWebsite/damping%20properties%20of%20materials.pdf

[38] P. L. Walter, 2008, "Selecting Accelerometers for and Assessing Data from Mechanical Shock Measurements", Last accessed June 15 2011,, PCB Piezotronics Technical Note 24,

http://www.pcb.com/techsupport/docs/vib/LoRes_24__Mechanical_Shock_Tech.pdf.

[39] H. A. Gaberson, 2010, "Effects of Filtering Shock Data", Sound and Vibration, pp. 8-13.

[40] Kistler Instrument Corp, Last accessed June 15 2011, http://www.sensorsmag.com/sensors/acceleration-vibration/the-principles-piezoelectric-accelerometers-1022

[41] J. E. Shigley, 1986, "Mechanical Engineering Design", McGraw-Hill First Metric Edition, pp 291- 336.

[42] P. L. Walter, 2008, "Selecting Accelerometers for and Assessing Data from Mechanical Shock Measurements", PCB Piezotronics, Technical Note 24, Last accessed June 15 2011.

[43] T. Irvine, 2009 "An Introduction to the Shock Response Spectrum", Last accessed June 15 2011, http://www.vibrationdata.com/tutorials2/vrs.pdf

[44] M. Serridge and T. R. Licht, 1987, "Piezoelectric Accelerometers and Vibration Preamplifiers Theory and Application Handbook", Brüel & Kjaer, pp.105-106

[45] S. H. Park and A. V. Carazo, 2009, "User Defined Waveform Generation by ATILA® Transient Module with Wilson-Q Methods", Micromechatronics Inc.

APPENDIX A

NOLIAC PIEZOELECTRIC MATERIAL PROPERTIES

Piezo ceramics specifications

Properties	Symbol & unit	NCE40	NCE41	NCE46*	NCE51	NCE53	NCE55	NCE57*	NCE59*	NCE80
DIELECTRIC PROPERTIES (tolerances +/- 10%)										
Relative Dielectric Constant	$\frac{\varepsilon^T_{33}}{\varepsilon_0}$	1250	1350	1300	1850	1600	5000	1800	2900	1050
Dielectric Loss Factor	$tg\delta$ [10^{-4}]	25	40	30	190	130	220	170	190	20
Dielectric Loss Factor at 400V/mm	$tg\delta$ [10^{-4}]	140	200							100
ELECTROMECHANICAL PROPERTIES (tolerances +/- 5%)										
Coupling Factors**	k_p	0.58	0.57	0.57	0.65	0.56	0.62	0.59	0.64	0.55
	k_{31}	0.34	0.33	0.33	0.37	0.32	0.39	0.33	0.37	0.30
	k_{33}	0.70	0.68	0.68	0.72	0.65	0.72	0.70	0.75	0.68
	k_t	0.50	0.50	0.47	0.51	0.47	0.50	0.47	0.52	0.48
Piezoelectric Charge Constants	$-d_{31}$ [10^{-12} C/N]	140	130	130	195	150	260	170	240	100
	d_{33} [10^{-12} C/N]	320	310	290	460	360	670	425	575	240
Piezoelectric Voltage Constants	$-g_{31}$ [10^{-3} Vm/N]	11	11	11	13	9	9	11	10	11
	g_{33} [10^{-3} Vm/N]	27	25	28	27	23	19	27	23	27
Frequency Constants	N^E_p [m/s]	2160	2280	2230	1940	2180	1970	2010	1970	2270
	N^D_t [m/s]	1980	2000	2040	2010	2040	1990	1950	1960	2050
	N^E_1 [m/s]	1470	1600	1500	1400			1400	1410	1610
	N^D_3 [m/s]	1340	1500	1800	1390			1500	1500	1500
PHYSICAL PROPERTIES (tolerances +/- 5%)										
Mechanical Quality Factor	Q_m	700	1400	>1000	80	80	70	80	90	1000
Density	ρ [10^3 kg/m^3]	7.75	7.90	7.70	7.80	7.60	8.00	7.70	7.45	7.80
Elastic Compliances	s^E_{11} [10^{-12} m^2/N]	13	13	13	16	16	17	17	17	11
	s^E_{33} [10^{-12} m^2/N]	17	16	20	19	18	21	23	23	14
Curie Temperature	T_c [°C]	325	290	330	340	340	170	350	235	305

*) For multilayer components only.
**) Measured in accordance with standard EN 50324.

Piezo actuator specifications (table rotated 90° on the page; transcribed with products as rows).

Name	Plates	Rings	Linear	Stacked	Length (L)/Outer diameter (OD) (mm)	Tol.	Width (W)/Inner diameter (ID) (mm)	Tol.	Width max (W_m)	Height (H) (mm)	Tol.	Nominal operating voltage (V)	Free stroke @ nom. (µm) ±15%	Blocking force @ nom. (N) ±20%	Capacitance (nF) ±15%	Max. op. temp (°C)	Material (NCE)	Unloaded resonance frequency (Hz)
SCMAR05		x	x	x	20	+0.8/-0.6	12	+0.4/-0.6	22.3	4-200	+/-0.2 or 1%*	200	2.9-282	8000	784-77600	150	NCE57	>250k - >6 k
SCMAR04		x	x	x	15	+0.65/-0.45	9	+0.3/-0.5	17.2	4-150	+/-0.2 or 1%*	200	2.7-197	4530	475-35150	150	NCE57	>250k - >7 k
SCMAR03		x	x	x	12	+0.6/-0.4	6	+0.2/-0.4	14.1	4-120	+/-0.2 or 1%*	200	2.7-157	2670	333-19600	150	NCE57	>250k - >9 k
SCMAR02		x	x	x	8	+0.45/-0.25	3	+0.1/-0.3	10	4-80	+/-0.2 or 1%*	200	2.6-100	1700	162-6300	150	NCE57	>250k - >14k
SCMAR01		x	x	x	6	+0.4/-0.2	2	+0.1/-0.3	7.9	4-60	+/-0.2 or 1%*	200	2.6-74	1000	95-2750	150	NCE57	>250k - >18k
CMAR05		x	x		20	+/-0.6	12	+/-0.4		2	+/-0.05	200	3	8000	825	200	NCE57	>500k
CMAR04		x	x		15	+/-0.45	9	+/-0.3		2	+/-0.05	200	2.8	4530	500	200	NCE57	>500k
CMAR03		x	x		12	+/-0.4	6	+/-0.2		2	+/-0.05	200	2.8	2670	350	200	NCE57	>500k
CMAR02		x	x		8	+/-0.25	3	+/-0.1		2	+/-0.05	200	2.7	1700	170	200	NCE57	>500k
CMAR01		x	x		6	+/-0.2	2	+/-0.1		2	+/-0.05	200	2.7	1000	100	200	NCE57	>500k
SCMAP12	x			x	2	+0.3/-0.1	2	+0.3/-0.1	3.8	4-20**	+/-0.2 or 1%*	120	2.4-21	160	34-310	150	NCE57	>250k - >52 k
SCMAP11	x			x	5	+0.3/-0.1	5	+0.3/-0.1	6.8	4-50	+/-0.2 or 1%*	200	1.9-46	800	71-1700	200	NCE46	>250k - >22 k
SCMAP10	x			x	3	+0.3/-0.1	3	+0.3/-0.1	4.8	4-30	+/-0.2 or 1%*	200	1.7-24	290	24-350	200	NCE46	>250k - >35 k
SCMAP09	x			x	10	+0.4/-0.2	10	+0.4/-0.2	11.9	4-100	+/-0.2 or 1%*	200	3-149	4000	418-20500	150	NCE57	>250k - >11 k
SCMAP08	x			x	7	+0.35/-0.15	7	+0.35/-0.15	8.9	4-70	+/-0.2 or 1%*	200	3-103	1960	209-7100	150	NCE57	>250k - >16 k
SCMAP07	x			x	5	+0.3/-0.1	5	+0.3/-0.1	6.8	4-50	+/-0.2 or 1%*	200	2.9-71	1000	100-2300	150	NCE57	>250k - >22 k
SCMAP06	x			x	3	+0.3/-0.1	3	+0.3/-0.1	4.8	4-30	+/-0.2 or 1%*	200	2.8-39	360	29-400	150	NCE57	>250k - >35 k
SCMAP05	x			x	7	+0.35/-0.15	7	+0.35/-0.1	8.9	4-70	+/-0.2 or 1%*	150	2.9-100	1960	390-13250	150	NCE57	>250k - >16 k
SCMAP04	x			x	5	+0.3/-0.1	5	+0.3/-0.1	6.8	5-50	+/-0.2 or 1%*	150	4.6-73	1000	238-3800	150	NCE57	>200k - >22 k
SCMAP03	x			x	3	+0.3/-0.1	3	+0.3/-0.1	4.8	5-30	+/-0.2 or 1%*	150	4.2-39	360	100-950	150	NCE57	>200k - >35 k
SCMAP02	x			x	5	+0.3/-0.1	3	+0.3/-0.1	5.8	4-50	+/-0.2 or 1%*	60	2.7-64	1000	1400-33300	125	NCE59	>250k - >22 k
SCMAP01	x			x	3	+0.3/-0.1	3	+0.3/-0.1	4.8	4-30	+/-0.2 or 1%*	60	2.3-33	360	450-6300	125	NCE59	>250k - >35 k
CMAP12	x		x		2	+/-0.1	2	+/-0.1		2	+/-0.05	120	2.8	160	36	200	NCE57	>500k
CMAP11	x		x		5	+/-0.1	5	+/-0.1		2	+/-0.05	200	2	800	75	200	NCE46	>500k
CMAP10	x		x		3	+/-0.1	3	+/-0.1		2	+/-0.05	200	1.8	290	25	200	NCE46	>500k
CMAP09	x		x		10	+/-0.2	10	+/-0.2		2	+/-0.05	200	3.2	4000	440	200	NCE57	>500k
CMAP08	x		x		7	+/-0.15	7	+/-0.15		2	+/-0.05	200	3.2	1960	220	200	NCE57	>500k
CMAP07	x		x		5	+/-0.1	5	+/-0.1		2	+/-0.05	200	3.1	1000	100	200	NCE57	>500k
CMAP06	x		x		3	+/-0.1	3	+/-0.1		2	+/-0.05	200	2.9	360	30	200	NCE57	>500k
CMAP05	x		x		7	+/-0.1	7	+/-0.1		3	+/-0.05	150	3.1	1960	410	200	NCE57	>500k
CMAP04	x		x		5	+/-0.1	5	+/-0.1		3	+/-0.05	150	4.8	1000	250	200	NCE57	>300k
CMAP03	x		x		3	+/-0.1	3	+/-0.1		3	+/-0.05	150	4.4	360	105	200	NCE57	>300k
CMAP02	x		x		5	+/-0.1	3	+/-0.05		3	+/-0.05	60	2.8	1000	1460	125	NCE59	>500k
CMAP01	x		x		3	+/-0.1	3	+/-0.1		3	+/-0.05	60	2.6	360	500	125	NCE59	>500k

* Whichever is largest
** For stacks higher than 10mm, it may be necessary to add a support within the application in order to avoid bending and buckling during mounting and operation.

Noliac A/S

Material data based on typical values

Symbol	Unit	NCE46	NCE57	NCE59
$\varepsilon_{1,r}^{\sigma}$		1.19E+03	1.80E+03	2.44E+03
$\varepsilon_{3,r}^{\sigma}$		1.33E+03	1.80E+03	2.87E+03
$\varepsilon_{1,r}^{S}$		8.28E+02	1.13E+03	1.34E+03
$\varepsilon_{3,r}^{S}$		7.00E+02	9.14E+02	1.22E+03
$\tan\delta(_3{}^{\sigma})$		0.003	0.017	0.016
$T_C >$	ºC	330	350	235
k_p		0.568	0.592	0.643
k_t		0.471	0.469	0.524
k_{31}		0.327	0.327	0.370
k_{33}		0.684	0.699	0.752
k_{15}		0.553	0.609	0.671
d_{31}	C/N	-1.28E-10	-1.70E-10	-2.43E-10
d_{33}	C/N	3.28E-10	4.25E-10	5.74E-10
d_{15}	C/N	3.27E-10	5.06E-10	7.24E-10
d_h	C/N	7.24E-11	8.50E-11	8.82E-11
g_{31}	V m/N	-0.0109	-0.0107	-0.0096
g_{33}	V m/N	0.0280	0.0267	0.0226
g_{15}	V m/N	0.0389	0.0373	0.0321
e_{31}	C/m^2	-2.80	-3.09	-5.06
e_{33}	C/m^2	14.7	16.0	21.2
e_{15}	C/m^2	9.86	11.64	13.40
h_{31}	V/m	-4.52E+08	-3.82E+08	-4.68E+08
h_{33}	V/m	2.37E+09	1.98E+09	1.96E+09
h_{15}	V/m	1.34E+09	1.16E+09	1.13E+09
N_p	m/s	2209.94	2011.08	1970.47
N_t	m/s	2038	1953	1966
N_{31}	m/s	1500	1400	1410
N_{33}	m/s	1800	1500	1500
N_{15}	m/s	1018	896	822
$Q_{m,p}{}^{E}$		2.7E+03	89	76
$Q_{m,t}{}^{E}$		3.3E+03	74	195
ρ	kg/m^3	7.70E+03	7.70E+03	7.46E+03
$\nu_{12}{}^{E}$		0.334	0.389	0.340
$s_{11}{}^{E}$	m^2/N	1.30E-11	1.70E-11	1.70E-11

$s_{12}{}^{E}$	m^2/N	-4.35E-12	-6.60E-12	-5.78E-12
$s_{13}{}^{E}$	m^2/N	-7.05E-12	-8.61E-12	-8.79E-12
$s_{33}{}^{E}$	m^2/N	1.96E-11	2.32E-11	2.29E-11
$s_{44}{}^{E} = s_{55}{}^{E}$	m^2/N	3.32E-11	4.35E-11	5.41E-11
s_{66}	m^2/N	3.47E-11	4.71E-11	4.56E-11
$s_{11}{}^{D}$	m^2/N	1.16E-11	1.51E-11	1.47E-11
$s_{12}{}^{D}$	m^2/N	-5.74E-12	-8.41E-12	-8.10E-12
$s_{13}{}^{D}$	m^2/N	-3.47E-12	-4.08E-12	-3.30E-12
$s_{33}{}^{D}$	m^2/N	1.05E-11	1.19E-11	9.94E-12
$s_{44}{}^{D} = s_{55}{}^{D}$	m^2/N	2.31E-11	2.73E-11	2.98E-11
$c_{11}{}^{E}$	N/m^2	1.68E+11	1.47E+11	1.34E+11
$c_{12}{}^{E}$	N/m^2	1.10E+11	1.05E+11	8.97E+10
$c_{13}{}^{E}$	N/m^2	9.99E+10	9.37E+10	8.57E+10
$c_{33}{}^{E}$	N/m^2	1.23E+11	1.13E+11	1.09E+11
$c_{44}{}^{E} = c_{55}{}^{E}$	N/m^2	3.01E+10	2.30E+10	1.85E+10
c_{66}	N/m^2	2.88E+10	2.12E+10	2.20E+10
$c_{11}{}^{D}$	N/m^2	1.69E+11	1.49E+11	1.36E+11
$c_{12}{}^{D}$	N/m^2	1.12E+11	1.06E+11	9.21E+10
$c_{13}{}^{D}$	N/m^2	9.33E+10	8.75E+10	7.58E+10
$c_{33}{}^{D}$	N/m^2	1.58E+11	1.44E+11	1.51E+11
$c_{44}{}^{D} = c_{55}{}^{D}$	N/m^2	4.34E+10	3.66E+10	3.36E+10
$Y_{11}{}^{E}$	GPa	7.69E+01	5.90E+01	5.88E+01
$Y_{33}{}^{E}$	GPa	5.09E+01	4.31E+01	4.37E+01
$Y_{11}{}^{D}$	GPa	8.62E+01	6.60E+01	6.81E+01
$Y_{33}{}^{D}$	GPa	9.56E+01	8.43E+01	1.01E+02

APPENDIX B

ACCELEROMETER PROPERTIES

Dytran INSTRUMENTS, INC.

Dynamic Transducers and Systems
21592 Marilla St. • Chatsworth, CA 91311 • Phone 818-700-7818
www.dytran.com • e-mail: info@dytran.com

NOTE: **LIVM** is Dytran's trademark for its line of Low Impedance Voltage Mode sensors with built in amplifiers operating from constant current sources over two wires. **LIVM** instruments are compatible with most other manufacturers' comparable systems.

SPECIFICATIONS, MODEL SERIES 3200B, 3200BT & 3200BM [1]
LIVM HIGH SHOCK ACCELEROMETERS

SPECIFICATIONS BY MODEL

MODELS	RANGE F.S. (G's)	MAXIMUM SHOCK (G's)	SENSITIVITY (NOM) [2] (mV/G)	ELECTRICAL NOISE (G's)	NATURAL FREQUENCY (kHz)
3200B , BT & BM	+/-70,000	100,000	0.05	0.014	130
3200B2, B2T & B2M	+/-50,000	100,000	0.1	0.007	130
3200B3, B3T & B3M	+/-20,000	100,000	0.25	0.0028	130
3200B4, B4T & B4M	+/-10,000	50,000	0.5	0.0014	130
3200B5, B5T & B5M	+/- 5,000	50,000	1.0	0.0007	130
3200B6, B6T & B6M	+/- 2,500	50,000	2.0	0.0035	100

COMMON SPECIFICATIONS

SPECIFICATION	VALUE	UNITS
DISCHARGE TIME CONSTANT, NOM.	1.0	SECOND
LOW FREQUENCY -3db POINT, NOM.	.16	Hz
LOW FREQUENCY -5% POINT	.50	Hz
FREQUENCY RESPONSE, ±10%	.35 to 10000	Hz
LINEARITY [3]	±1	% F.S.
TRANSVERSE SENSITIVITY, MAXIMUM	3.0	%
OUTPUT IMPEDANCE, NOM.	100	OHMS
OUTPUT VOLTAGE BIAS, NOM.	+8.5	VDC
SUPPLY CURRENT RANGE [4]	2 to 20	mA
COMPLIANCE (SUPPLY) VOLTAGE RANGE [4]	+18 to +20	VDC
OPERATING TEMPERATURE RANGE	-60 to +250	°F
SIZE (HEX x HEIGHT) [5]	3/8 x .64	INCHES
WEIGHT	6	GRAMS
CONNECTOR, TOP MOUNTED	10-32	MICRO-COAXIAL
MATERIAL, HOUSING/CONNECTOR	17-4 PH	STAINLESS STEEL
MOUNTING PROVISION, 3200B/3200BT/3200BM	1/4-28/10-32/M6 x 1.0	INTEGRAL STUD
ENVIRONMENTAL SEAL	EPOXY	
ISOLATION, CASE TO MOUNTING SURFACE	10	MEGOHMS

[1] Model series 3200B features 1/4-28 mounting stud, series 3200BT features 10-32 stud, series 3200BM has a m6 x 1.0 metric mounting stud. All other characteristics are identical.
[2] Measured by impacting against calibrated force sensor. NIST traceable.
[3] Percent of full scale or any lesser designated full scale range, zero-based best fit straight line method.

REV F. ECN 7325, 01/18/11   2

ACCELEROMETER, ICP®, TRIAXIAL

Model Number		Revision G
356B21		ECN #: 32784

	ENGLISH	SI	
Performance			
Sensitivity (±10 %)	10 mV/g	1.02 mV/(m/s²)	
Measurement Range	±500 g pk	±4905 m/s² pk	
Frequency Range (±5 %) (y or z axis)	2 to 10000 Hz	2 to 10000 Hz	
Frequency Range (±5 %) (x axis)	2 to 7000 Hz	2 to 7000 Hz	
Resonant Frequency	≥55 kHz	≥55 kHz	
Broadband Resolution (1 to 10000 Hz)	0.004 g rms	0.04 m/s² rms	[1]
Non-Linearity	≤1 %	≤1 %	[3]
Transverse Sensitivity	≤5 %	≤5 %	
Environmental			
Overload Limit (Shock)	±10000 g pk	±98100 m/s² pk	
Temperature Range (Operating)	-65 to +250 °F	-54 to +121 °C	[2]
Temperature Response	See Graph	See Graph	[1][2]
Electrical			
Excitation Voltage	18 to 30 VDC	18 to 30 VDC	
Constant Current Excitation	2 to 20 mA	2 to 20 mA	
Output Impedance	≤200 ohm	≤200 ohm	
Output Bias Voltage	7 to 11 VDC	7 to 11 VDC	
Discharge Time Constant	0.3 to 1.0 sec	0.3 to 1.0 sec	
Settling Time (within 10% of bias)	<3 sec	<3 sec	
Spectral Noise (1 Hz)	1000 µg/√Hz	9810 (µm/sec²)²/√Hz	[1]
Spectral Noise (10 Hz)	300 µg/√Hz	2943 (µm/sec²)²/√Hz	[1]
Spectral Noise (100 Hz)	100 µg/√Hz	981 (µm/sec²)²/√Hz	[1]
Spectral Noise (1 kHz)	50 µg/√Hz	490 (µm/sec²)²/√Hz	[1]
Physical			
Sensing Element	Ceramic	Ceramic	
Sensing Geometry	Shear	Shear	
Housing Material	Titanium	Titanium	
Sealing	Hermetic	Hermetic	
Size (Height x Length x Width)	0.4 in x 0.4 in x 0.4 in	10.2 mm x 10.2 mm x 10.2 mm	
Weight	0.14 oz	4 gm	[1]
Electrical Connector	8-36 4-Pin	8-36 4-Pin	
Electrical Connection Position	Side	Side	
Mounting Thread	5-40 Female	5-40 Female	

Optional Versions (Optional versions have identical specifications and accessories as listed for standard model except where noted below. More than one option maybe be used.)

A - Adhesive Mount
    Supplied Accessory: Model 080A109 Petro Wax
    Supplied Accessory: Model 080A90 Quick bond Gel (for use with accelerometer
    adhesive mtg bases to fill gaps on rough surfaces)

HT - High temperature, extends normal operation temperatures

J - Ground Isolated			
Temperature Range (Operating)	-65 to +325 °F	-54 to +163 °C	
Frequency Range (+5 %)	7000 Hz	7000 Hz	
Electrical Isolation (Base)	>10⁴ ohm	>10⁴ ohm	
Size (Height x Length x Width)	0.44 in x 0.40 in x 0.44 in	11.2 mm x 11.2 mm x 10.2 mm x 11.2 mm	
Weight	0.16 oz	4.5 gm	
Mounting	Adhesive	Adhesive	

Supplied Accessory: Model 080A109 Petro Wax
Supplied Accessory: Model 080A109 Petro Wax
Supplied Accessory: Model 080A90 Quick bond Gel (for use with accelerometer adhesive mtg bases to fill gaps on rough surfaces)

Notes
[1] Typical.
[2] 250° F to 325° F data valid with HT option only.
[3] Zero-based, least-squares, straight line method.
[4] See PCB Declaration of Conformance PS023 for details.

Supplied Accessories
034K10 Cable 10FT Mini 4 Pin To (3) BNC (1)
080A109 Petro Wax (1)
080A Adhesive Mounting Base (1)
080A109 Petro Wax (1)
081A27 Mounting Stud (5-40 to 5-40) (1)
081A90 Mounting stud, 10-32 to 5-40 (1)
ACS-1T NIST traceable triaxial amplitude response, 10 Hz to upper 5% frequency. (1)
M081A27 Metric mounting stud, 5-40 to M3 x 0.50 long (1)

Sensitivity Deviation(%)

Typical Sensitivity Deviation vs Temperature

Entered: LLH	Engineer: AJA	Sales: WDC	Approved: EB	Spec Number:
Date: 04/21/2010	Date: 04/20/2010	Date: 04/20/2010	Date: 04/20/2010	15127

PCB PIEZOTRONICS™
VIBRATION DIVISION

3425 Walden Avenue
Depew, NY 14043
UNITED STATES
Phone: 888-684-0013
Fax: 716-685-3886
E-mail: vibration@pcb.com
Web site: www.pcb.com

CE [4]

All specifications are at room temperature unless otherwise specified.
In the interest of constant product improvement, we reserve the right to change specifications without notice.
ICP® is a registered trademark of PCB group, Inc.

APPENDIX C

DETAILS OF EXPERIMENTAL ARRANGEMENTS
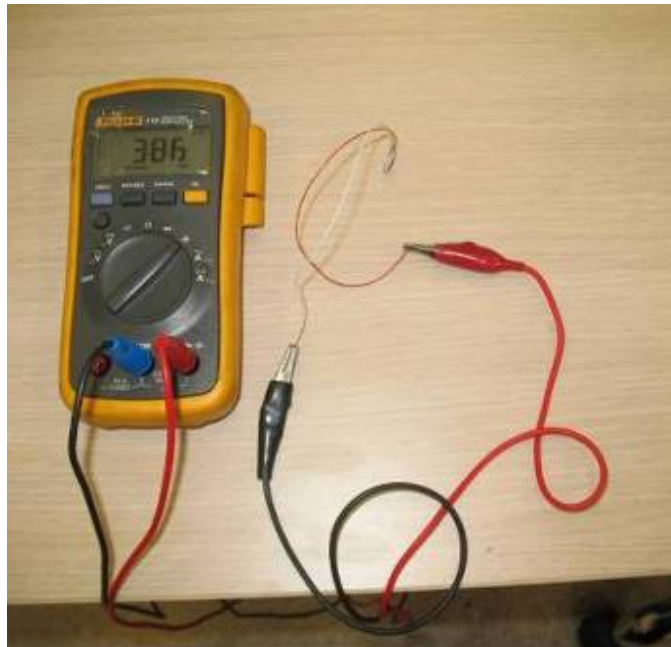
Figure C.1 CMAR03 Capacitance Measurement

Figure C.2 CMAR04 Capacitance Measurement

Figure C.3 NCE40 Capacitance Measurement

Figure C.4 CMAR03 Capacitance Measurement after Tightening for Impact Hammet Tests

Figure C.5 CMAR03 Capacitance Measurement after Tightening for Pressure Gun Tests

Figure C.6 CMAR04 Capacitance Measurement after Tightening for Pressure Gun Tests

Electrical Resistance

Piezoelectric Material
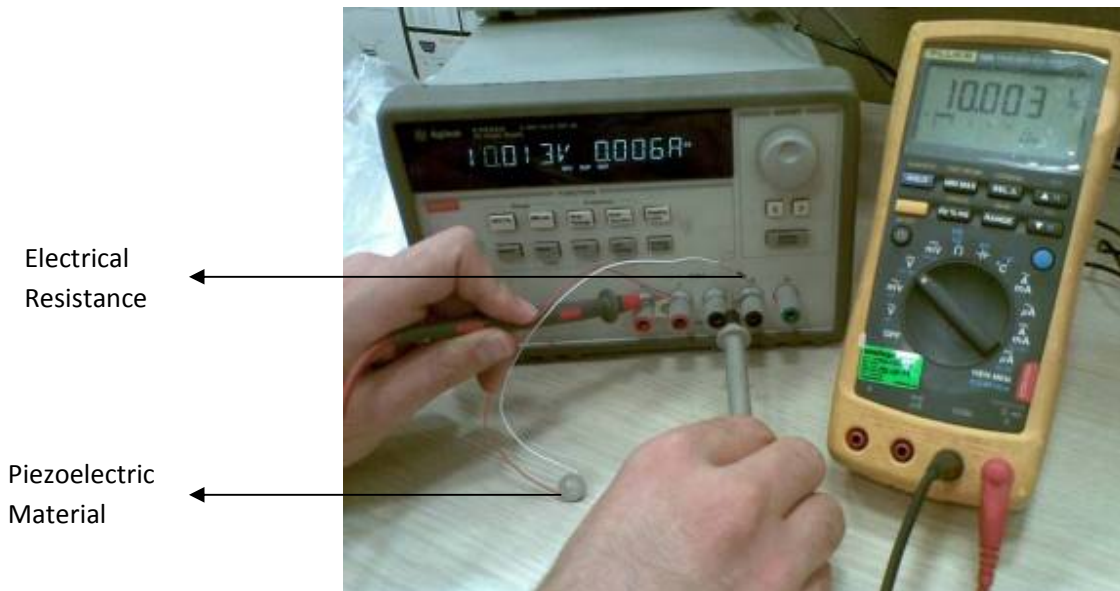
Figure C.7 Input Voltage Measurement for Leakage Resistance Calculation
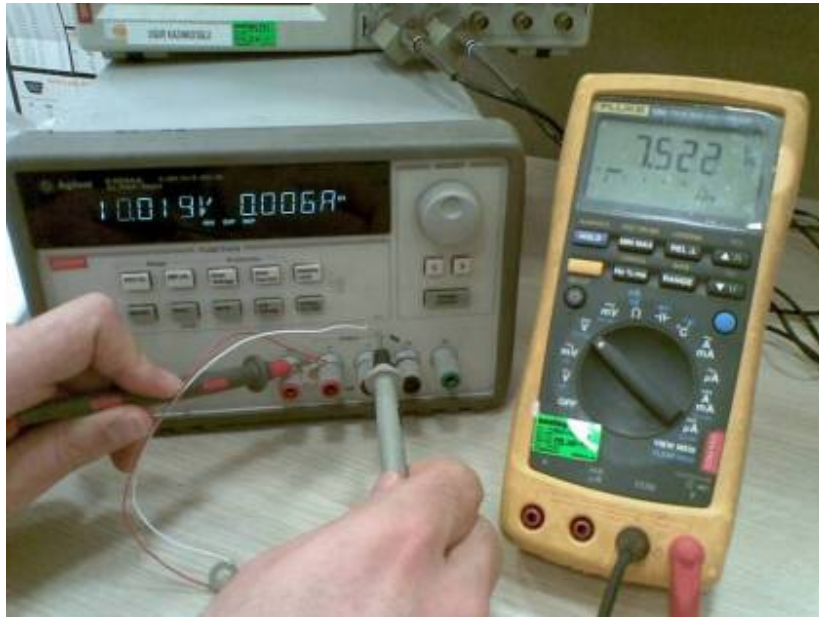
Figure C.8 Output Voltage Measurement for Leakage Resistance Calculation
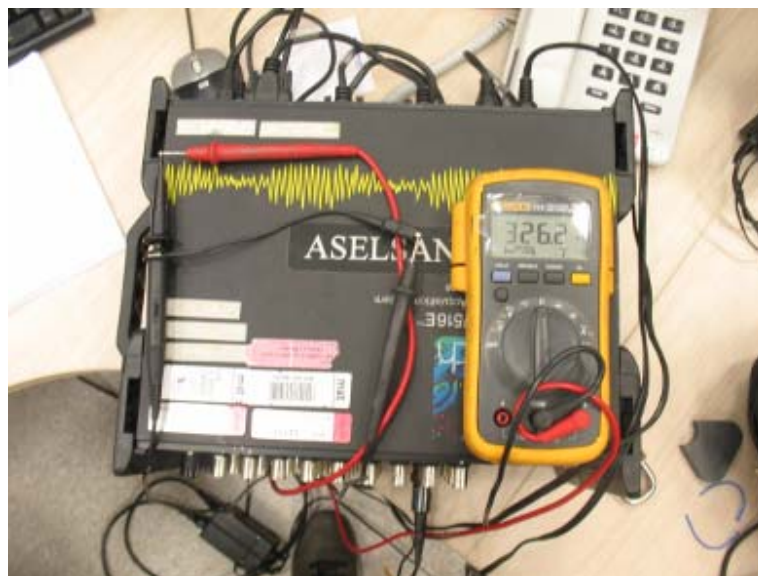
Figure C.9 Measurement of Resistance of Oscilloscope Probe

Measuring Large Voltages - Example

Approx MAX External Voltage Vmax	Resistance R	* Sensitivity mV/V
+/-20V	45.3K	99.404
+/-40V	95.3K	49.850
+/-60V	150K	32.258

* Sensitivity calculation....

$$\left(\frac{5}{(5+R)}\right) \times 1000$$
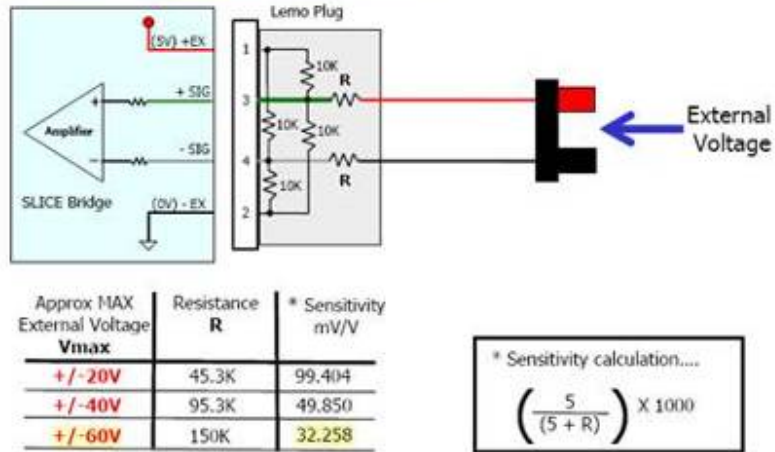
Figure C.10 SliceWare 4865-01 Cable Electrical Scheme
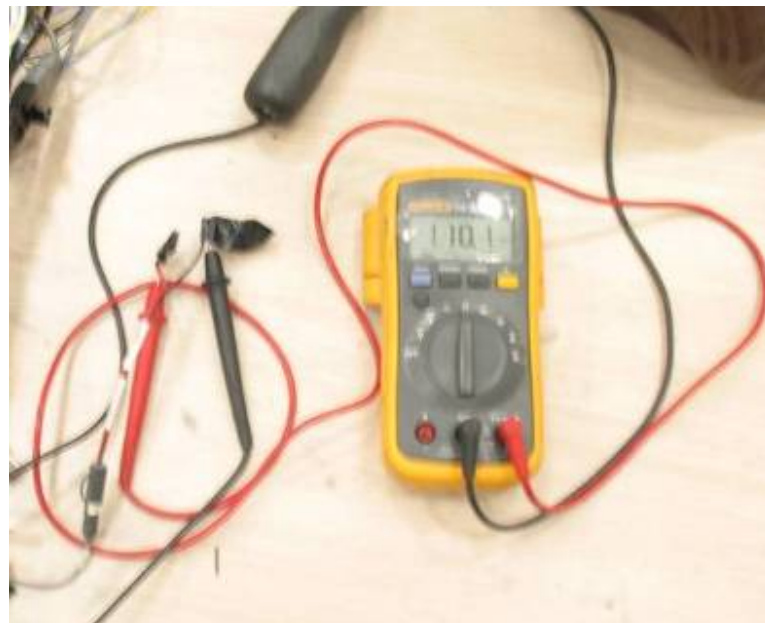
Figure C.11 Equivalent Resistance Measurement of 4865-01 Cable

Figure C.12 Agilent E3634A Power Supply

Figure C.13 NCE 40 Material and Electrical Isolators

Figure C.14 Sample Steel Compression Mass in Harmonic Loading Tests

Figure C.15 Aluminum Apparatus for Modal Shaker Connection

Figure C.16 Accelerometer Glued on Compression Mass

Figure C.17 Impact Hammers

Figure C.18 Loctite Silver Anti-Seize Product

Figure C.19 Micro-Epsilon Laser Displacement Sensor

Figure C.20 Slice Nano Data Acquisition System

Figure C.21 MSI Model 64 Accelerometer

Protection
Apparatus

Compression
Direction

Compression
Mass
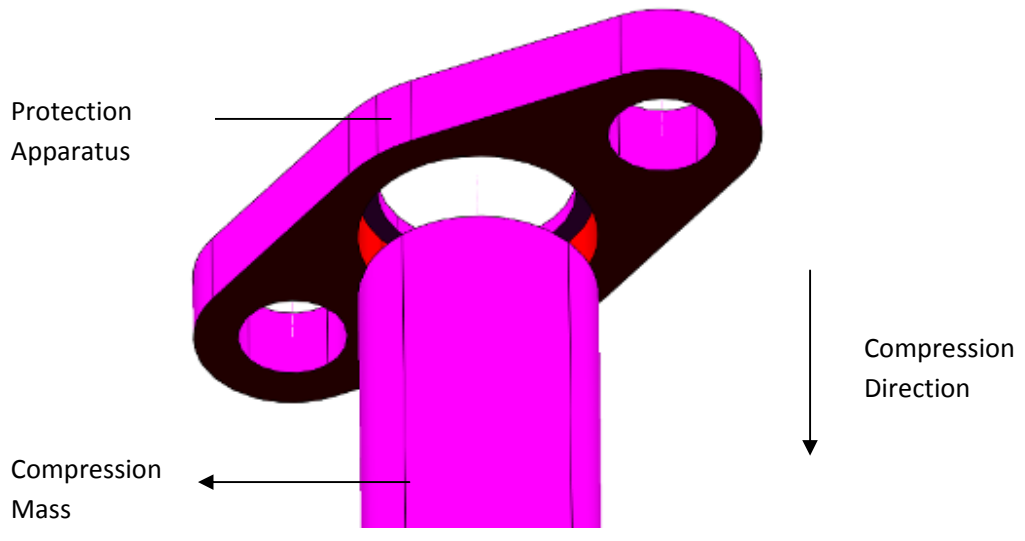
Figure C.22 Protection Apparatus Montage

APPENDIX D

DETAILS OF ANALYSIS PROCEDURES
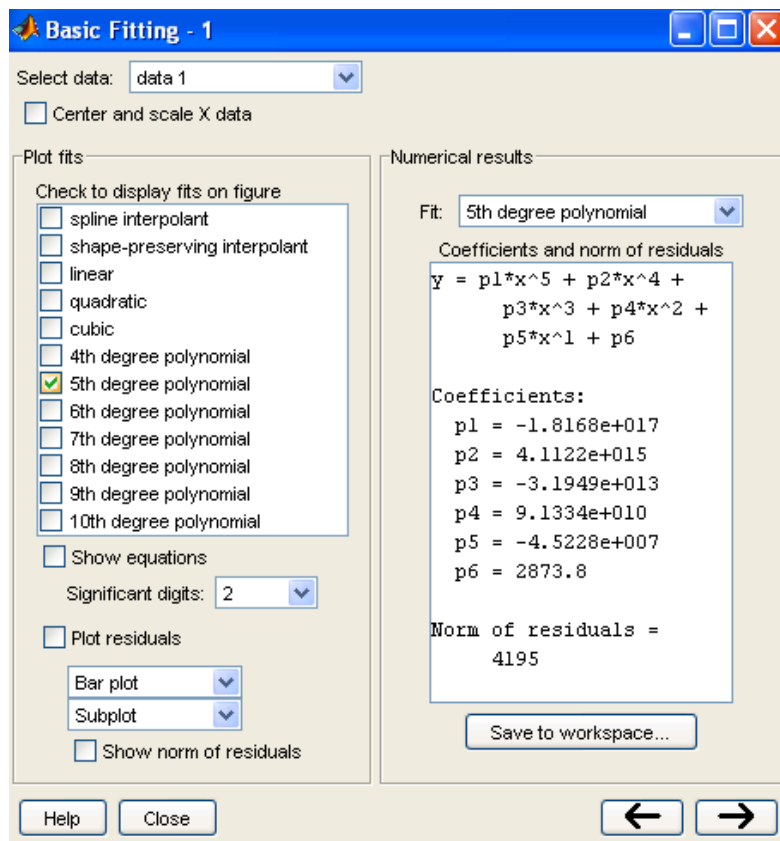
Figure D.1 Acceleration Formulization by MATLAB® Basic Fitting Toolbox in Mechanical Resonator Calculation
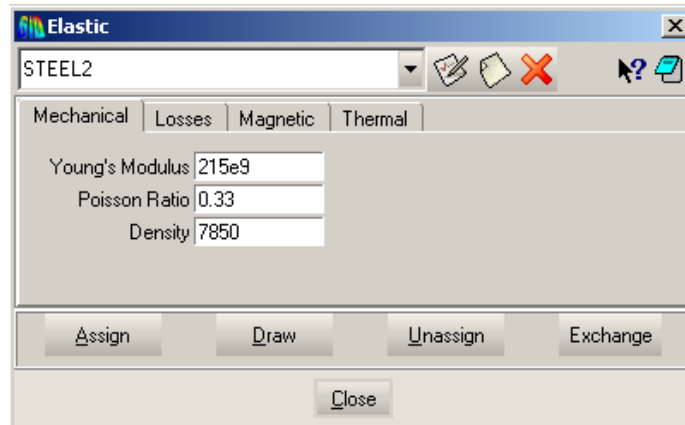
Figure D.2 Steel Material Properties
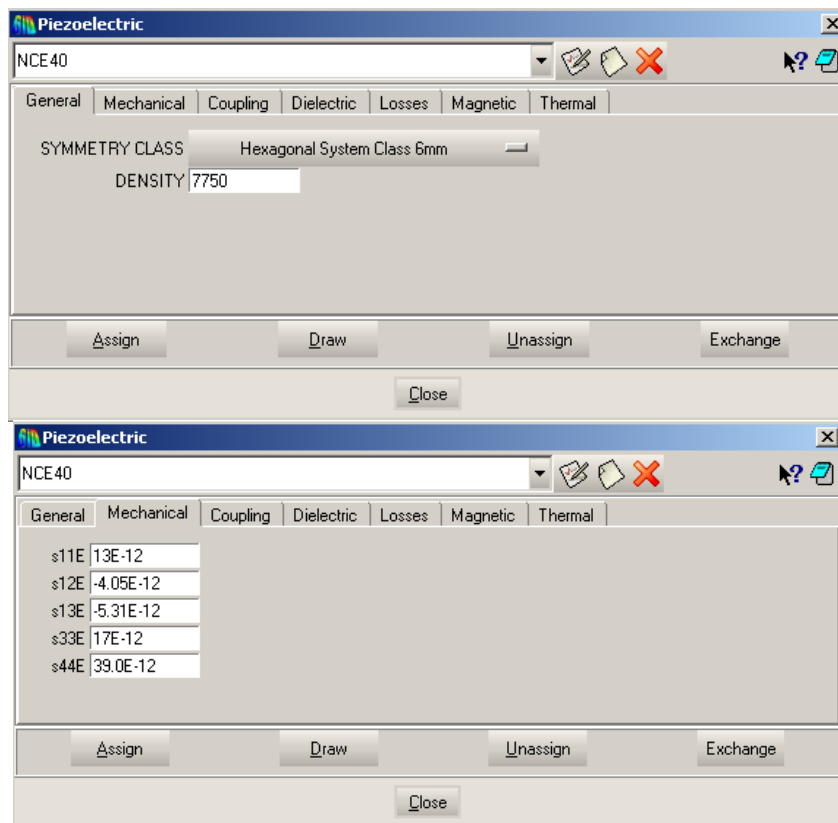
Figure D.3 NCE 40 Material Properties

Piezoelectric — NCE40

General | Mechanical | Coupling | Dielectric | Losses | Magnetic | Thermal

d15 496e-12
d31 -140e-12
d33 320e-12

Assign   Draw   Unassign   Exchange

Close

Piezoelectric — NCE40

General | Mechanical | Coupling | Dielectric | Losses | Magnetic | Thermal

E11T/E0 1475
E33T/E0 1250

Assign   Draw   Unassign   Exchange

Close

Piezoelectric — NCE40

General | Mechanical | Coupling | Dielectric | Losses | Magnetic | Thermal

DELTA M 0.000715
DELTA P 0.
DELTA D 0.0025

Assign   Draw   Unassign   Exchange

Close

Figure D.3 NCE 40 Material Properties (Continued)

Figure D.4 Reference Acceleration Value for Harmonic Analysis in ATILA®

Figure D.5 Reference Voltage Value for Harmonic Analysis in ATILA
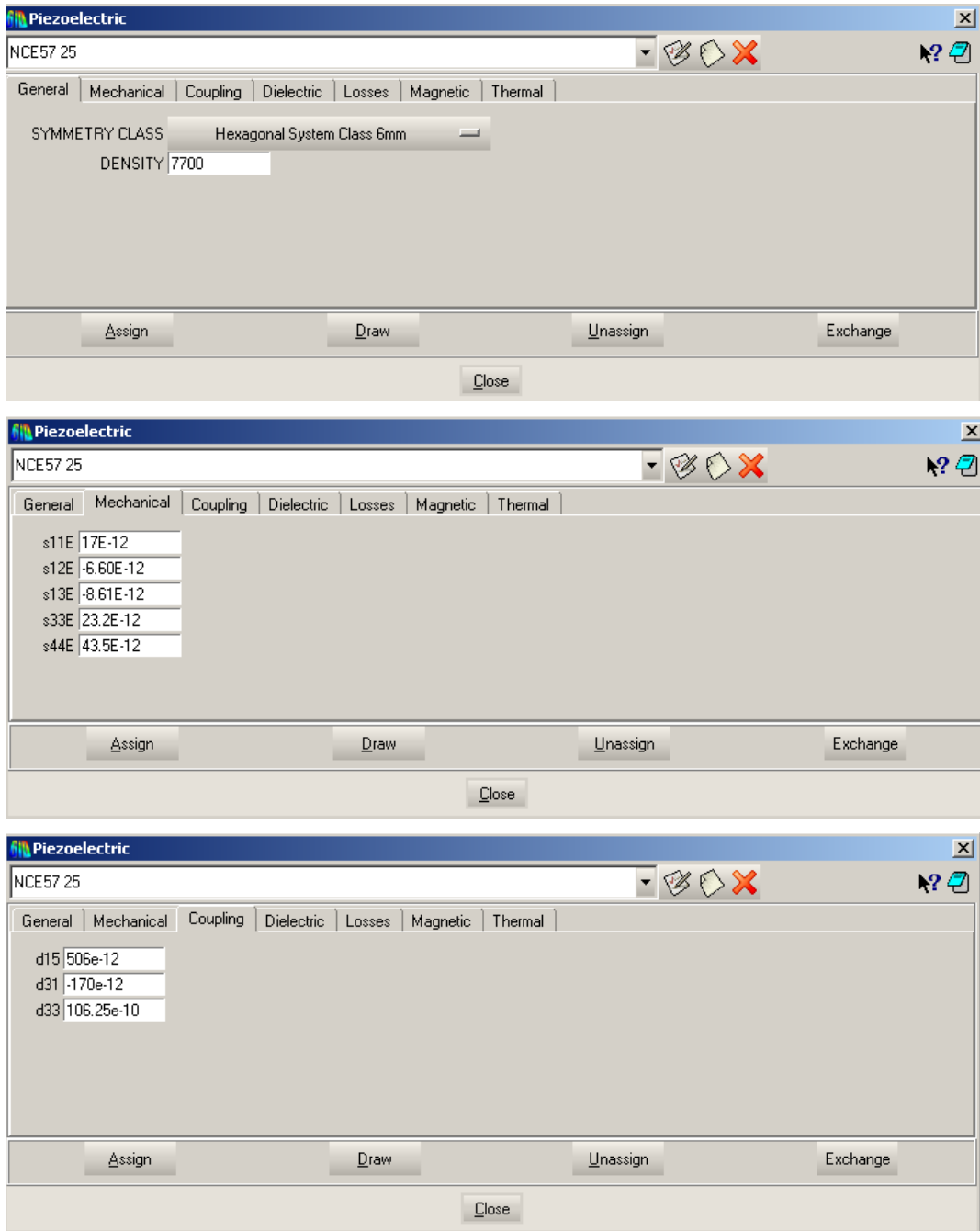
Figure D.6 NCE 57 Material Properties for Single Layer Modelling
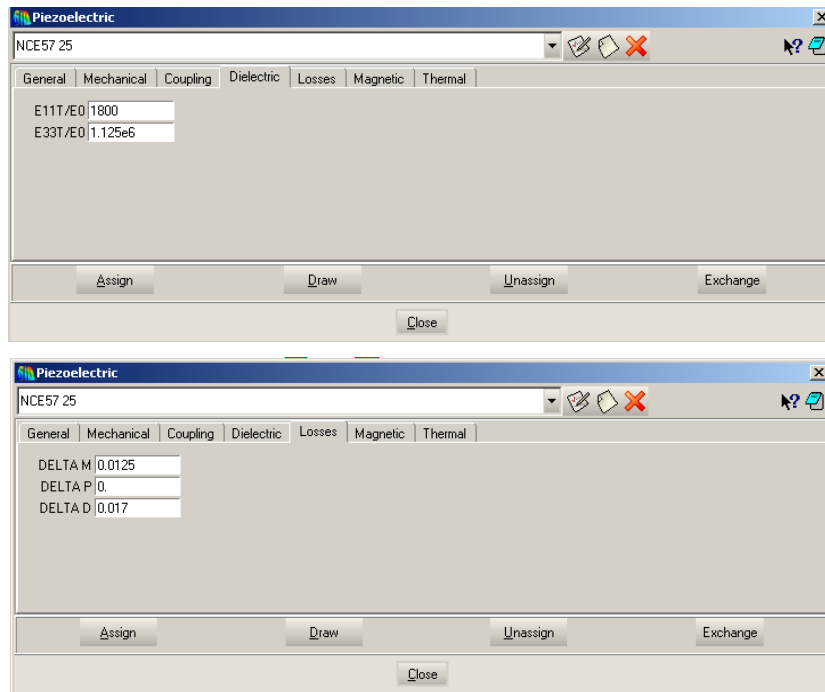
Figure D.6 NCE 57 Material Properties for Single Layer Modelling (Continued)

Figure D.7 ATILA Analysis File Arrangement for Transient Loading

	A	B	C	D
1	0.0000000000E+00	0.0000000000E+00	0.0000000000E+00	2.6480000000E+01
2	1.0000000000E-03	8.4220000000E-06	1.4000000000E-02	1.0000000000E+01
3	2.0000000000E-03	2.9540000000E-05	3.0270000000E-02	2.1240000000E+01
4	3.0000000000E-03	7.1040000000E-05	5.3460000000E-02	2.6040000000E+01
5	4.0000000000E-03	1.3910000000E-04	8.4060000000E-02	3.4860000000E+01
6	5.0000000000E-03	2.4180000000E-04	1.2280000000E-01	4.3050000000E+01
7	6.0000000000E-03	3.8770000000E-04	1.7050000000E-01	5.2090000000E+01
8	7.0000000000E-03	5.8570000000E-04	2.2710000000E-01	6.1190000000E+01
9	8.0000000000E-03	8.4480000000E-04	2.9240000000E-01	6.8880000000E+01
10	9.0000000000E-03	1.1730000000E-03	3.6410000000E-01	7.4570000000E+01
11	1.0000000000E-02	1.5750000000E-03	4.4100000000E-01	7.8100000000E+01
12	1.1000000000E-02	2.0550000000E-03	5.1840000000E-01	7.8710000000E+01
13	1.2000000000E-02	2.6160000000E-03	6.1040000000E-01	1.1190000000E+02
14	1.3000000000E-02	3.2920000000E-03	7.5210000000E-01	1.7970000000E+02
15	1.4000000000E-02	4.1570000000E-03	1.0070000000E+00	3.5640000000E+02
16	1.5000000000E-02	5.3900000000E-03	1.5120000000E+00	6.6980000000E+02
17	1.6000000000E-02	7.2960000000E-03	2.3580000000E+00	1.0160000000E+03
18	1.7000000000E-02	1.0210000000E-02	3.5160000000E+00	1.2850000000E+03
19	1.8000000000E-02	1.4400000000E-02	4.8920000000E+00	1.4460000000E+03
20	1.9000000000E-02	2.0030000000E-02	6.3860000000E+00	1.5460000000E+03
21	2.0000000000E-02	2.7210000000E-02	7.9710000000E+00	1.5960000000E+03
22	2.1000000000E-02	3.5960000000E-02	9.5240000000E+00	1.5000000000E+03

Figure D.8 Excel Data Sheet for Transient Loading